

NORTHWESTERN UNIVERSITY

Nanoscale Corrosion and Tribology Mechanisms in CoCrMo Alloys and
Associated Systems

A DISSERTATION

SUBMITTED TO THE GRADUATE SCHOOL
IN PARTIAL FULFILLMENT OF THE REQUIREMENTS

for the degree

DOCTOR OF PHILOSOPHY

Field of Materials Science and Engineering

By

Alex Yu-Wei Lin

EVANSTON, ILLINOIS

June 2020

ProQuest Number:27964148

All rights reserved

INFORMATION TO ALL USERS

The quality of this reproduction is dependent on the quality of the copy submitted.

In the unlikely event that the author did not send a complete manuscript and there are missing pages, these will be noted. Also, if material had to be removed, a note will indicate the deletion.



ProQuest 27964148

Published by ProQuest LLC (2020). Copyright of the Dissertation is held by the Author.

All Rights Reserved.

This work is protected against unauthorized copying under Title 17, United States Code
Microform Edition © ProQuest LLC.

ProQuest LLC
789 East Eisenhower Parkway
P.O. Box 1346
Ann Arbor, MI 48106 - 1346

© Copyright by Alex Yu-Wei Lin 2020

All Rights Reserved

ABSTRACT

Nanoscale Corrosion and Tribology Mechanisms in CoCrMo Alloys and Associated Systems

Alex Yu-Wei Lin

Early-stage oxidation and corrosion mechanisms of CoCrMo and NiCrMo alloys can be analyzed on the nanoscale by transmission electron microscopy. Both alloys are attractive for a broad array of applications such as gas turbines and aircraft engine components as they are known for their excellent corrosion resistance and mechanical properties at elevated temperatures. Additionally, CoCrMo alloys are widely used in orthopedic implants such as total hip replacements, as they have low wear rates and high biocompatibility, resulting in long service lifetimes. Since corrosion and oxidation behavior and the resulting oxide layers on the alloy surfaces are very sensitive to the conditions employed, it is necessary to understand the relevant mechanisms at specific operating conditions. A thorough analysis of the crystallography and chemistry of nanoscale oxide layers formed on these alloys by transmission electron microscopy can provide fundamental insights on the thermodynamics and kinetics of oxide formation in very different environments.

Nonequilibrium oxide phases, which have unusual combinations of crystallography and chemical compositions, are observed in the early-stage oxidation and corrosion of CoCrMo alloys. An investigation of CoCrMo alloys oxidized at a moderate temperature and short time scale reveals that grain boundaries play a role in assisting the formation of oxides that contain solute capture. As cation and oxygen diffusion is rapid through high-energy grain boundaries, spinel oxides with Cr contents that exceed the thermodynamic limits are observed. An aqueous corrosion appraisal of CoCrMo alloys also shows that the oxide layer, which has predominantly rocksalt crystallography, contains a significant amount of Cr, exceeding the solubility described in thermodynamic data. The oxide layers on a CoCrMo

alloy corroded in model synovial fluids containing hyaluronic acid is somewhat different, as rocksalt crystallography is observed but does not have any solute capture, suggesting that there is a secondary process occurring as the alloy interacts with biomolecules in typical simulated synovial fluids. Further electrochemical analysis indicates that hyaluronic acid significantly prevented the formation of a protective layer by removing Cr cations from the oxide layer. Possible strategies to prevent this deleterious effect are currently under investigation.

In addition, tribological mechanisms at nanoscale contacts are shown both experimentally and theoretically. With *in situ* transmission electron microscopy, mechanical deformations such as compression and shear are observed in crumpled graphene, which is composed of intra-sheet links and graphitic nanocrystals. *In situ* sliding reveals that intra-sheet links are flexible and can fold and unfold reversibly while graphitic nanocrystals are rigid, demonstrating the origins of enhanced mechanical stability and wear resistance of crumpled graphene. By combining contact mechanics and flexoelectricity, the electromechanical couplings at contacting surfaces can be modeled, explaining the thermodynamic driver behind tribocharge transfer. The link between flexoelectricity and triboelectricity is important for understanding the complex nature of localized electrical properties at nanoscale asperities and can lead to the better designs of surfaces to be tailored for specific applications.

Approved by

Professor Laurence D. Marks

Department of Materials Science and Engineering

Northwestern University, Evanston, IL 60208 USA

Acknowledgements

First and foremost, I would like to acknowledge my advisor, Prof. Laurie Marks, for providing me the opportunity to join his lab and develop my own research project as undergrad. Since then, he has always been patient and understanding, and is constantly encouraging me to think rigorously and ask the “right” questions about scientific problems. In addition, I would like to thank him for introducing me to a large network of collaborators whose contributions helped me understand topics more deeply and made this work possible. I would also like to thank the members of my dissertation committee: Prof. Amanda Petford-Long, Prof. Peter Voorhees, and Prof. Santanu Chaudhuri for their time and support. I am also grateful to Prof. Ken Shull for sitting on my qualifying exam committee and providing guidance on my early work in tribology.

I want to thank all of the past and present members of the Marks group. I am especially indebted to Emily Hoffman for patiently mentoring me when I began research as an undergrad and training me on the *in situ* tribology TEM holders when I started on my PhD project. Thanks for always encouraging me to apply for fellowships and attend conferences. I would also like to thank Lawrence and Pratik for their friendship and helping me troubleshoot computer errors throughout the years. A special thanks to Chris for editing my writing, collaborating with me on the triboelectricity work, and helping me get started with DFT. I am also grateful to Xiao-xiang for collaborating on numerous corrosion and oxidation projects and patiently teaching me how to do better high-resolution microscopy. Thanks to Zach for our interesting discussions on microscopy and hosting homebrewing sessions. Thanks to Ryan for helping us win multiple IM ultimate championships. Thanks to Tiffany for keeping the group website and my personal webpage up to date and always making wonderful desserts for group meeting.

I would also like to thank Dr. Alexander Müller and Prof. Andy Minor for hosting me at the National Center for Electron Microscopy at Lawrence Berkeley National Lab

and providing me access to their cryo-FIB instrument. I am especially grateful to Alex for tirelessly working alongside me on a very challenging cryogenic experiment that is presented in Chapter 6.

I would like to thank the staff at the Electron Probe Instrument Center (EPIC) at Northwestern for their technical help with instruments: Dr. Jinsong Wu for training me on TEMs and Dr. Ben Myers and Karl Hagglund for managing the FIB and always willing to help me troubleshoot errors.

I would like to thank specific collaborators for the contribution in the work presented in this dissertation. The CoCrMo samples and used in Chapter 3 and 4 and the electrochemical data used in Chapter 4 are provided by Dr. Simona Radice, Dr. Michel Laurent, and Dr. Markus Wimmer at the Department of Orthopedic Surgery at Rush University Medical Center. The NiCrMo samples used in Chapter 6 are fabricated and provided by Matt Taylor and Prof. John Perepezko of the University of Wisconsin-Madison. The crumpled graphene solutions used in Chapter 7 and synthesized and provided by Prof. Albert Dato and Prof. Gordon Krauss at Harvey Mudd College. I will also like to acknowledge Chris Mizzi for writing much of the code used to generate the figures in Chapter 8.

Above all, I cannot thank my family and friends enough for making all of this possible. They have always supported me, believed in me, and encouraged to me to follow my scientific pursuits. I would especially like to thank my my parents for always listening to me and helping me better understand myself. Last but not least, I would like to thank Martha for her encouragement and love during some of the most stressful times during my PhD. I look forward to our future together.

I also want to officially acknowledge my funding sources. The majority of this work was funded by the National Science Foundation on grant no. CMMI-1400618 and the Office of Naval Research MURI on contract no. N00014-16-1-2280. The experiments in Chapters 6 were performed at the Molecular Foundry and was supported by the Office of Science,

Office of Basic Energy Sciences, of the US Department of Energy under contract no. DE-AC02-05CH1123. The experiments in Chapter 7 were performed at the Center for Nanoscale Materials at Argonne National Laboratory, supported by the US Department of Energy, Office of Science, Office of Basic Energy Sciences under contract no. DE-AC02-06CH11357. I would also like to acknowledge financial support from the Walter P. Murphy Fellowship and the STLE Chicago Section Research Scholarship.

Table of Contents

ABSTRACT	3
Acknowledgements	5
List of Tables	12
List of Figures	13
Chapter 1. Introduction	22
1.1 Background	22
1.2 Organization	26
Chapter 2. Methods	27
2.1 Sample Preparation	27
2.1.1 Alloy Oxidation and Aqueous Corrosion	27
2.1.2 Corrosion in Simulated Biological Fluids	28
2.1.3 TEM Sample Preparation	30
2.2 Characterization	31
2.2.1 Transmission Electron Microscopy	31
2.2.2 <i>In situ</i> TEM	35
2.3 Theoretical Methods	38
Chapter 3. Formation of Cation and Oxygen Diffusion Barriers at CoCrMo Surfaces and Grain Boundaries	41
3.1 Introduction	41
3.2 Methods and Materials	45
3.2.1 Sample Preparation	45
3.2.2 Electron Microscopy	45
3.3 Results	46

	9
3.4 Discussion	52
3.5 Conclusions	58
Chapter 4. Preferential Interaction Between Hyaluronic Acid and Cr in Simulated Biological Conditions	60
4.1 Corrosion, Tribology and Tribocorrosion in CoCrMo Alloys	62
4.2 Methods and Materials	64
4.2.1 Alloy Preparation	64
4.2.2 Corrosion in Model Synovial Fluid	65
4.2.3 Aqueous Corrosion	65
4.2.4 Electron Microscopy	65
4.3 Results	65
4.4 Work in Progress	69
4.5 Conclusions	71
Chapter 5. Thermodynamics of the Formation of Nonstoichiometric Spinel Oxides	73
5.1 Background on Spinel Oxides	74
5.2 DFT Methods	77
5.3 Results and Discussion	78
5.4 Discussion and Conclusions	85
5.5 Future Work	88
Chapter 6. Early-Stage NiCrMo Oxidation Revealed by Cryo-TEM	91
6.1 Introduction	91
6.2 Experimental Details	94
6.2.1 Sample Preparation	94
6.2.2 Aqueous Corrosion and Freezing	95
6.2.3 Cryo-FIB Milling	95

	10
6.2.4 Cryo-TEM Characterization	96
6.2.5 TEM Characterization of Conventionally-Prepared Specimens	97
6.3 Results	97
6.4 Discussion	102
6.5 Conclusions	104
Chapter 7. <i>In situ</i> Observations of Graphitic Staples in Crumpled Graphene	106
7.1 Introduction	107
7.2 Experimental Methods	108
7.2.1 Crumpled Graphene Synthesis	108
7.2.2 Transmission Electron Microscopy	109
7.3 Results and Discussion	110
7.4 Conclusions	116
Chapter 8. Modeling Electromechanical Couplings at Nanoscale Contacts	117
8.1 Introduction	117
8.2 Results	119
8.3 Discussion and Conclusions	125
8.4 Future Opportunities	127
Chapter 9. Conclusions	129
9.1 Oxidation and Corrosion	129
9.2 Tribology and Triboelectricity	130
Bibliography	131
Appendix A. DFT CIFs	164
A.1 Ni ₃ O ₄	164
A.2 Ni ₅ CrO ₈	165
A.3 Ni ₂ CrO ₄	167

	11
A.4 $\text{Ni}_3\text{Cr}_3\text{O}_8$	169
A.5 NiCr_2O_4	170
A.6 $\text{Ni}_3\text{Cr}_9\text{O}_{16}$	172
A.7 NiCr_5O_8	174
A.8 $\text{NiCr}_{11}\text{O}_{16}$	176
A.9 Cr_3O_4	178
Appendix B. Supplementary Video Captions	180

List of Tables

3.1	Composition of low-carbon CoCrMo alloy in at.%	45
5.1	DFT energies normalized by metal atoms and oxygen atoms are shown for each spinel oxide at STP and 1000 K.	82
5.2	BVS for Ni, Cr, and O ions in NiCr ₂ O ₄ , Ni ₃ O ₄ , and Cr ₃ O ₄ . Td denotes tetrahedral sites and Oh denotes octahedral sites.	85
8.1	Examples of flexoelectric coefficient and flexocoupling voltage measurements for both oxides and polymers in the literature. Polymer measurements do not have specified signs, so f is treated as $ f $ for those materials.	119
8.2	Comparison between measure triboelectric surface charge (σ_{tribo}) and calculated flexoelectric polarization (P_{FXE}) for feature sizes in the mm to μm range assuming a flexoelectric coefficient of 1 nC/m.	126

List of Figures

- 1.1 (a) Multiple asperities at an engineering interface. (b) A scanning probe microscope tip, commonly used as a counterface for nanoscale sliding experiments, simulates a single asperity. Adapted from [7]. 24
- 2.1 A schematic of the three-electrode electrochemical test chamber. The working electrode (WE) is the CoCrMo sample, the counter electrode (CE) is the Pt wire, and the reference electrode (RE) is the Ag/AgCl electrode. Adapted from [48]. 29
- 2.2 Various signals are produced when the electron beam interacts with a specimen in the TEM. 33
- 2.3 Atomic-scale stick slip on a Cu(111) surface is observed by measuring the lateral forces with both (a) soft and (b) stiff cantilevers. Bright areas represent high forces and dark areas represent low forces. (a) Image size is 3 nm × 3 nm. (b) Image size is 3.5 nm × 3.5 nm. Adapted from [53]. 36
- 2.4 *In situ* sliding in the TEM is performed by moving the specimen against a stationary AFM tip. 38
- 3.1 SEM images of the CoCrMo sample after oxidation. (a) An overall view shows that selected grain boundaries and grains have darker contrast, indicating inward oxide growth. (b) On the finer scale, bright oxide nanoparticles are well-distributed across most grains and inward growing oxides are found mainly at grain boundaries but can also occur at individual grains. 47
- 3.2 An ADF image shows the uniformity of the outer oxide layer and that multiple inward growing oxides, located on the left side of the image, can be found at selected grain boundaries. 47

- 3.3 Morphology of the duplex microstructure. The outer oxide consists of spinel oxide islands and the inner oxide is a corundum oxide layer, as verified by the FFT of the two regions in the oxide. The lower dashed line marks the metal-oxide interface and the upper dashed line is the approximate location of the corundum-spinel interface. 48
- 3.4 HAADF image with a corresponding compositional linescan of the duplex oxide microstructure. The outer oxide includes (a) a Co_3O_4 spinel and (b) a nonstoichiometric $(\text{Co}_{1-x}\text{Cr}_x)_3\text{O}_4$ spinel. The inner oxide is composed of (c) a Cr-rich corundum layer adjacent to the (d) alloy surface. 49
- 3.5 Inward growth of Cr-rich corundum oxide at a grain boundary. Corresponding EDS mapping indicates that the local region around the corundum oxide is depleted in Cr. 50
- 3.6 A second case of inward oxide growth. The inward oxide comprises of both Cr-rich corundum and Co-rich rocksalt. 50
- 3.7 A third case of inward oxide growth at grain boundaries show that the inward growing oxide is mostly Co-rich rocksalt and the outward growing oxide contain a Cr-rich corundum phase along with a Co-rich spinel oxide. (a) HAADF image shows that outward growing island is phase separated. (b) A TEM image captures the (c) outer oxide, (d) inner Cr-rich layer, and (e) inward growing rocksalt. FFTs of the regions depict the corresponding crystallography in those regions. 51
- 3.8 HAADF images of the oxide morphology. (a) The interface between the inner and outer oxide layers contains additional voids, demonstrating the result of outward cation diffusion and inward oxygen diffusion. (b) Isolated spinel particles can also found throughout the corundum layer, even near the

		15
	metal-oxide interface. The left side of the dash line shows a corundum lattice spacing, while the right side shows a spinel lattice spacing.	52
3.9	A multiscale approach, which involves EBSD mapping, TEM imaging, and EDS analysis of grain boundary carbides can be used to understand the relationship between preferential corrosion, grain boundary misorientation, and Cr depletion. Adapted from [98].	58
4.1	Schematic illustration of the effect of proteins on material degradation over time. Although proteins can reduce corrosion initially, they may cause pits or pinholes to form in the oxide layer and cause increased corrosion. The complexation effect shows that metal can form complexes with proteins and can result in increased corrosion/dissolution rates. Adapted from [153].	64
4.2	CoCrMo discs corroded in RPMI + HA and RPMI + BSA + HA electrolytes indicate the presence of films with different thicknesses.	66
4.3	TEM analysis of the oxide layers in the RPMI + HA sample shows that the oxide islands are polycrystalline and have rocksalt crystallography.	67
4.4	HAADF imaging and a corresponding EDS linescan verified that the thin rocksalt oxide contains almost no Cr, with the exception of minor Cr content near the metal-oxide interface.	67
4.5	(a) The early-stage aqueous corrosion of a NiCrMo alloy show rocksalt oxides forming epitaxially on the metal. Adapted from [160] (b) Similarly, a CoCrMo alloy corroded in Cl ⁻ -containing solutions has mostly rocksalt oxide islands.	68
4.6	The EDS linescan of the oxide layer formed during aqueous corrosion indicated that the oxide composition contains a significant amount of Cr, confirming that nonequilibrium solute capture occurred during oxide formation.	68

- 4.7 Potentiodynamic scans from -0.9 V to 0.9 V (vs. Ag/AgCl) on CoCrMo alloy samples immersed in three different model synovial fluids containing different combinations of Dulbecco's phosphate buffered saline (DPBS), newborn calf serum (BCS) protein, and HA. Without proteins, the presence of HA significantly decreases the corrosion resistance of CoCrMo. Adapted from [161]. 70
- 4.8 (a) Potentiostatic anodic polarization at +0.7 V (vs. Ag/AgCl) for 1 hour indicates that current increases significantly in the DPBS + HA solution, while there is practically no current in the other solutions, suggesting that the alloy remains in the passive state in those cases. (b) The dotted area in (a) is magnified to show the respective current densities in the DPBS and DPBS + NCS + HA solutions. 70
- 4.9 TEM reveals that the oxide formed on a CoCrMo sample immersed in DPBS + HA is porous and has mainly rocksalt crystallography. 71
- 5.1 Crystal structures of a normal spinel and a inverse spinel. A atoms are in gray, B atoms are in green, and oxygen atoms are in red. Adapted from [177]. 75
- 5.2 Plots of the free energy of formation of different spinel oxides with varying amounts of Ni and Cr at STP. Individual points indicate the DFT energies shown in Table 5.1 and the dotted line represents in the convex hull constrained to the spinel structure. The energies shown are (a) normalized per metal atom and (b) normalized per oxygen atom, in order to demonstrate the dominant diffusing species for each case. 80
- 5.3 Plots of the free energy of formation of different spinel oxides with varying amounts of Ni and Cr at 1000 K and 1 atm of oxygen. Individual points indicate the DFT energies shown in Table 5.1 and the dotted line represents in the convex hull constrained to the spinel structure. The energies shown are (a)

- normalized per metal atom and (b) normalized per oxygen atom, in order to demonstrate the dominant diffusing species for each case. 81
- 5.4 The free energies of various crystallographic phases with varying amounts of Ni and Cr at 1000 K and 1 atm of oxygen. Individual points indicate the DFT energies and the dotted line represents in the convex hull. The energies shown are (a) normalized per metal atom and (b) normalized per oxygen atom, in order to demonstrate the dominant diffusing species for each case. Adapted from [123]. 82
- 5.5 Density of states for NiCr_2O_4 , showing the Ni and Cr $3d$ states and the O $2p$ states. Up spins are above the x axis and down spins are below. 83
- 5.6 Density of states for Ni_3O_4 , showing the Ni $3d$ states and the O $2p$ states. Up spins are above the x axis and down spins are below. 84
- 5.7 Density of states for Cr_3O_4 , showing the Cr $3d$ states and the O $2p$ states. Up spins are above the x axis and down spins are below. 85
- 5.8 XRD patterns showing corundum (marked with #) and spinel (marked with *) crystallographies contain rather broad peaks indicating a disordered spinel phase has formed. Adapted from [196]. 90
- 6.1 HREM images show that the rock-salt islands grown on NiCrMo substrate oxidized in sodium sulfate for 10^4 seconds. Adapted from [40]. 94
- 6.2 Schematic showing the cryo-FIB milling process of a frozen corroded NiCrMo alloy, which is mounted to a cooled stage. 96
- 6.3 (a) Cryo-SEM secondary electron image of the frozen corroded NiCrMo half-disc. The irregular top edge is the region that was pre-thinned to electron transparency with Ar^+ ion milling and the bright particles are ice crystals, which charge in the electron beam. (b) A top-down FIB secondary electron

		18
	image of (a) shows that ice contamination (dark particles) is more significant in the lower part of the half-disc, away from the thin alloy edge.	98
6.4	Secondary electron image of (a) the cryo-FIB milled regions that also served as notched markers to identify regions of interest for cryo-TEM imaging. (b) Higher magnification image showing that the regions that were thinned have significantly less contamination in comparison with unthinned regions.	99
6.5	(a) Cryo-TEM imaging of cryo-FIB milled region. SAED patterns from alloy regions show (b) polycrystalline β -Ni _{1-x} Cr _{2x/3} (OH) ₂ with rocksalt Ni _{1-x} Cr _{2x/3} O and (c) rocksalt and corundum oxide phases. (b) Orientational relationships between (1) the (110) Ni _{1-x} Cr _{2x/3} (OH) ₂ ring and the (220) Ni spots and (2) the (101) Ni _{1-x} Cr _{2x/3} O ring and the (111) rocksalt spots are observed. (c) In the thicker part of the sample, the inner diffraction rings are more diffuse and correspond to vitreous ice and the major diffraction vectors of polycrystalline corundum.	99
6.6	Dark-field images taken from (a) the (110) Ni _{1-x} Cr _{2x/3} (OH) ₂ diffraction ring and (b) the (101) Ni _{1-x} Cr _{2x/3} (OH) ₂ diffraction ring. As indicated in both images, the Ni _{1-x} Cr _{2x/3} (OH) ₂ nanocrystals contributing to the diffraction lie on the edges of the Ni-alloy bulk.	100
6.7	X-ray diffraction patterns of β -Ni(OH) ₂ and α -Ni(OH) ₂ . Adapted from [238].	101
6.8	Conventionally-prepared NiCrMo sample shows the growth of rocksalt Ni _{1-x} Cr _{2x/3} O islands. (a) HREM image and (b) the corresponding SAED pattern obtained from the Ni _{1-x} Cr _{2x/3} O - metal interface shows cube-on-cube epitaxy.	102
7.1	Graphitic staples in crumpled graphene nanosheets.	108

- 7.2 *In situ* sliding in the TEM is performed by moving the specimen against a stationary AFM tip. 109
- 7.3 Transmission electron diffraction patterns taken from the regions in the respective TEM images, indicated by circles, show (a) intra-sheet links and (b) graphitic nanocrystals. 110
- 7.4 (a) Prior to sliding and compression, crumpled graphene sheets have no preferential order. (b) After sliding and compression, a 3D non-deformable solid with a higher density of graphitic regions, was formed. 111
- 7.5 (a-d) TEM images extracted from Video S2 displaying that (b-c) the crumpled graphene sheet supported by a graphitic nanocrystal folds as it makes contact with the AFM tip, and then (d) unfolds as it passes the tip. As the graphene sheet folded, edges of the sheet were reoriented into graphitic regions. (e-h) Graphical models showing the structural changes occurring as the sheet was sliding against the tip. The sample is moving from left to right in this sequence. Scale bars, 50 nm. 112
- 7.6 (a-c) As the sample is moving to the right, graphitic nanocrystals, indicated by the black arrows in (a) and (c), have minimal changes in contrast under this sliding condition. This suggests that there are no significant structural changes except for some minimal rotation about the tip. (d-f) As the sample moved to the left, a suspended intra-sheet link, indicated by the black arrows, almost unfolded completely. The localized intra-sheet link, which appeared very dark in (e), almost completely vanished in (f). White arrows indicate the sample's direction of travel. 114
- 7.7 (a-c) Needle-like graphitic nanocrystals, indicated by arrows, acted as support for the graphene sheets. The nanocrystals converged as the sample slid toward the tip, and returned to their original configuration as the sample passed the tip.

The interaction between the graphitic nanocrystals and the AFM tip collapsed the crumpled sheet. The sample is travelling from left to right in this sequence. Scale bars, 100 nm. 114

- 8.1 Schematic of asperity contact between a rigid sphere (shown in blue) and an elastic body (shown in red). The elastic body will deform during both indentation and pull-off, resulting in a net strain gradient opposite to the direction of the applied force (F). 120
- 8.2 (a-e) There are 5 symmetrically inequivalent strain gradients that arise from Hertzian indentation of an elastic half-space that can flexoelectrically couple to the normal component of the electric field. Contour lines indicate the constant value of the strain gradient in units of 10^6 m^{-1} , z is the direction normal to the surface with positive values going into the bulk, and x is the in-plane direction. The origin is at the central point of contact. (f) The magnitude of the average effective strain gradient $|\frac{\partial \epsilon}{\partial z}|_{eff}$ as a function of indenter radius (R). The average effective strain gradient is the sum of the all the strain components shown (a-e) averaged over the indentation/pull-off volumes. 122
- 8.3 (a) Normal component of the electric field induced by Hertzian indentation via a flexoelectric coupling. Contour lines indicate electric field in units of MV/m, z is the direction normal to the surface with positive values going into the bulk, and x is the in-plane direction. The origin is the central point of contact. (b) Magnitude of the average electric field ($|\bar{E}_z|$) in the indentation/pull-off volumes (at asperities) as a function of indenter radius (R) for flexocoupling voltages of 1 V and 10 V. 124
- 8.4 Electric potential difference along the surface of the deformed body for indentation (blue solid line) and pull-off (red dashed line). The x axis represents the in-plane direction and the origin is the central point of contact. 125

8.5 Strain distribution within core-shell InAs nanowires under tensile stress is observed by STEM combined with nanobeam electron diffraction. Adapted from [258].

CHAPTER 1

Introduction

1.1 Background

Tribology and corrosion are old disciplines that have recently seen an increase in attention. Tribology has a long history dating back to ancient civilizations, with records showing that oil and animal fats were used to grease sledges for transporting heavy statues and lubricate wheels and gears in Egypt, Mesopotamia, and China [1]. Similarly, biological corrosion was recorded in Etruscan and Roman civilizations, as dental prostheses made of noble metals such as gold were used to stabilize diseased teeth [2]. Fast-forward to the modern day, tribology and corrosion remain to be important fields of study in biomedical applications, especially in orthopedics and dentistry [3]. The rise of complications such as tissue inflammation and bone loss in CoCrMo metal-on-metal hip replacements has driven the field of bio-tribocorrosion, which studies the electrochemical and tribological aspects of implants in body fluids at the interface, to improve the lifespan of implants and avoid costly revision surgeries. Beyond biomedical applications, tribology and corrosion are prevalent across many industries such as power generation, marine infrastructure and transport, aerospace, and automotive industries. The economic cost of tribology and corrosion is immense, as studies conducted in the last few decades estimate that 2-6% [4, 5] of an industrialized country's gross domestic product is consumed by frictional losses and the estimated cost of corrosion is on the same scale, exceeding \$1.1 trillion in the United States for 2016 [6].

As summarized above, the understanding of surface degradation processes, particularly when tribological components are operating in harsh oxidative or corrosive environments, is critical for the design of new surfaces and alloys for minimizing operating costs and losses and maximizing the service lifetimes. Additionally, in many cases, advancements in industries are exposing materials to more extreme service conditions such as higher temperatures and

pressures, requiring the need for greater understanding of tribological and corrosive behavior across a broad variety of environments.

In order to control friction and corrosion, the basic theory of each will need to be introduced. The laws of friction dating back to DaVinci still see use today in basic discussions of macroscale phenomena, and they are listed here:

$$F = \mu F_N \quad (1.1)$$

$$F \not\propto A \quad (1.2)$$

$$F \not\propto v \quad (1.3)$$

Where F is the friction force, μ the scalar coefficient of friction, F_N the normal load, A the contact area, and v the sliding velocity. The first macroscopic law of friction states that when a body is in motion along a contacting surface, the dissipative friction force will be directly proportional to the normal force, related by a constant known as the coefficient of friction, μ . This quantity is determined by materials properties of the contacting surfaces as well as environmental conditions and surface roughness at the interface. The second macroscopic law of friction states that friction is independent of the area of contact. For example, a piece of paper sliding across a table on its flat side experiences the same friction force as if it were sliding on its edge. This statement was not formally challenged until 1950 by Bowden and Tabor with the realization that areas of contact between surfaces (even smooth ones) consist of multiple asperities and account for a small fraction of the apparent contact area (Figure 1.1). The third macroscopic friction law, contributed by Coulomb, states that friction is independent of sliding speed. This has also been contradicted with extensive nanoscale sliding experiments. Although the macroscopic laws of friction serve as good approximations for macroscale behavior, they do not accurately explain the theory of frictional wear and deformation at the nanoscale.

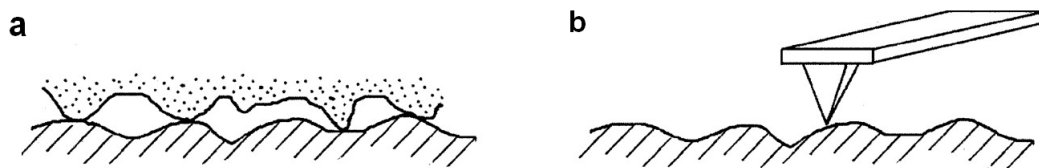
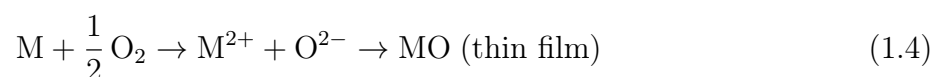


Figure 1.1. (a) Multiple asperities at an engineering interface. (b) A scanning probe microscope tip, commonly used as a counterface for nanoscale sliding experiments, simulates a single asperity. Adapted from [7].

A fair amount is known about nanotribology, including wear mechanisms. Volume loss of sliding contacts is a complicated process depending on both the intrinsic properties of the material, such as hardness and fracture toughness, and extrinsic factors such as contact geometry and the environment [8]. Tribological studies of two surfaces sliding against each other usually place an emphasis on friction coefficient and wear. At the macroscopic scale, plasticity of the materials, stress distribution, along with environment and sliding velocity, have been interrogated with conventional experimental techniques such as pin-on-disc tribometers. It is known that wear can be caused by abrasive, adhesive, fatigue, fretting, and corrosive wear, resulting in different degrees of volume loss [7, 9]. From the mechanical perspective, the Archard wear model [10] has been widely proven for general tribological systems with total wear volume loss being proportional to the normal load, the sliding distance, and inversely proportional to material hardness. The stresses at the surface can be calculated using approaches such as Hertzian contact theory [11] and adhesion [12–15]. In addition to mechanical wear, tribochemical reactions at sliding contact surfaces are also important and, in many cases, critically influence the environmental sensitivity [16–20].

Moving to corrosion, when a metal oxidizes in an aqueous environment or in air at elevated temperatures, the following oxidation reaction occurs:



The thermodynamics for corrosion reactions of various metals can be ascertained from Pourbaix diagrams [21], which show the equilibrium electrochemical potential dependence of pH

at given pressure, temperature, and concentration. Pourbaix diagrams are useful to predict the immunity of passivity; however, they overlook the kinetic phenomena of corrosion reactions. The established models of protective film oxide formation in aqueous environments [22] and higher temperature oxidation have focused upon the development of equilibrium phases, such as nickel oxide and chromium oxide in NiCr alloys, or enrichments of alloying elements in passive films [23–26]. A thin oxide layer develops first with a substantial electrical potential gradient across it, as first described by Cabrera and Mott [27]. As the film thickness increases, point defects diffuse across the oxide due to the chemical potential gradients and the electric fields [28–30], often referred to as field-assisted diffusion. Eventually, the film thickness becomes large and standard diffusion becomes the controlling factor. In an aqueous environment, the film may never reach this limit due to simultaneous dissolution at the oxide-water interface [31, 32]. In some cases, a thin oxide film develops which does not significantly oxidize further, serving as a self-protective coating. In other cases, particularly when chloride ions are present in the aqueous environment, there is accelerated corrosion, as the protective oxide film may develop pits and pinholes and expose the metal to corrosion attack [33, 34]. There is significant experimental understanding of how to mitigate chloride attack, including the addition of Mo or other alloying elements [35–39]. Typically, aqueous films have been characterized with extensive X-ray photoelectron spectroscopy (XPS) data, and solid-state oxide films have been examined with X-ray diffraction (XRD) or electron diffraction. More recently, nonequilibrium oxide phases have been found in the oxide films during both air oxidation and aqueous corrosion by combining structural information with atomic scale chemical analyses [40, 41]. Many experimental methods today are capable of probing the structure and chemistry of microscale, nanoscale, and even atomic scale surfaces, motivating future studies of nanoscale tribocorrosion mechanisms in more detail and allowing for the development and design of better performing materials.

Tribocorrosion, a combination of corrosion with tribology, to the first order has to involve a linear combination of the two phenomena. For example, minor wear in a quasi steady-state

oxide film in aqueous conditions can promote dissolution, analogous to what was observed in tribochemical attack of graphite via *in situ* experiments [42]. A classic model for delamination failure of an oxide film is associated with metal vacancies leading to Kirkendall voids [43–45] at the metal-oxide interface which act as nucleation sites for cracks. Clearly, failure will be enhanced due to external mechanical tractions. There are other possibilities, such as the combination of external stresses and internal ones due to electromechanical couplings [46, 47]. Beyond these examples, there may be many more, non-linear effects that only occur in tribocorrosion and are not so relevant for either tribology or corrosion in isolation but hold relevance in reality.

1.2 Organization

This thesis is organized with an overview of experimental and theoretical methods in Chapter 2. Experimental results of nonequilibrium solute capture at CoCrMo grain boundaries are presented in Chapter 3, with a brief discussion of the kinetics of oxide formation at grain boundaries with high interfacial energies. The details of the electrochemical behavior of CoCrMo alloys in model synovial fluids and a discussion of current work in progress are presented in Chapter 4. Next, I will turn to the thermodynamics of forming nonstoichiometric spinel oxides in NiCr alloys using density function theory (DFT) in Chapter 5. A cryo-transmission electron microscopy (TEM) approach to characterize hydroxide phases in early-stage aqueous corrosion is presented in Chapter 6. *In situ* TEM observations of the nanomechanical behavior of crumpled graphene are presented in Chapter 7. Finally, I will discuss a model that uses the flexoelectric effect as a thermodynamic driver to explain and quantify tribocharge separation and transfer in Chapter 8.

CHAPTER 2

Methods

The purpose of this chapter is to present the details of various experimental procedures which were commonly used throughout the work described herein. In order to study corrosion and tribology mechanisms in depth, a combination of several sample preparation, characterization, and theoretical methods were employed to examine the structure and chemistry of the resulting surface after electrochemical or mechanical treatments. The first portion of this chapter will focus on sample preparation by describing the oxidative or corrosive conditions used for alloys and the methods used to prepare these samples for nanoscale characterization. In the next portion of the chapter, background for the electron microscopy techniques, including the *in situ* TEM method used to study tribology, will be introduced. Lastly, in the final portion of the chapter, density functional theory used in thermodynamic calculations is described, followed by a brief discussion of the bond valence sum approach to quantify the structural stability of oxide phases.

2.1 Sample Preparation

2.1.1 Alloy Oxidation and Aqueous Corrosion

Before oxidation and aqueous corrosion, alloy samples were mechanically polished through a sequence of progressively finer sizes of silicon carbide abrasive papers from 320-grit up to 1200-grit with water lubrication. Next, the polishing was performed using water-based 3 μm and 1 μm diamond suspensions dispersed on a cloth-based polishing pad. The final stage polishing was performed using a 0.06 μm Al_2O_3 slurry until the alloy surface had a mirror finish. Lastly, the samples were ultrasonically cleaned in acetone and de-ionized water for 10 minutes each, to remove any remaining debris from mechanical polishing.

To simulate oxidation conditions, the polished samples were oxidized either in ambient air or flowing oxygen at temperatures from 700 to 1000 $^\circ\text{C}$ in a quartz tube furnace for

0.5 to 2 hours. For selected samples, the ends of the quartz tube were sealed and oxygen gas was flowed through the tube furnace with a pO_2 of 0.5 atm to increase the oxidation rate. To simulate early-stage aqueous corrosion, polished alloy samples or TEM samples (see Section 2.1.3) were corroded in 200 mL of a 0.1 M NaCl solution adjusted with 0.1 mM HCl to pH 4, with 5 μ L of H_2O_2 (30% w/w) injected near the sample surface to increase the oxidation rate. This treatment was verified by Dr. Katie Lutton and Prof. John Scully at the University of Virginia to produce an electrochemical potential near +0.2 V versus a saturated calomel reference electrode (SCE), a potential within the passive region. Verification of the chemical potentiation approach was achieved by observing identical oxides in electrochemical impedance experiments [40]. Both the bulk samples and TEM samples were corroded for 10^4 seconds at room temperature.

2.1.2 Corrosion in Simulated Biological Fluids

In order to investigate the interactions of CoCrMo alloys with hyaluronic acid (HA) and bovine serum albumin (BSA), which are constituents in human synovial fluid, electrolyte solutions were tested in a three-electrode electrochemical cell that was connected to a Gamry Series G 750 Potentiostat by Dr. Simona Radice of the Department of Orthopedic Surgery at Rush University Medical Center. An illustration of the three-electrode electrochemical test is shown in Figure 2.1. The polished CoCrMo samples were fitted into the center of the testing chamber, acting as the working electrode. The counter electrode consisted of a 0.5 mm Pt wire that wrapped around the circumference of test chamber wall. A Gamry Silver/Silver Chloride Skinny Reference Electrode in saturated KCl solution was used as the reference electrode. The reference electrode was located about 2 mm away from the polished CoCrMo surface. To simulate typical physiological conditions, the tests were performed inside a water-jacketed CO_2 incubator with the temperature set to 37 °C and the CO_2 level set to 5.0%.

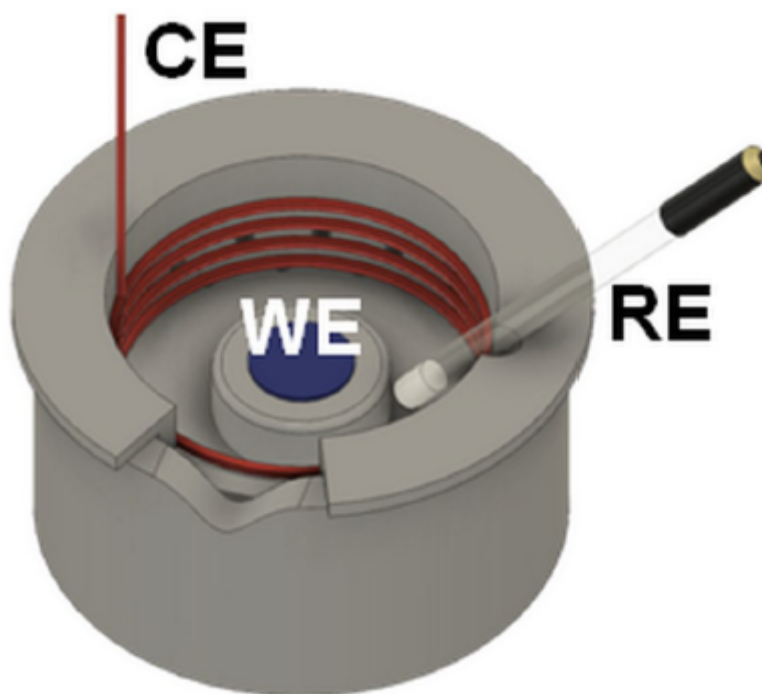


Figure 2.1. A schematic of the three-electrode electrochemical test chamber. The working electrode (WE) is the CoCrMo sample, the counter electrode (CE) is the Pt wire, and the reference electrode (RE) is the Ag/AgCl electrode. Adapted from [48].

Generally, the electrochemical test protocol used in this thesis includes the following steps: open circuit potential (OCP), potentiodynamic polarization, and potentiostatic polarization. At the OCP, the anodic reaction rate is equal to the cathodic reaction rate, and the OCP value is often used to determine whether the material is in the passive or active corrosion regime. Potentiodynamic polarization is a characterization step that involves changing the potential of the working electrode and monitoring the current which is produced. By measuring the corrosion current for the entire range of the potentiodynamic scan, a breakdown potential, which indicates the transition to the transpassive domain, can be observed. Lastly, the potentiostatic polarization involves applying a constant anodic potential in the passive domain, close to the transpassive domain so Cr^{3+} will dissolve. The potentiostatic polarization step can clarify whether alloys exhibit lower corrosion resistance in different simulated biological

fluids. Even though some of the potential ranges tested exceed the clinically observable values, the electrochemical test protocols can provide valuable insight into how individual components in the synovial fluid affect corrosion, leading to a more clinically relevant understanding of bio- and tribocorrosion.

2.1.3 TEM Sample Preparation

TEM samples were primarily prepared with two different methods: a conventional TEM sample preparation method or a focused ion beam (FIB) lift-out method. The conventional TEM sample preparation method was employed when the area of interest was large and the focus of the study was to establish basic mechanisms; for instance, the understanding of oxide formation on CoCrMo alloys during aqueous corrosion. In contrast, the FIB lift-out method was used to identify details of corrosion and oxidation processes, specifically at surfaces and grain boundaries. The TEM lamellae prepared in a FIB were typically 50-100 nm thick and contained grain boundaries or oxide islands, allowing for the characterization of the structure and chemistry of the metal-oxide interface.

To prepare conventional TEM samples, bulk NiCr, NiCrMo, and CoCrMo alloys were cut into thin slices using a Buehler Isomet low speed saw. The alloy slices were cut into 3 mm discs with thicknesses of approximately 0.5 mm using a rotary disc cutter and 40 μm silicon carbide slurry, and mechanically polished to thicknesses of less than 100 μm with silicon carbide lapping paper and water lubrication. The alloy discs were mechanically dimpled until the centers of the discs were about 25 μm thick. Following that, the dimpled discs were washed with acetone and ion milled with a Fischione Model 1050 TEM Mill operated at 5 kV with a 6° milling angle for 1 to 4 hours until a small hole began to form at the center, followed by a final polish at 1 kV with a 2° milling angle for 1 hour. To further reduce the amorphous and ion-implantation layers, TEM samples were loaded into a Fischione Model 1040 Nano-Mill for low-angle Ar⁺ ion milling at 500 eV for several minutes.

For the FIB lift-out method, the TEM samples were lifted out after the deposition of Pt protective layers on the oxidized or corroded surface in a dual-beam FEI Helios Nanolab FIB system, and then thinned using a beam energy of 30 kV. The FIB consists of a scanning electron imaging beam operating at 10 kV with a beam current of 1.4 nA for imaging and a Ga⁺ ion milling beam orientated at 52° to the electron beam operating at 30 kV with beam currents ranging from 93 pA to 48 nA for milling. A final cleaning step was performed at 2 kV to reduce the amorphous layer thicknesses in the TEM lamellae.

2.2 Characterization

2.2.1 Transmission Electron Microscopy

The majority of the structural and chemical characterizations of samples undergoing oxidative, corrosive, and tribological processes were performed with transmission electron microscopy (TEM). TEM is one of the most effective characterization techniques as it has the ability to resolve near-atomic scale information about both the bulk and surfaces of materials while simultaneously collecting crystallographic information with transmission electron diffraction. The capability to image thin oxide layers and nanoscale oxide islands and select an appropriate area for electron diffraction is critical for understanding oxidation and corrosion mechanisms. More details about studying tribological mechanisms with *in situ* TEM will be discussed in Section 2.2.2.

Electron microscopy uses the interactions of high energy electrons with a sample to characterize the atomic and electronic structure of that sample. Louis de Broglie first theorized that the electron had wave-like characteristics, with a wavelength significantly smaller than that of visible light. According to de Broglie, the wavelength of the electrons which reach the sample is related to their energy. With the proper relativistic correction, this wavelength is on the order of 2.51×10^{-12} m in a typical TEM. The resolution limit, as defined in Equation 2.1, will show that the theoretical wavelength-limited resolution in a TEM is smaller than the H atom.

$$d \cong \frac{1.22\lambda}{\beta} \quad (2.1)$$

Here, d is the minimum distance that can be resolved, λ is the electron wavelength, and β is the semi-angle of the magnifying lens. Although the resolution based on the electron wavelength is high, in reality it will be limited by the aberrations in the electron optics. In addition to the spherical aberration (C_s) and chromatic aberration (C_c) in the electromagnetic lenses, the image resolution will be further impacted by the misalignment of the lenses, vibrations, electromagnetic interference, and thick samples. The introduction of aberration correction systems, which can measure and correct the principal aberrations affecting the resolution, diagnose and eliminate parasitic aberrations such as astigmatism, and improve the stability of the microscope [49–51], have made it significantly easier to obtain atomic-resolution imaging despite the various sources that reduce the image resolution.

Many modern TEMs have the ability to operate in scanning mode, where a focused and rastering electron probe is used for imaging instead of a parallel beam. This mode of operation is called scanning transmission electron microscopy (STEM), and can be used for correlated high-resolution imaging and quantitative chemical analysis. As the fine electron probe scans the sample in a raster pattern, the scattered electrons are detected by detectors that are placed after the sample. Similar to a conventional TEM, a STEM is capable of acquiring bright field (BF) images and one can also use an annular bright field (ABF) detector. STEM also have annular dark field (ADF) detectors, which only collect the scattered electrons over an annulus at an intermediate angle. ADF imaging provides diffraction contrast and some sensitivity to atomic number (Z) as different elements will appear at varying intensities. To further improve the Z -contrast in images, a high-angle annular dark field (HAADF) detector can be inserted to collect the electrons that scatter by a higher angle than in ADF mode. At high-angle scattering conditions, the image contrast will be sensitive to the thickness of the atomic columns and the atomic number. The collected HAADF signal will be proportional to

Z^n , where n is 1.7-2. While HAADF imaging in STEM mode is often referred to as Z-contrast imaging for convenience, it is crucial to check that the actual angular ranges that STEM detectors are collecting are in fact large enough to minimize diffraction contrast. Additionally, spherical and chromatic aberrations also impact the resolution of images captured in STEM mode, similar to conventional TEM imaging. Aberrated electron beams will not be properly focused at the appropriate probe positions, resulting in decreased spatial resolution. To remedy this, C_s correctors improve image resolution by forming smaller probes with higher currents. Consequently, the spatial resolution and sensitivity of spectroscopy techniques performed in STEM mode will be greatly enhanced as well.

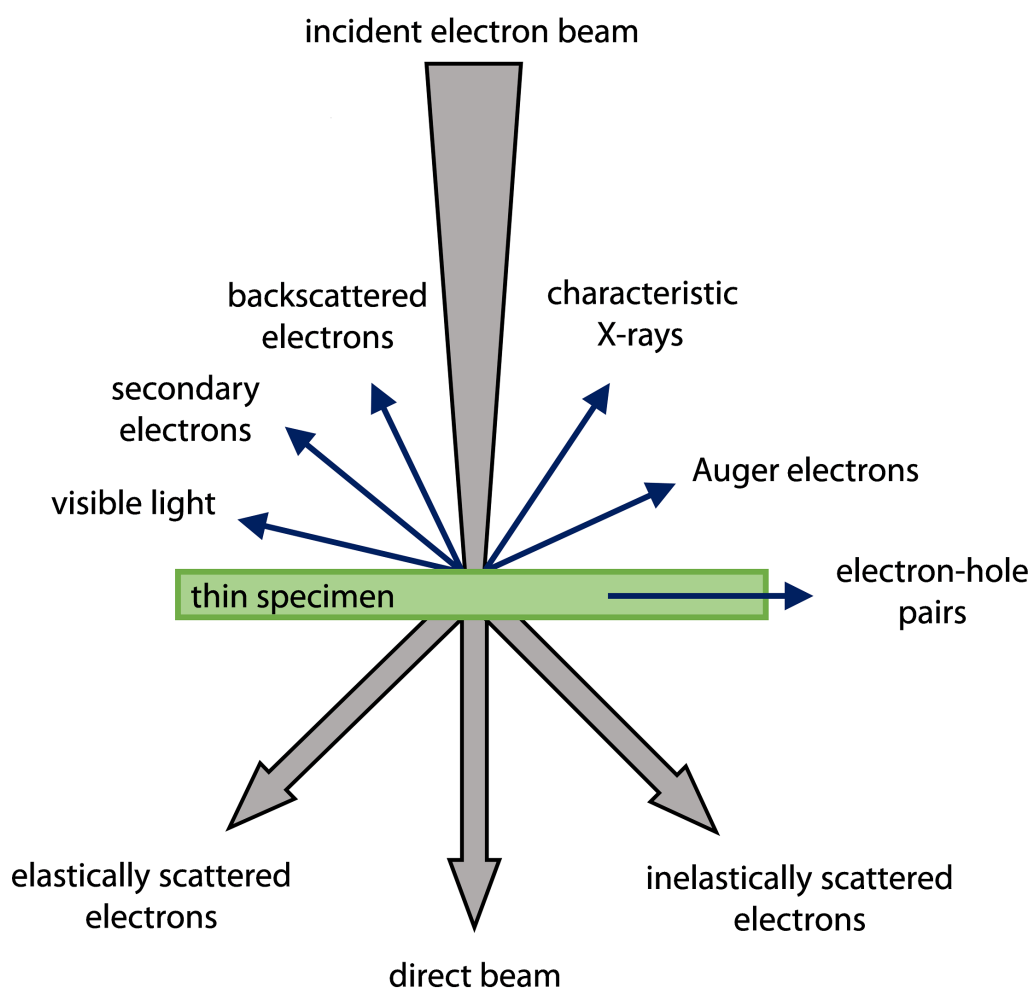


Figure 2.2. Various signals are produced when the electron beam interacts with a specimen in the TEM.

In addition to high-resolution imaging, the wide range of secondary signals produced from electron-specimen interactions in a TEM can be used for additional analytical characterization. A schematic of these secondary signals is shown in Figure 2.2. For the work reported in this thesis, I heavily use spectroscopy techniques such as energy-dispersive spectroscopy (EDS) which uses characteristic X-rays and electron energy loss spectroscopy (EELS) which uses inelastically scattered electrons to characterize the chemical compositions of oxide layers on a corroded metal alloy. As the electrons are inelastically scattered by the specimen, they are promoted from the K, L, or M shells to unfilled shells above the Fermi level. As the inner shell electrons get promoted, electrons from the outer shells will decay into the unfilled shells and emit characteristic X-rays, which match the energy difference between the two shells. These characteristic X-rays are collected by a detector (or sometimes detectors) and qualitative and quantitative chemical compositions of specific regions of interest in a specimen can be obtained. In contrast, EELS uses the kinetic energy change of the beam electrons as they transmit through the specimen by collecting the exiting electrons with a magnetic-prism spectrometer. The energy distribution of the inelastically scattered electrons provide information about the atoms present in the material, the bonding and oxidation states of the atoms, and the collective interactions of atoms with their neighbors, allowing one to fully characterize the chemical and structural properties of the specimen. Although EELS has many capabilities, this thesis will only focus on the elemental quantification of various *3d* transition metal oxides.

While many different electron microscopes were used throughout this thesis, the majority of the experimental data was collected on these three microscopes located at Northwestern University:

- (1) JEOL ARM-200CF, a probe aberration corrected cold-field emission S/TEM operated at 200 kV, equipped with a Gatan Quantum EELS spectrometer and two Oxford X-Max 100TLE windowless silicon drift detectors for EDS,

- (2) JEOL ARM-300F, a cold-field emission S/TEM operated at 300 kV, equipped with an Oxford silicon drift detector for EDS,
- (3) JEOL JEM-2100F, a field-emission S/TEM operated at 200 kV, equipped with a Gatan GIF system for EELS and HRTEM and an Oxford Inca EDS detector.

2.2.2 *In situ* TEM

The most popular approach for nanoscale tribology studies has been scanning probe microscopy techniques, which include atomic force microscopy (AFM). AFM uses optical sensing to take precise measurements of the AFM tip's interaction with the surface. In a conventional AFM, the normal force between the tip and the sample is measured to determine the topography of a surface. For friction and sliding experiments, it is more relevant to use lateral force variations, which can be measured from the lateral deflections of the cantilever via optical interferometry as the tip interacts with the surface [52]. This technique is now commonly known as friction force microscopy (FFM) and has been used heavily to observe various atomic scale friction phenomena such as stick slip [52, 53], superlubricity [54–56], and lattice directed sliding [57, 58]. In addition, FFM is also used to determine the effects of sliding velocity [59, 60], substrate crystallography [61, 62], temperature [63, 64], and boundary layer thickness [65]. Furthermore, the arrangement of different chemical functional groups and its effect on lubrication and adhesion can be examined with chemical force microscopy, which uses chemically modified AFM tips to probe surfaces with different functional terminations [66]. In summary, scanning probe microscopy techniques are fairly robust due to their ability to map frictional domains across many different materials systems with a force resolution on the order of tens of piconewtons. The atomically sharp tips used in these approaches approximate single asperity contacts, effectively simulating fundamental solid-solid interactions in nanotribology.

Experiments in tribology have often suffered from the inability to observe the interactions at a sliding interface, commonly known as the buried interface problem. Many previous studies of friction and adhesion at sliding interfaces have heavily used scanning probe microscopy

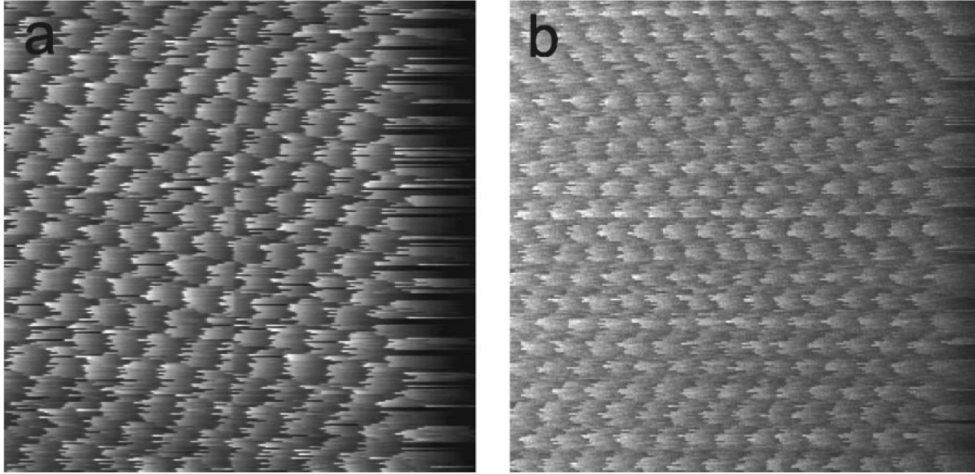


Figure 2.3. Atomic-scale stick slip on a Cu(111) surface is observed by measuring the lateral forces with both (a) soft and (b) stiff cantilevers. Bright areas represent high forces and dark areas represent low forces. (a) Image size is $3 \text{ nm} \times 3 \text{ nm}$. (b) Image size is $3.5 \text{ nm} \times 3.5 \text{ nm}$. Adapted from [53].

techniques. A number of techniques have been modified to include *in situ* data such as optical spectroscopies [67–69] or XPS [70]. Additionally, dynamic processes at monolayer interfaces such as the motion of misfit dislocations have been observed [71–73]. Although these methods have identified and quantified many different friction phenomena on the nanoscale, *ex situ* characterizations of contact surfaces and volume averaged measurements do not necessarily represent a single asperity-asperity contact.

An ideal experimental approach is to slide a single asperity against a surface, image at the atomic scale in real time at the structural and chemical levels, and then correlate the observations with applied force measurements and surface traction. While this cannot yet be performed, many advances in instrumentation, especially the specialized TEM holder, have gotten closer to this ideal experiment. Designs for *in situ* contact probes specifically for TEMs date back to the 1970s [16]. Using this technology, small volumes of materials can be stressed in different ways, for instance, indentation of soft materials, wear of soft tips on hard surfaces, bending of nanowires, and compression of materials between hard contacts. Newer iterations of these contact probes improved the position resolution, and it became more common to use scanning probe instruments such as an AFM or scanning tunneling

microscope (STM) within a TEM. Some of the most elegant work to date is done by Kizuka et al. [74–76] who showed atomic-scale images of a gold tip sliding on a gold surface.

In situ TEM methods allow for understanding key elements of the processes taking place at buried interfaces. While sliding experiments inside the TEM are not as quantitative as AFM and FFM approaches or mesoscale tribometers such as the pin-on-disc tribometer, its ability to reveal nanoscale and atomic scale details with real-time imaging is unparalleled. Over the last decade, the advent of commercial systems from Hummingbird, Hysitron, and Nanofactory has motivated experiments at much higher precision and image resolutions, as many of these holders are compatible with aberration corrected TEMs. Current instruments use either a STM or AFM tip or a tip specialized for mechanical stability in nanoindentation experiments.

In this thesis, I will concentrate on sliding solid-solid interfaces and directly observing the interfaces in real time without having to rely on retroactive post-mortem characterizations. A Nanofactory AFM-TEM holder, illustrated in Figure 2.4, is used for *in situ* sliding studies. To date, the image resolution is not as good as conventional high-resolution TEMs, mainly due to vibration of the sample and coupling between the electron beam and piezoelectric drives in the holder. Despite the fact that the built-in AFM tip in the holder is capable of collecting force measurements and AFM images, the mechanical stability of the probes and the accuracy of the measurements remain poor in these instruments.

With the geometry of the holder in mind, it is pertinent to mention the requirements for experimental design in order to observe tribological phenomena in a TEM. The sample has to be thin along the electron beam direction of an appropriate surface exposed to the AFM tip, which serves as a counterface during slide processes. Additionally, the sample is required to physically fit into the holder as the frame is only slightly larger than 3 mm, the diameter of a typical TEM grid. A successful example is drop casting lubricant materials onto a fractured SiN substrate that is glued onto a tungsten wire, which can then be inserted into the sample mount in the AFM-TEM holder. As a result, the sample along with the SiN

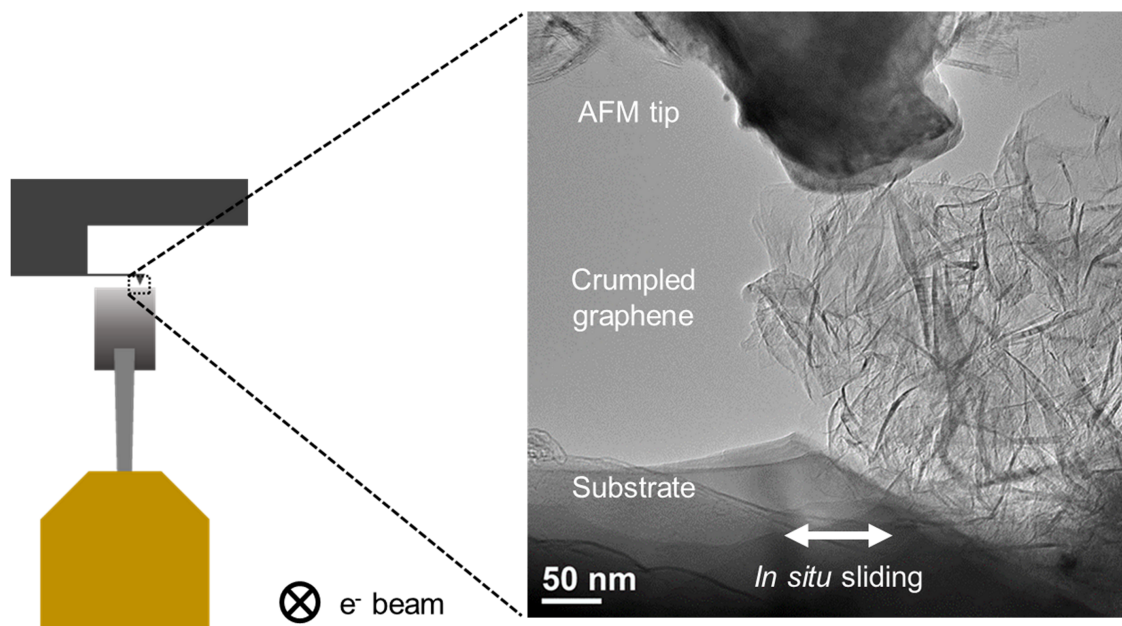


Figure 2.4. *In situ* sliding in the TEM is performed by moving the specimen against a stationary AFM tip.

substrate can then be moved in contact to the tip for sliding. Furthermore, the sample and holder alignments are critical for successful *in situ* sliding experiments. While the resulting images and videos appear as 2D images, the experiments are in 3D so the relative positions of the sample surface, tip, and the entire holder need to be aligned in the electron beam. To accomplish this task, a programmable gaming controller connected to the TEM holder manipulator is used to adjust the sample position in the x, y, and z directions with sub-nanometer positional resolutions. The Nanofactory AFM-TEM holder system was used in a 200 kV FEI Tecnai F20ST TEM at Argonne National Laboratory.

2.3 Theoretical Methods

Density functional theory (DFT) allows for the calculations of the structure, thermodynamic stability, and electronic properties of compounds that may not have any existing experimental data. In DFT, the ground state electron density, $\rho(\mathbf{r})$, has a one-to-one mapping to any observable property. This general theorem simplifies a many-body system of n electrons into a set of n single-electron Schrodinger-like equations, which can be calculated

with one of many modern DFT implementations. While DFT is exact, its utilization requires approximating what is known as the exchange-correlation functional and the quality of this approximation affects the accuracy of the DFT simulation. For example, transition metal oxides are well-known to be inaccurately modeled by standard PBE or LDA methods, as they tend to overestimate the hybridization between the metal $3d$ orbitals and the oxygen $2p$ orbitals [77, 78]. This results in too much covalency (too little ionicity). To correct for the covalency problem, the LDA+ U method [77, 79] increases the ionicity by introducing an energy penalty (Hubbard U term) to reduce the degree of $2p$ - $3d$ hybridization. However, the method requires the user to input a value for the Hubbard U , which is difficult to determine independently. Additionally, even if the value of U is “correctly” picked, the U term is not a global parameter as bonding is highly dependent on the local environment and spin states. A recently developed method uses an on-site hybrid approach [80–82], which adds an exact exchange to correct the highly correlated $3d$ orbitals, that can adapt to the bonding environment at different atomic sites and changes in the spin states. This approach enables the calculation of a wide range of structures and compositions with relative ease, as a full structural minimization is approximately 10% slower than a conventional PBE calculation.

DFT calculations in this thesis were performed with the all-electron augmented plane wave + local orbitals (APW+lo) WIEN2K code [83, 84]. The spin-polarized calculations used the PBE functional exchange-correlation potential [85], a hybrid fraction of 0.25 for the $3d$ electrons using the on-site hybrid approach [80–82], a RKmax of 6.5 and a k-point mesh of $5 \times 5 \times 5$, with atomic positions and densities converged with a parallel fixed-point algorithm [86]. All structures were fully relaxed, and the lattice parameters were optimized as a function of the volume while maintaining the same space group. As a secondary check, the treatment of transition metal oxides was compared to experimental thermodynamic data such as the heats of formation for NiO and Cr₂O₃, and the difference is smaller than the intrinsic errors in typical DFT calculations.

In addition to the formation energies, optimized structures, and density of states, bond-valence sums (BVS) were analyzed. BVS provides a simple way to characterize the structural stability with respect to the coordination and bonding for atoms in an ionic compound [87–89]. The calculation of the BVS is defined in Equation 2.2:

$$BVS = \sum_i v_i = \sum_i \exp\left(\frac{R_0 - R_i}{b}\right) \quad (2.2)$$

Where v_i is the individual bond valences, R_0 is the parameterized length for a particular bond, R_i is the observed DFT bond length, and b is an empirical constant which is usually set to 0.37. After the BVS values are determined for each of the atoms in a DFT calculated structure, they should have values that are similar to their preferred valence states. The BVS can also be used to interpret the valence of the metal atoms, which can be complex as many transition metals are multivalent and can exhibit multiple valences in a single compound.

Formation of Cation and Oxygen Diffusion Barriers at CoCrMo Surfaces and Grain Boundaries

3.1 Introduction

CoCrMo alloys are attractive for a broad array of applications as they are known for their excellent corrosion resistance and mechanical properties. In particular, CoCrMo alloys are widely used in orthopedic implants such as total hip replacements, as they have low wear rates and high biocompatibility, resulting in long service lifetimes. The corrosion of CoCrMo alloys has been closely examined in biomedical applications, as existing studies cover topics such as electrochemical behaviors in simulated physiological settings [90–94], intergranular corrosion of different microstructures [95–97], and grain-boundary assisted crevice corrosion [98, 99]. The addition of Mo in CoCr-based alloys, the impact of which is still somewhat unclear in the context of oxidation resistance, extends the use of these alloys to high temperature applications, such as gas turbines used in power generation and fuel nozzles in aircraft engines. While the corrosion processes in CoCrMo alloys are well-described in various simulated physiological conditions, the oxidation processes in elevated temperatures are not as well-documented. In fact, most elevated temperature studies of CoCrMo alloys are completed at very high temperatures ($T > 900$ °C) and long oxidation times, which are often on the order of tens to hundreds of hours. Since oxidation behavior is very sensitive to the conditions employed in a study, it is difficult to understand the oxidation of CoCrMo alloys at intermediate temperatures by simply extrapolating the results from high temperatures. Since oxidation resistance is a critical requirement for alloys designed for specific operating conditions, the microstructures of oxide layers formed at intermediate temperatures provide crucial details about how oxides initiate and evolve.

Several studies of long-term oxidation of CoCr alloys at various high temperatures have been published [100–104]. Duplex oxide scales consisting of an outer layer of columnar CoO

and an inner layer of CoO with Cr_2O_3 and CoCr_2O_4 inclusions are observed in a Co-10Cr alloy oxidized at 800-1300 °C. The duplex oxide morphology is consistent with previous studies of CoCr alloys of different Cr compositions that range from 0-48 wt.%. According to the work by Phalnikar et al. [100], the oxidation rate of this system increases with increasing amounts of chromium up to about 10 wt.% Cr. As the Cr content exceeds 10 wt.%, the oxidation rate decreases with increasing chromium content up to around 30 wt.%. The increase of oxidation rates in CoCr alloys with dilute amounts of Cr has been investigated more closely in kinetic studies such as diffusion marker and isotopic experiments [105] as well as on the analysis of the scale morphology and composition [104, 106]. The decrease of oxidation rates in CoCr alloys with high Cr concentrations is attributed to the Cr_2O_3 and spinel particles imparting oxidation resistance in the inner oxide layer. The general understanding of the role of Cr_2O_3 and spinel CoCr_2O_4 is that both oxide phases act as diffusion barriers that limits outward cation diffusion through the oxide scale, resulting in reduced oxide growth. However, as previously mentioned, these studies only examined oxidation at high temperatures ($T > 900$ °C) for long periods of time. Additionally, oxidation resistance and the morphology and composition of the oxide layers have not yet been investigated in CoCrMo alloys at intermediate temperatures. Furthermore, the effect of grain boundaries on the formation of oxides at the metal surface during oxidation has not been analyzed for CoCrMo alloys either.

For completeness, two mechanisms that are generally applicable to oxidation and corrosion will be discussed here: nonequilibrium solute capture and grain boundary sensitization. Nonequilibrium solute capture, which was recently found to exist in multiple Cr-containing alloy systems [40, 41, 107–109] and may extend to other systems as well [110], is a phenomenon where oxides have unusual combinations of crystallographies and chemical compositions, far from thermodynamic limits documented in literature such as phase diagrams. Nonequilibrium solute capture occurs frequently in early-stage oxidation and corrosion, since the kinetic conditions for solute capture to occur are met when there are rapidly moving interfaces (growing oxidation front) or a static interface with a large net flux of atoms across it (rapid

diffusion). In addition to the kinetic conditions, the thermodynamic conditions require that the nonequilibrium phase is metastable but has not been provided enough time or driving force to relax back to the global energy minimum. The kinetic and thermodynamics requirements also suggest that although nonequilibrium solute capture is observed in oxidation and corrosion, it does not exclusively apply to these cases and could be observed in other contexts as well. With the knowledge of nonequilibrium solute capture, both the crystallography and chemistry of the oxide are required in order to fully characterize the oxide layers. If only one of the two was examined, inaccurate conclusions about the initiation and evolution of these oxides could be drawn. For instance, the CoCrMo alloy used in this study forms protective oxides during oxidation owing to its high Cr concentration, and numerous studies claim that the oxide is Cr_2O_3 [90–92, 111], citing only coarse scale XRD or XPS studies. However, these results are in fact not indicative of the alloy phases during early-stage oxidation or corrosion nor are they representative of the whole process taking place.

The other general mechanism that will be covered in this chapter is grain boundary sensitization. The term sensitization refers to the local reduction of a protective alloying element, which is typically Cr, resulting in enhanced corrosion susceptibility. For most Cr-containing alloys, which include stainless steels, Ni-based, and Co-based alloys, it is well-known that during alloy heat treatments, Cr-rich carbides precipitate at grain boundaries. As the carbides grow, Cr becomes segregated to the boundaries, leading to the local regions adjacent to the grain boundaries are depleted of Cr. In addition to the Cr concentration near grain boundaries, the geometry of the grain boundary lattice can also affect carbide formation and grain boundary sensitization. Dislocations and lattice defects at the grain boundaries can act as sinks for solutes, resulting in preferential sites for the breakdown of the protective oxide films. As shown in the grain-boundary assisted crevice corrosion (GACC) model, coincident site lattice (CSL) boundaries in CoCrMo alloys inhibit the depletion of Cr and the formation of carbides, leading to improved corrosion resistance [98, 99]. Furthermore, the GACC model has also shown that the severity of corrosion, as quantified by the sizes

of the corrosion crevices, is linked to the grain boundary interfacial energies. High-energy boundaries are most susceptible to corrosion attack, since there is a large amount of Cr depletion and sufficient thermodynamic driving force for the removal of the boundary. Which oxides form at the earliest time and how do they change over time? How is each oxide phase formed and what mechanism is the rate-limiting step during growth? Do the oxides have different combinations of crystallographies and chemical compositions in the presence of grain boundaries? These questions remain unanswered.

In this chapter, I will elucidate that early-stage oxidation behavior of a CoCrMo alloy is affected by kinetic and thermodynamic factors involving the relative diffusion rate of cations and oxygen. Furthermore, I will demonstrate that the kinetics and thermodynamics of oxide growth are influenced by the presence of grain boundaries by characterizing the inward oxide growth at grain boundaries that result in grooving. The microstructures and chemical compositions of oxide layers formed at 700 °C for 30 min in a CoCrMo alloy are analyzed with TEM, providing insight into how oxides initiate and evolve in early-stage oxidation, and two different growth regimes were shown. A duplex layer structure of an outer spinel oxide layer that could either be Co-rich or Cr-rich and a thin inner Cr-rich corundum oxide layer was observed. The spinel oxide growth is dominated by cation diffusion, so it grows outward. The corundum oxide growth is dominated by oxygen diffusion into the metal, resulting in inward oxide growth. Near the metal-oxide interface, the spinel phase contains a significant concentration of pores, and Cr dopants exceeding thermodynamically stable compositions. In addition, the inward growth of corundum oxides at selected grain boundaries is observed, resulting in kinetic Wulff shapes that were previously observed in corrosion crevices during grain-boundary assisted crevice corrosion (GACC) in CoCrMo alloys [98, 99]. I will conclude by drawing some parallels between the grooving at grain boundaries during oxidation to the corrosion crevices at grain boundaries during electrochemical corrosion and expanding the scope of the GACC model to include oxidation at grain boundaries.

3.2 Methods and Materials

3.2.1 Sample Preparation

A wrought low-carbon CoCrMo (Aubert & Duval Corporation) bar was sectioned into discs with a diameter of 12 mm and height of 7 mm. The alloy composition, in accordance to ASTM F1537, is given in Table 3.1. One surface of the 12 mm diameter alloy disc was ground and polished using a semi-automatic Struers MD-Gekko polisher. The alloy samples were mechanically polished through a sequence of progressively finer sizes of silicon carbide abrasive papers from 320-grit up to 1200-grit with water lubrication. Next, the polishing was performed using water-based 3 μm and 1 μm diamond suspensions dispersed on a cloth-based polishing pad until the alloy surfaces had a mirror finish. The final polished surfaces were characterized by collaborators at Rush University Medical Center with a Zygo NewView 6300 white light interferometer and the surface roughness values were on the order of $R_a \leq 10$ nm. The as-received CoCrMo alloys contained grains 3-5 μm in diameter with twinned microstructure, as verified by SEM imaging prior to oxidation treatments. The polished samples were oxidized in flowing oxygen at 700 °C for 30 min in a Carbolite STF 15/180 tube furnace. The ends of the quartz tube were sealed, and oxygen gas was flowed through the tube furnace with a $p\text{O}_2$ of 0.5 atm.

Table 3.1. Composition of low-carbon CoCrMo alloy in at.%

Co	Cr	Mo	C	Ni
Balance	31.1	3.6	< 0.7	< 1.0

3.2.2 Electron Microscopy

SEM characterization was performed on the FEI Quanta 650 SEM operating at an accelerating voltage of 20 kV. The TEM lamellae samples were lifted out from three separate grain boundary regions after the deposition of Pt protective layers on the oxidized surface in a dual-beam FEI Helios Nanolab FIB system. The samples were then thinned using a beam energy of 30 kV. A final cleaning step was performed at 2 kV to reduce the amorphous layer

thicknesses in the TEM lamellae. TEM and HAADF imaging were performed on the JEOL ARM-300F operated at 300 kV and the aberration-corrected JEOL ARM-200CF operated at 200 kV. The collection angles between 90-220 mrad were used for HAADF imaging. EDS analysis was performed with Oxford windowless silicon drift detectors on the ARM-200CF and ARM-300F, and EELS was performed with a Gatan Quantum EELS spectrometer.

3.3 Results

SEM images of the CoCrMo alloys oxidized for 0.5 h show the surface morphology on different length scales. In Figure 3.1a, the grain boundary network can be observed, with some grain boundaries and to a certain extent, individual grains, decorated with dark void-like features, which are likely inward growing oxides. Additionally, the light features distributed throughout Figure 3.1a resemble the morphology of a cluster of outward growing oxide particles. On a finer length scale, grains of 3-5 μm in diameter, similar to the microstructure of the as-received alloy, are clearly visible and the bright oxide nanoparticles are well-distributed across most of these grains as shown in Figure 3.1b. Many grain boundaries contain similar dark features that are indicative of an inward growing oxide. Although the inward growing oxides at the grain boundaries do not appear to be continuous or evenly distributed, there are two interesting observations to note. Firstly, there is a preferential nature to the amount of inward growing sites at some grain boundaries and certain other boundaries contain little to none of the dark features. Secondly, even though the distribution of the oxides along the grain boundary length is non-uniform, the entire boundary exhibits a darker image contrast in comparison to the grains. This image contrast can be attributed to the initial stages of grain boundary grooving as a consequence of the inward growing oxides.

To further clarify the inward and outward growth of oxides, a low magnification ADF image, as seen in Figure 3.2, shows the uniformity of the outer oxide layer and that multiple inward growing oxides can be found at selected grain boundaries. Figure 3.3 shows the typical duplex oxide microstructure on the oxidized CoCrMo surface. The inner layer of the

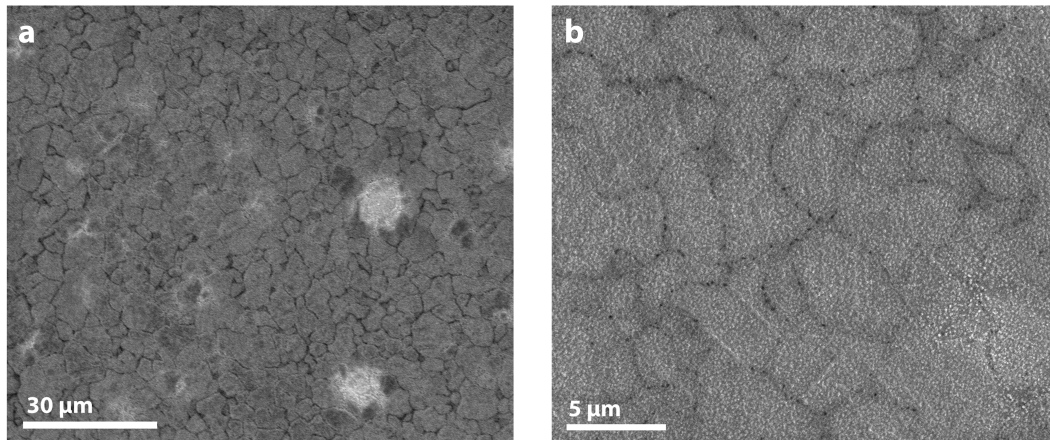


Figure 3.1. SEM images of the CoCrMo sample after oxidation. (a) An overall view shows that selected grain boundaries and grains have darker contrast, indicating inward oxide growth. (b) On the finer scale, bright oxide nanoparticles are well-distributed across most grains and inward growing oxides are found mainly at grain boundaries but can also occur at individual grains.

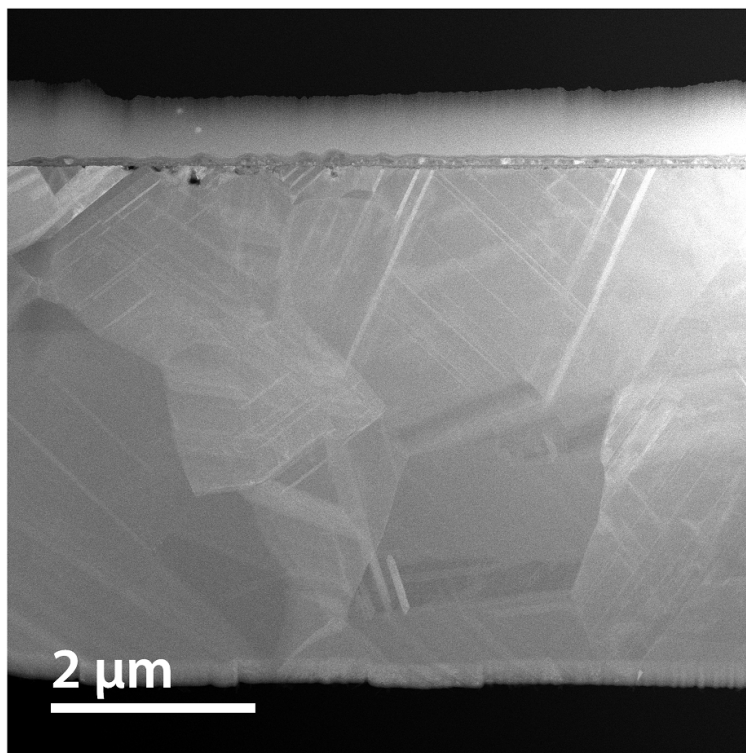


Figure 3.2. An ADF image shows the uniformity of the outer oxide layer and that multiple inward growing oxides, located on the left side of the image, can be found at selected grain boundaries.

oxide consists of primarily polycrystalline corundum structure, and the outer layer consists of coarse-grained spinel structures. The oxide crystallography was determined by electron diffraction. From the compositional linescan and EDS mapping shown in Figure 3.4, the inner corundum oxide layer is confirmed to be Cr-rich and the outer spinel oxide is Cr-rich near the corundum-spinel interface and becomes more Co-rich near the outer surface of oxide. The Cr concentrations in the spinel oxides have been observed to exceed the thermodynamically stable stoichiometry of the cobalt chromium spinel phase (CoCr_2O_4), confirming that nonequilibrium solute capture can occur in spinel oxides. There is also Co in the corundum layer which is not unexpected, as Co is soluble in Cr_2O_3 and can form a continuous solid corundum solution $\text{Co}_{2-x}\text{Cr}_x\text{O}_3$ for x less than $\sim 4/3$. I will return to this result later in this chapter.

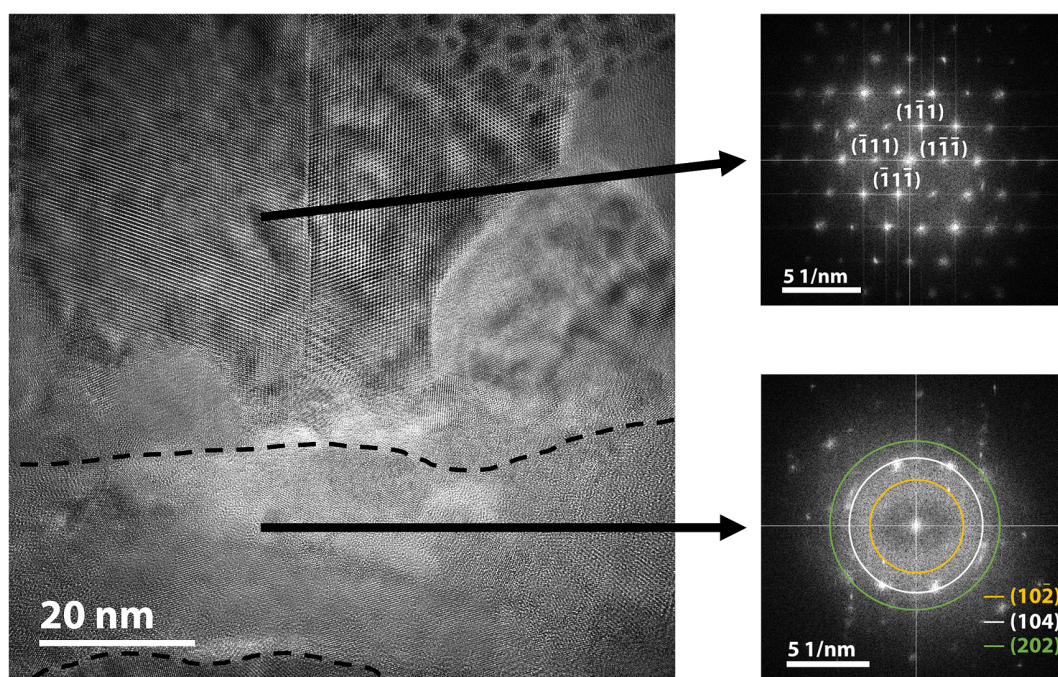


Figure 3.3. Morphology of the duplex microstructure. The outer oxide consists of spinel oxide islands and the inner oxide is a corundum oxide layer, as verified by the FFT of the two regions in the oxide. The lower dashed line marks the metal-oxide interface and the upper dashed line is the approximate location of the corundum-spinel interface.

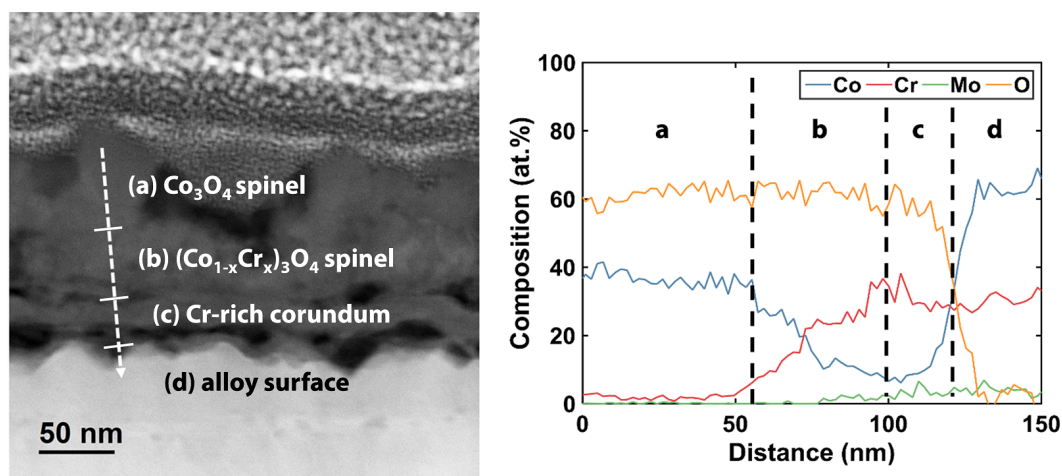


Figure 3.4. HAADF image with a corresponding compositional linescan of the duplex oxide microstructure. The outer oxide includes (a) a Co_3O_4 spinel and (b) a nonstoichiometric $(\text{Co}_{1-x}\text{Cr}_x)_3\text{O}_4$ spinel. The inner oxide is composed of (c) a Cr-rich corundum layer adjacent to the (d) alloy surface.

Although the duplex oxide microstructure and the constituent oxide phases can be observed throughout the sample, there are deviations at the grain boundaries. At selected grain boundaries such as the one shown in Figure 3.5a, Cr-rich corundum oxide grows inward in addition to the polycrystalline corundum layer. In Figure 3.5b, EDS mapping indicates that the inward growing oxide depletes the Cr from the local region at the metal-oxide interface. At another grain boundary shown in Figure 3.6, the inward growing phase does not only consist of just the Cr-rich corundum but also includes a Co-rich oxide, that has rocksalt crystallography. In Figure 3.7, a third case shows that the inward growing Co-rich rocksalt oxide is surrounded by the Cr-rich corundum layer, and the outward growing oxide contains corundum as well as the spinel phase. We note that the inward growing oxides are phase-separated in all of the observed cases.

HAADF images show the atomic-scale details of the duplex oxide structure. Figure 3.8a is a lower magnification image, with the brighter region (higher mass-density) at the bottom of the image representing the alloy. Figure 3.8b shows the metal-oxide interfacial region in more detail, where the corundum layers are adjacent to the metal surfaces. In the corundum layer, at the metal-oxide interface, there are also isolated spinel oxide inclusions.

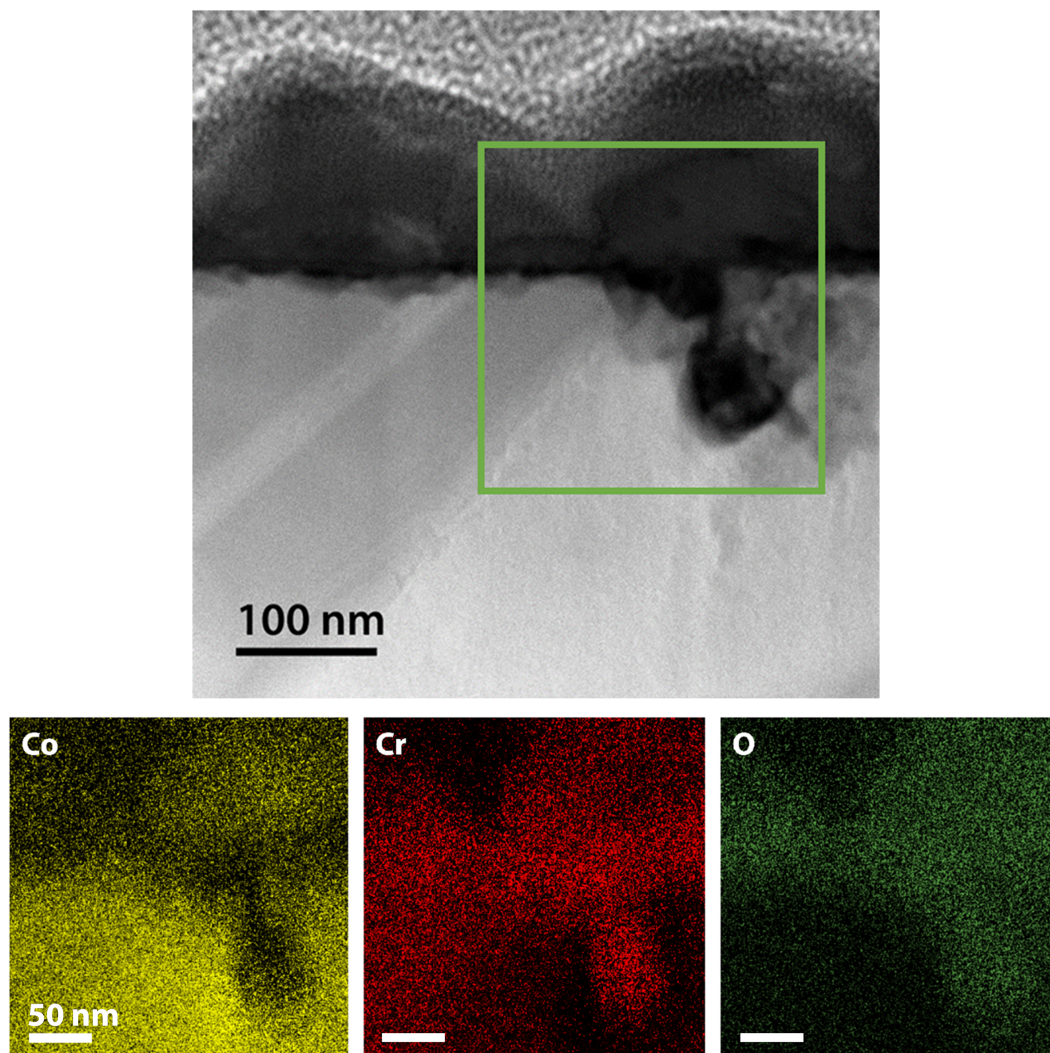


Figure 3.5. Inward growth of Cr-rich corundum oxide at a grain boundary. Corresponding EDS mapping indicates that the local region around the corundum oxide is depleted in Cr.

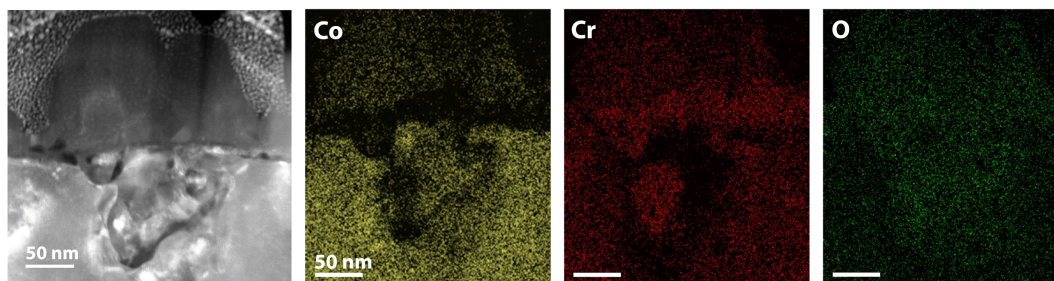


Figure 3.6. A second case of inward oxide growth. The inward oxide comprises of both Cr-rich corundum and Co-rich rocksalt.

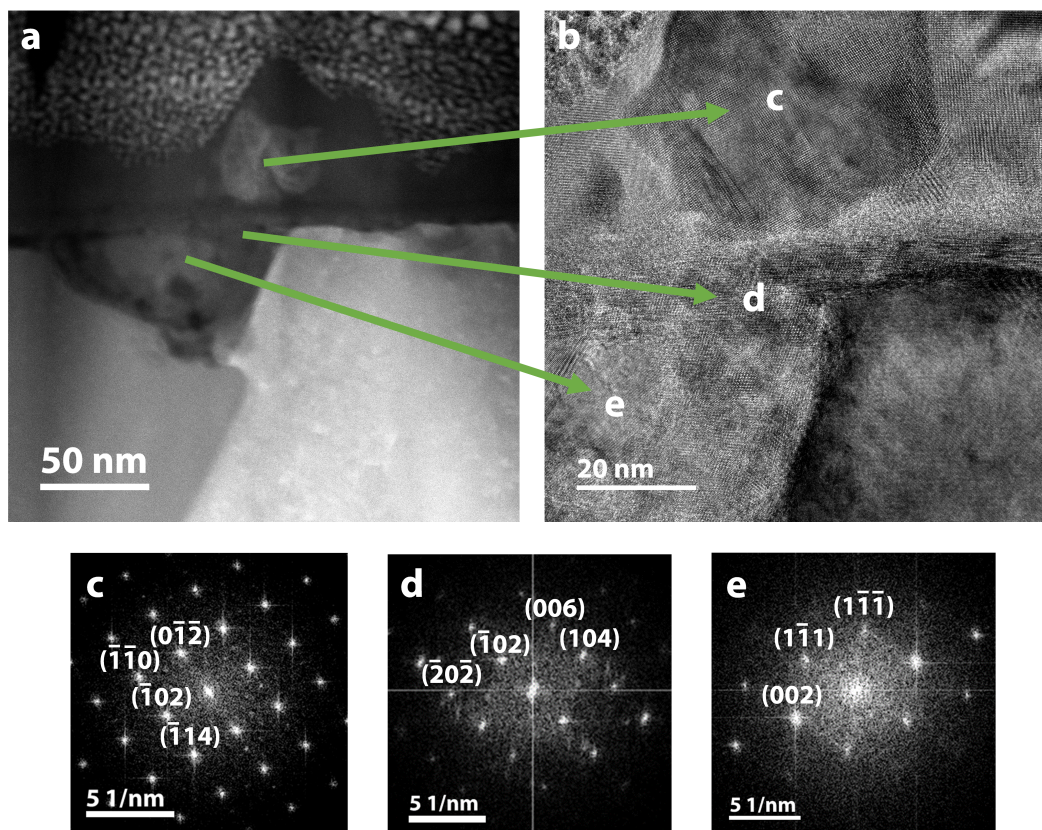


Figure 3.7. A third case of inward oxide growth at grain boundaries show that the inward growing oxide is mostly Co-rich rocksalt and the outward growing oxide contain a Cr-rich corundum phase along with a Co-rich spinel oxide. (a) HAADF image shows that outward growing island is phase separated. (b) A TEM image captures the (c) outer oxide, (d) inner Cr-rich layer, and (e) inward growing rocksalt. FFTs of the regions depict the corresponding crystallography in those regions.

The morphology of the oxides provides additional information about the formation of oxide phases at CoCrMo surfaces. There is a size variation across different grains and grain boundaries: the spinel oxide phases have coarser grains with sharper facets in certain grains, while other grains have smaller spinel oxides particles. This is also apparent at grain boundaries, as certain boundaries actually have enhanced secondary electron contrast, indicating that there are larger and more faceted outward growing particles. However, the oxide shows primarily inward island growth at most grain boundaries under a flat corundum oxide thin film. The inward growing oxides have different morphologies, depending on whether it is the Cr-rich corundum or the Co-rich rocksalt. The shape of the resulting

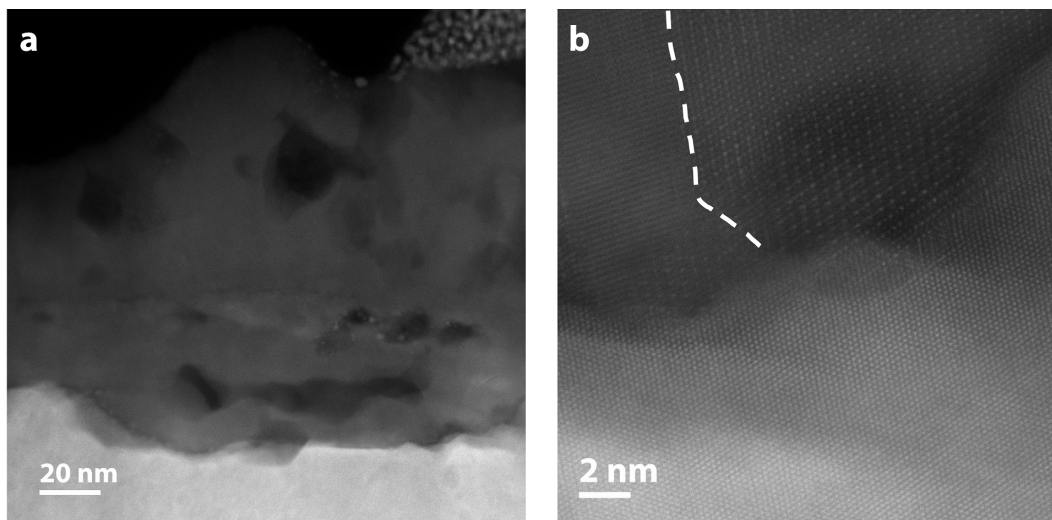


Figure 3.8. HAADF images of the oxide morphology. (a) The interface between the inner and outer oxide layers contains additional voids, demonstrating the result of outward cation diffusion and inward oxygen diffusion. (b) Isolated spinel particles can also be found throughout the corundum layer, even near the metal-oxide interface. The left side of the dash line shows a corundum lattice spacing, while the right side shows a spinel lattice spacing.

grain boundary groove due to the oxidative attack would also appear to be affected by the crystallography of the growing oxide. Lastly, there are typically a significant number of pores at the corundum-spinel interface, demonstrating the bidirectional growth that is occurring at the original metal surface. While the corundum generally grows inward, cations diffuse through the corundum layer to form spinel particles, leaving Kirkendall voids at the interface. For the instances where the rocksalt grows inward, cation diffusion through the oxide is more prevalent, resulting in an excess of Cr which could either form a combination of corundum and spinel or a nonstoichiometric spinel in the oxide that grows outward.

3.4 Discussion

The direction of oxide growth corresponds mainly to the species that dominate diffusion. For instance, inward oxide growth occurs when diffusion is dominated by oxygen diffusion and outward oxide growth occurs when diffusion is dominated by cation diffusion. For the intermediate temperature range, it has been established that oxygen diffusion often dominates the growth of corundum, so it grows inward in most cases. For the spinel phase, there are

some complexities as there are large spinel nanoparticles that occupy the outer oxide layer and small inclusions throughout the Cr-rich corundum layer and at the corundum-spinel interface. From previous experimental studies of Co-Cr spinel formation [112, 113], the reaction is driven by Co cation diffusion as the diffusivity of Co is well-known to be larger than the diffusivity of Cr through both corundum and spinel oxides. Additionally, the large particles grow outwards, demonstrating that cation diffusion dominates spinel growth. The fine spinel inclusions found in the inner Cr-rich layer and at the corundum-spinel interface are likely the result of the solid-state reaction between the rocksalt and the corundum phases.

During the initial stages of oxidation similar to the conditions used in this chapter, corundum Cr_2O_3 and rocksalt CoO form simultaneously. As a continuous oxide layer builds up, the oxidation becomes diffusion controlled. It has been shown that in Co-Cr systems that Co diffuses outward through the rocksalt phase via a vacancy mechanism as oxidation progresses, resulting in outward growth of the oxide [101]. Meanwhile, the oxygen diffuses in, forming discrete corundum particles at the metal-oxide interface. At intermediate temperatures, preferential internal oxidation occurs at grain boundaries, as the higher oxygen and metal diffusivities at grain boundaries are significant. The corundum particles at the metal-oxide interface and the grain boundaries would restrict Co cation diffusion, leading to pores forming at the surface of the corundum phase. This increase in porosity would also further decrease solid-state diffusion, while promoting the transport of oxygen gas to the inner oxide, which is composed of discontinuous corundum islands and voids. As oxidation continues to progress, the fast, inward oxygen transport will oxidize excess Co to form rocksalt, and the corundum would react with the rocksalt to form spinel oxides, which will restrict further outward cation diffusion from the metal and inward oxygen diffusion. The outer rocksalt CoO will continue to evolve as it will oxidize to the spinel Co_3O_4 phase, which is thermodynamically stable at $700\text{ }^\circ\text{C}$ [114].

However, Co-Cr systems are still inferior in comparison to Ni-Cr systems due to their low oxidation resistance [115]. One of the reasons that Co-Cr have lower oxidation resistance is

that Co cations are significantly more soluble in Cr_2O_3 than Ni cations are, resulting in a continuous corundum solid solution $\text{Co}_{2-x}\text{Cr}_x\text{O}_3$ for x less than $\sim 4/3$ [116] and allowing Co cations to diffuse through the corundum solid solution [109]. Another reason that Co-Cr have lower oxidation resistance is that the kinetics of forming the $(\text{Co}_{1-x}\text{Cr}_x)_3\text{O}_4$ spinel are fast, resulting in a defective porous oxide layer and morphological instabilities in the rocksalt oxide [113]. While the pores in the oxide limit the availability of sites for solid-state diffusion, they enable rapid inward oxygen diffusion thereby enhancing oxidation. Additionally, even though corundum Cr_2O_3 forms in most Co-Cr oxidation cases, the formation the spinel CoCr_2O_4 suggests that Cr_2O_3 is consumed in this reaction. Although the cation diffusivities in the CoCr_2O_4 phase is smaller than their diffusivities in Cr_2O_3 , the spinel will form discontinuously as the available corundum phase at the metal-oxide interface is not a complete layer.

From the results herein, we observe that the addition of Mo can address some of these shortcomings. First, it has been shown for NiCrMo alloys that Mo substantially promotes corundum formation in early-stage oxidation [40, 41, 117]. This should extend to CoCrMo alloys too, as they show significant pitting resistance in comparison to CoCr alloys in different corrosion environments, suggesting that Mo plays a direct role in the inhibition of corrosion [118, 119]. As shown in Figure 3.3, the morphology of the inner corundum layer appears to be continuous, but may contain spinel inclusions, defective regimes, and voids as the image contrast in the inner oxide layer is not uniform. The EDS mappings shown in Figures 3.5 and 3.6 indicate that the Cr-rich inner oxide forms continuously at the metal surface, suggesting that the corundum layer formed a uniform layer rather than discrete particles at the metal-oxide interface. Furthermore, although Figure 3.8b shows that it is possible to also observe spinel oxides in the inner oxide at the metal-oxide interface, these phases are well-ordered and provide almost complete coverage at the metal surface, limiting further oxygen and cation diffusion. This also shows that although Cr_2O_3 can be consumed in the formation of spinels, there is still a large amount of corundum remaining in the Cr-rich inner oxide. While the Mo may improve the blocking effect at the metal-oxide interface, the oxide

morphology contains a large amount of pores, as shown in Figure 3.8a. The porosity in the oxide scale appears to form independent of temperature in Co-10Cr alloys [101]. Since this remains an issue for CoCrMo alloys at moderate temperatures, additional alloying elements may be needed to form continuous corundum and spinel layers with minimal porosity during oxidation.

Lastly, we turn to the grain boundary dependent oxide growth as shown in Figure 3.1. Intergranular corrosion in CoCrMo alloys has been shown to occur preferentially, with randomly oriented high-energy grain boundaries corroding first [95, 98]. In coincident-site lattice (CSL) boundaries, there is also a hierarchy with respect to corrosion resistance of individual boundaries, as low-symmetry CSL boundaries have much more severe crevice corrosion compared to high-symmetry or twin boundaries [99]. This mechanism is known as the grain-boundary assisted crevice corrosion (GACC) model. Although the GACC model uses grain boundary interfacial energies as a variable, it also considers the level of Cr depletion near grain boundaries as a direct result of grain boundary sensitization, which describes the Cr depletion as Cr diffuses to boundaries to form carbide second phase particles. The boundaries more prone to corrosive attack are the ones that have significant carbide formations, since the Cr is depleted, resulting in their inability to form protective oxides.

We argue that a similar effect is taking place when CoCrMo alloys are exposed to an oxidative environment. As the oxygen diffuses into the alloy initially there is preferential internal oxidation at the grain boundaries. This is made possible by the Cr migration via the grain boundaries to the oxidizing surface, as grain boundaries are high diffusivity paths in metals. As the oxides form at the surfaces above the grain boundaries, the regions immediate to the boundary becomes depleted in Cr, leading to grain boundary grooving as the amount of protective corundum formed near the boundary surface is decreased. This may also result in the likelihood of inward rocksalt formation, which is observed in Figures 3.6 and 3.7, near the corundum phase formed at the boundary. However, not all inward growing corundum forms uniformly, and this is likely due to the grain boundary interfacial energy contributions

to the kinetic effects of oxide growth. For instance, Equation 3.1 demonstrates the velocity (v) of grain boundary grooving:

$$v \propto \exp\left(\frac{-[\Delta G_{\text{oxide}} + \gamma_{\text{GB}}A_{\text{GB}}]}{RT}\right) \quad (3.1)$$

Where ΔG_{oxide} is the free energy of formation of the oxide, γ_{GB} is the interfacial energy of the grain boundary, and A_{GB} is the area of the grain boundary. As the grain boundary groove grows, the grain boundary area will decrease and the surface area will increase, so it is imperative to consider the excess surface free energy and the groove geometry as the grain boundary interfacial energy is directly related to those values, assuming there is local equilibrium at the triple junction. As a result, grain boundary groove studies typically use the dihedral angle of the groove (Ψ) to determine the relative grain boundary energy ($\gamma_{\text{GB}}/\gamma_s$):

$$\frac{\gamma_{\text{GB}}}{\gamma_s} = 2 \cos\left(\frac{\Psi}{2}\right) \quad (3.2)$$

Where γ_s is the excess surface free energy. According to the relationship in Equation 3.2 and experimental studies of thermal grooving in the literature [120, 121], grain boundaries with a low relative energy will form grooves with larger dihedral angles. As a result, deep oxide grooves are likely forming at high-energy grain boundaries. The relationship between grain boundary energy and oxide groove geometry merits further work.

This demonstrates that the high-energy boundaries would oxidize preferentially and form Cr_2O_3 quickly, depleting the surrounding region in Cr thereby exposing it to the formation of the less protective rocksalt CoO. Consequently, is it more likely for solute capture to occur at high-energy boundaries due to the chemical inhomogeneities and increased diffusion kinetics. However, in all cases, the early-stage oxidation behavior shows that the Cr-rich layer is also able to stabilize above the grain boundary groove. Since the CoCrMo alloy sample used in this chapter contained fine grains (3-5 μm grain diameter) as seen in Figure 3.2, the Cr diffusion to the surface region is enhanced due to the large density of grain boundaries,

and the external Cr_2O_3 layer can also grow laterally to the grain interior and neighboring boundaries, eventually providing coverage to the entire surface. A previous study of an austenitic stainless steel oxidized at 700 °C shows that a grain size below 8 μm is necessary to form a complete Cr-rich layer [122], as intragrain regions will generally form non-protective spinel oxides in the interior oxide, which can allow additional cations to continue to diffuse out at a fast rate.

Although the Cr-depletion and inward rocksalt formation were mediated by the high density of grain boundaries, the reduction of high-energy randomly orientated grain boundaries may also play a role in supporting the chemical uniformity of the alloy surface. Grain boundaries will remain to be preferential sites for oxidation; however, if the kinetics of oxide formation could be more consistent across individual boundaries, the protective surface oxides would be uniform morphologically and chemically, resulting in enhanced oxidation resistance. According to the GACC model, CSL boundaries are effective against corrosion initiation, which will also allow them to maintain protective surface oxides during long-term corrosion. Although the true interfacial energies of CSL boundaries are difficult to predict accurately, general trends between grain boundary misorientation and oxide crystallography and chemistry can be related with a combined electron backscatter diffraction and TEM approach, which was used to develop the GACC model, as shown in Figure 3.9. The surface oxides in the corrosion crevices of CSL boundaries and high-energy boundaries were neglected in the GACC model and can certainly lead to additional insights into the oxidation and corrosion resistance of CoCrMo alloys in a variety of applications.

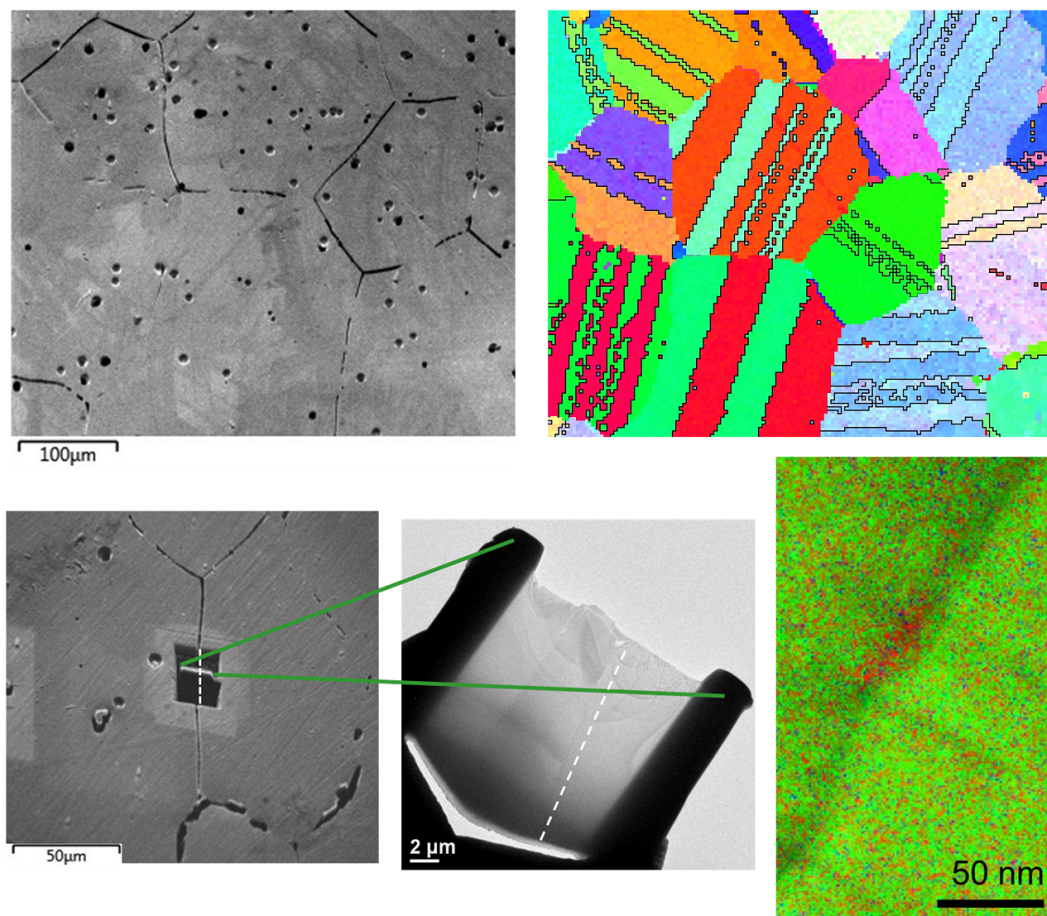


Figure 3.9. A multiscale approach, which involves EBSD mapping, TEM imaging, and EDS analysis of grain boundary carbides can be used to understand the relationship between preferential corrosion, grain boundary misorientation, and Cr depletion. Adapted from [98].

3.5 Conclusions

Early-stage oxidation of CoCrMo alloys shows that there are several mechanisms that influence the growth and evolution of oxides at intermediate temperatures. First, the addition of Mo promotes the formation of corundum, which significantly reduces outward cation diffusion and inward oxygen diffusion. However, as cation diffusion is restricted through the corundum, the initially formed rocksalt oxide becomes porous, accelerating inward oxygen diffusion at the corundum and metal-oxide interface. Next, the interior rocksalt reacts with the corundum to form spinel at the corundum surface; however, spinel inclusions can also be found at the metal-oxide interface. The spinels have low cation diffusivities, but contain

many pores, which lead to further oxidation. Finally, inward oxide growth at the grain boundaries is promoted by fast oxygen ingress and large outward Cr diffusion. As a result, corundum oxide particles form preferentially at grain boundaries and are typically inward growing. The rapid formation of corundum leads to a local depletion of Cr, exposing the neighboring areas to enhanced oxidative attack and enabling the inward growth of rocksalt oxides. However, the high density of grain boundaries provide sufficient Cr cations for the formation of a Cr-rich inner oxide layer and this layer can also grow laterally to the grain interior (at the surface) and neighboring boundaries, eventually providing coverage to the entire alloy surface. With more careful studies of the oxidation behaviors of different grain boundary structures such as low-energy CSL boundaries, it is possible to further optimize the oxidation performance of CoCrMo alloys and adapt them to many other applications.

Preferential Interaction Between Hyaluronic Acid and Cr in Simulated Biological Conditions

In Chapter 3, I showed that nonequilibrium solute capture can occur in the formation of spinel oxides, especially at high-energy grain boundaries, during the early-stage oxidation of CoCrMo alloys. Since the formation of nonequilibrium oxides requires both thermodynamic metastability and sufficiently fast kinetics, solute capture will likely occur in many cases of high-temperature oxidation and almost all cases of aqueous corrosion [40, 123]. In addition, extensive experimental results have suggested that nonequilibrium oxides may have unusual combinations of crystallographies and chemical compositions, requiring both pieces of information to fully characterize the oxide layers formed during oxidation and corrosion. In this chapter, I will examine a few different cases of aqueous corrosion in CoCrMo alloys to compare the crystallography and chemistry of the oxides formed in each case. These insights can establish additional degradation mechanisms to understand the electrochemical behavior of CoCrMo in biomedical applications.

CoCrMo alloys have been heavily used in orthopedic prosthesis such total as hip replacements since they have a good combination of corrosion resistance, wear resistance, high tensile and fatigue strength, and high biocompatibility. However, these alloys are still susceptible to wear and corrosion *in vivo*. As a result, metallic nanoparticles and ions are released from the implant material [124, 125] and can lead to many complications, including inflammation [126–128], aseptic implant loosening [129, 130], and metal accumulation in organs distant from the implant [131]. There have been significant efforts to study the electrochemical behaviors of CoCrMo surfaces in different simulated biological environments by varying the applied electrochemical potential [90–93, 118, 132–138]. Other studies focused on the tribological behavior by characterizing friction, wear, and tribolayer formation on the alloy surfaces in biological lubricants such as simulated synovial fluids [139–142]. Additionally,

several studies incorporated electrochemical measurements into macroscopic tribological tests to understand tribocorrosion mechanisms and synergistic interactions between corrosion and wear in CoCrMo alloys [17, 18, 143–146]. As discussed last chapter, the morphology, chemistry, as well as protectiveness of oxide scales vary dramatically depending on the oxidative conditions used. Similarly, the formation of oxide films on CoCrMo surfaces is very sensitive to the simulated biological conditions, so each of these test protocols would have complex effects on the properties of the oxide and influence the degree of ion release from the alloy.

This chapter will focus on the oxide layers on CoCrMo alloys that are corroded in simulated synovial fluids. Recent efforts to establish the electrochemical behavior of CoCrMo in a model synovial fluid has shown that hyaluronic acid (HA), which is a viscoelastic macromolecule that plays an important role in the lubricious properties of synovial fluid [147], modifies the passive oxide film and lowers the corrosion resistance of the alloy [48, 148]. TEM characterizations of the oxide layers revealed that samples corroded in HA exhibited mostly rocksalt crystallography and are almost completely depleted in Cr, suggesting that the Cr interacted with HA to form complexes disrupting the formation of a passive Cr_2O_3 layer. However, the addition of proteins results in a significantly lower anodic current and higher corrosion resistance, demonstrating that proteins can compensate for the preferential interaction between HA and Cr during corrosion in model synovial fluids. The work in this chapter was done in collaboration with Dr. Simona Radice, Dr. Michel Laurent, and Dr. Markus Wimmer at the Department of Orthopedic Surgery, Rush University Medical Center.

The structure of this chapter is as follows. First, I will provide a brief background on some commonly used protocols to study corrosion, tribology, and tribocorrosion in CoCrMo alloys. I will also review some general mechanisms describe the corrosion and tribocorrosion in albumin proteins and HA, which are important components of synovial fluid. Next, I will show the TEM results indicating that the oxide layer in CoCrMo corroded in HA contains mostly Co, suggesting the weakening and eventual dissolution of Cr_2O_3 can be related to

the preferential interaction of HA and Cr and the precipitation of Cr organic complexes. This result will then be correlated to the oxides formed in early-stage aqueous corrosion of CoCrMo in a Cl^- -containing electrolyte, indicating similar structures but different kinetics taking place in the two cases. Lastly, some preliminary electrochemical data will be shown to indicate that the presence of proteins in the synovial fluid can significantly decrease the anodic currents on the macroscopic level, suggesting that proteins can possibly compensate for interaction between HA and Cr and preventing the accelerated corrosion as observed in similar tests without proteins.

4.1 Corrosion, Tribology and Tribocorrosion in CoCrMo Alloys

The elucidation of electrochemical reactions and the structure and chemistry of the surface oxide layers are critical to understand the interactions between the CoCrMo implant and the biological environment. The electrochemical behavior of CoCrMo alloys in simulated physiological solutions have been extensively studied in the literature, with most studies focusing on simple saline solution [91, 132], simulated physiological fluid with various salts [91], Hank's solutions [90, 92, 118], and phosphate buffered saline (PBS) solution [93, 135, 136]. In almost all of these studies, electrochemical techniques such as potentiodynamic and potentiostatic polarization, cyclic voltammetry, and electrochemical impedance spectroscopy were used to measure the electrochemical behavior of the alloy in passive and transpassive states. Additionally, *ex situ* surface analysis such as XPS, Auger electron microscopy [90–92, 94, 137, 138], or Raman spectroscopy [134] were carried out to characterize the structures and compositions of the oxide films on the alloy surface. Although local chemical and crystallographic information of oxide films are lacking in these studies, general trends of how inorganic ions, proteins, and biomolecules influence the passive film and the electrochemical behavior of CoCrMo can be elucidated.

Since synovial fluid is the natural biological environment for a CoCrMo joint implant, the electrochemical behavior of CoCrMo surfaces in simulated synovial fluids is important.

Some studies have focused on the role of albumin [132, 133, 136, 149–151], which is the most abundant protein in the synovial fluid, and how it interacts with the metal and the metal oxide. While albumin can form thick adsorption biofilms which can impart enhanced corrosion resistance, the proteins may not always form a complete adsorption layer and can also modify the chemical composition of the passive oxides and the kinetics of cathodic and anodic reactions taking place [94]. In fact, it has been shown that in certain conditions proteins can have an initial beneficial effect, and then transition to a detrimental effect by accelerating corrosion [152]. In long term corrosion studies, proteins can weaken metal-oxide bonds as they form complexes with metals. Although typically a slow process, direct protein interactions with metals can be rapid when the passive oxide is defective or damaged under mechanical loading conditions, resulting in non-protective surface oxides and enhanced localized corrosion [153]. The schematics of such processes are shown in Figure 4.1. There are significantly fewer studies on the electrochemical effect of HA [133, 148, 154, 155] and the interactions between HA and proteins and their effect on electrochemical properties has only been explored very recently [48].

As CoCrMo implants undergo mechanical wear, their tribological and tribocorrosion behaviors have been widely investigated [17, 18, 143, 144, 146]. Typical lubricants chosen for these experiments contain a combination of phosphate saline solutions and bovine serum to simulate the inorganic salt and protein content of physiological synovial fluid. Due to the lubricious nature of HA [147], it is often added to the model fluids during tribological testing to understand how it enhances the formation of a tribolayer and modifies the rheological properties of the fluids [3, 139, 156]. However, the combinations of wear and corrosion mechanisms can lead to a very complex environment near the contact zone of sliding surfaces. For instance, fretting wear can induce cracking in thin passive oxide layers, exposing the metal surface directly to the electrolyte. This can be reduced by proteinaceous tribofilms, which are generated as a result of tribochemical reactions [17, 18], as they can form a barrier to protect the oxide film and also lubricate the hip joint bearing surfaces and improve the overall wear

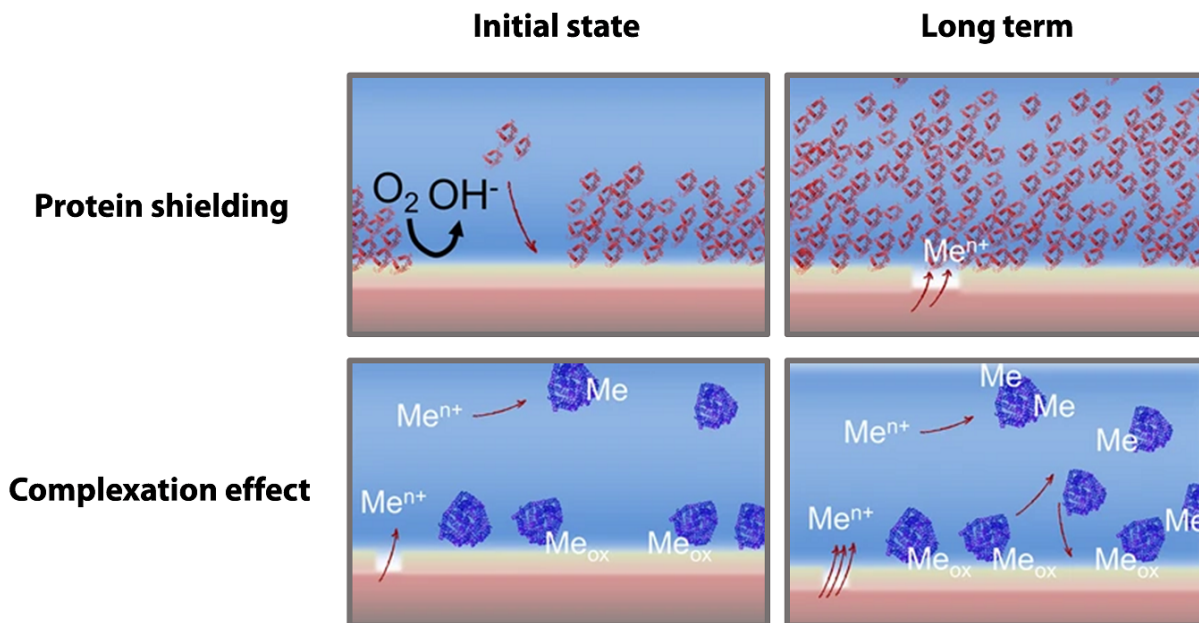


Figure 4.1. Schematic illustration of the effect of proteins on material degradation over time. Although proteins can reduce corrosion initially, they may cause pits or pinholes to form in the oxide layer and cause increased corrosion. The complexation effect shows that metal can form complexes with proteins and can result in increased corrosion/dissolution rates. Adapted from [153].

resistance. Lastly, Mo may further assist in the deposition of a tribofilm during CoCrMo tribocorrosion. Recent findings suggest that Mo^{6+} ions can enhance the protective tribofilm formation by interacting with proteins in the physiological medium to form a protein-rich film on metallic surfaces [157]. This finding combined with the fact the Mo can promote corundum formation in the passive oxide layer in Cr-containing alloys [40, 41, 117, 158] may explain the overall enhanced tribocorrosion resistance of CoCrMo alloys relative to CoCr alloys.

4.2 Methods and Materials

4.2.1 Alloy Preparation

The preparation of CoCrMo discs for corrosion treatment follows the same procedures as described previously in Section 3.2.1.

4.2.2 Corrosion in Model Synovial Fluid

In order to investigate the interactions of CoCrMo alloys with hyaluronic acid (HA) and bovine serum albumin (BSA), which are constituents in human synovial fluid, they were added to a cell culture medium (RPMI-1640) base solution to form electrolyte solutions that were tested in a three-electrode electrochemical cell that was connected to a Gamry Series G 750 Potentiostat. Details of the electrochemical test set-up can be found in Section 2.1.2.

The electrochemical test protocols used in this chapter follow these steps: (1) initial open circuit potential (OCP) for 1-3 h, (2) potentiostatic electrochemical impedance spectroscopy from 50 kHz to 0.005 Hz with 10 mV vs. the open circuit potential, (3) cathodic polarization with forward and reverse scan between -0.1 V (OCP) to -1 V (vs. Ag/AgCl) with a scan rate of 2 mV/s, (4) open circuit stabilization for 1 h, and (5) anodic polarization with forward and reverse scan between -0.1 V (OCP) to +1.3 V (vs. Ag/AgCl) with a scan rate of 2 mV/s. More details about the rationale of electrochemical protocol can be found in [48].

4.2.3 Aqueous Corrosion

Details of the preparation of TEM samples from CoCrMo discs and aqueous corrosion can be found in Section 2.1.

4.2.4 Electron Microscopy

SEM and TEM characterization follow the same procedures as described previously in Section 3.2.2.

4.3 Results

In Figure 4.2, there appears to be a thick organometallic film after corrosion in electrolyte solutions containing RPMI + BSA + HA, as the film has not completely delaminated from the surface. The edges around the RPMI + HA (no protein) sample also showed the presence of a thick film as thick green flakes are distributed along the circumference of the alloy surface. TEM analysis of the oxide layers in the RPMI + HA sample shows that the oxide islands

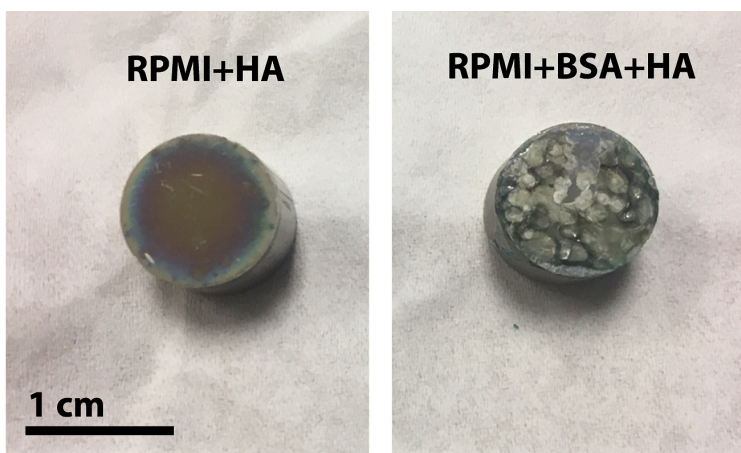


Figure 4.2. CoCrMo discs corroded in RPMI + HA and RPMI + BSA + HA electrolytes indicate the presence of films with different thicknesses.

are polycrystalline and have rocksalt crystallography, see Figure 4.3. In Figure 4.4, HAADF imaging and a corresponding EDS linescan verified that the rocksalt oxide contains almost no Cr, with the exception of minor Cr content near the metal-oxide interface. The observation supports the formation of organometallic precipitates that contain a high concentration of Co and Cr, as discussed by Radice et al. [48]

The early-stage aqueous corrosion of a CoCrMo alloy in Cl^- solutions indicated that the oxide also has a rocksalt structure, as shown in Figure 4.5. This result compares well to the oxides found in the CoCrMo corroded in the model synovial fluids containing HA. This is not surprising as an analysis of the base electrolyte solution indicates that there is about around 0.11 M of Cl^- , which is a similar concentration to the electrolyte used for aqueous corrosion albeit with different pHs. However, Radice et al. [48] has also shown that the local pH near the alloy surface drops during the electrochemical tests, supporting that oxides formed on CoCrMo alloys corroding in the model synovial fluids in this chapter can be modelled with the aqueous corrosion in a simple Cl^- -containing solution. Although the oxide structures of the two cases are similar, the chemical compositions have very different results. In Figure 4.6, the rocksalt oxide layer contains a significant amount of Cr, indicating that nonequilibrium

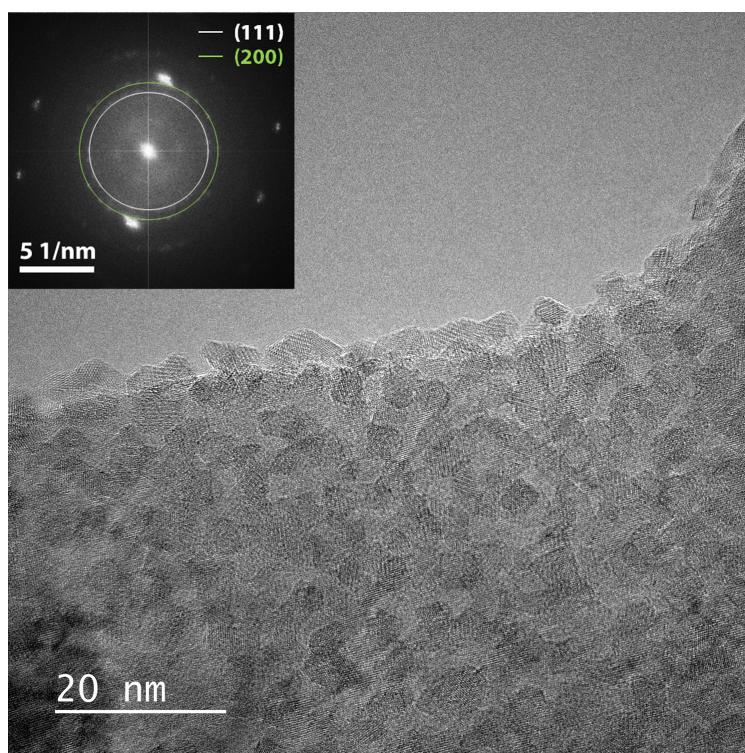


Figure 4.3. TEM analysis of the oxide layers in the RPMI + HA sample shows that the oxide islands are polycrystalline and have rocksalt crystallography.

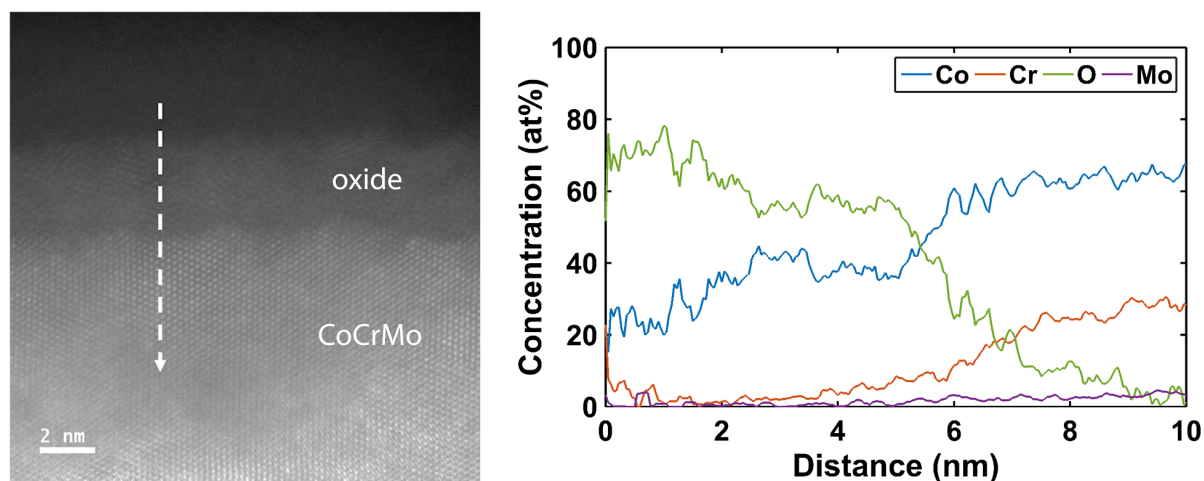


Figure 4.4. HAADF imaging and a corresponding EDS linescan verified that the thin rocksalt oxide contains almost no Cr, with the exception of minor Cr content near the metal-oxide interface.

solute capture has occurred during oxide formation. As the thermodynamic solubility of Cr in rocksalt CoO is about ~ 1 at.% [159], the rocksalt oxide shown in Figure 4.6 is metastable.

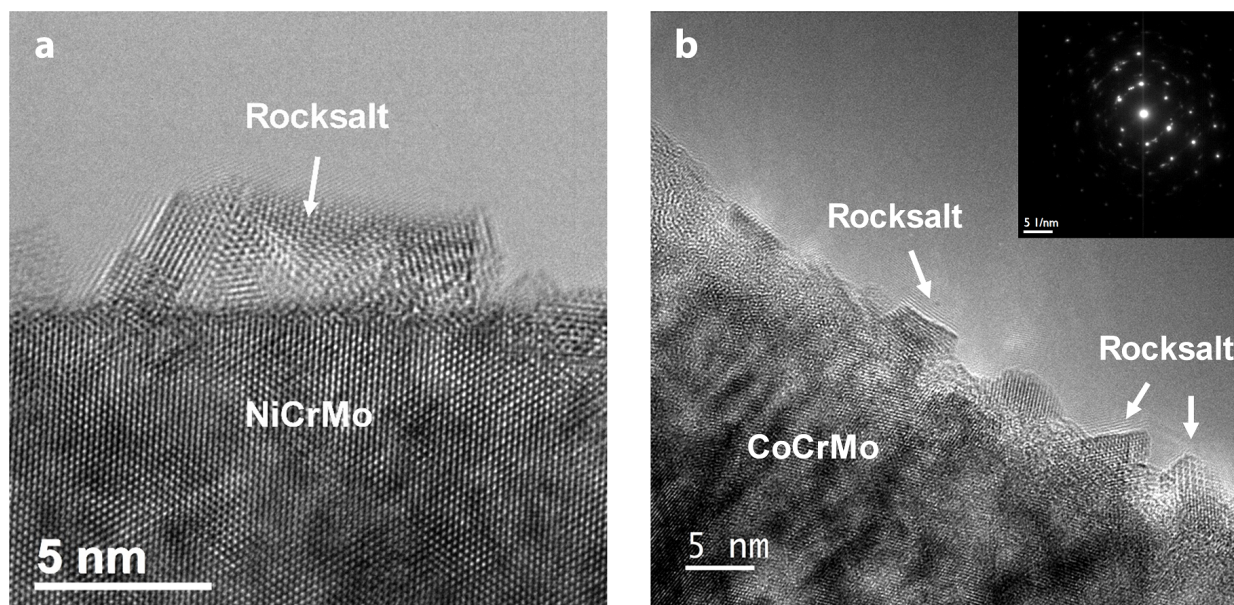


Figure 4.5. (a) The early-stage aqueous corrosion of a NiCrMo alloy show rock-salt oxides forming epitaxially on the metal. Adapted from [160] (b) Similarly, a CoCrMo alloy corroded in Cl^- -containing solutions has mostly rock-salt oxide islands.

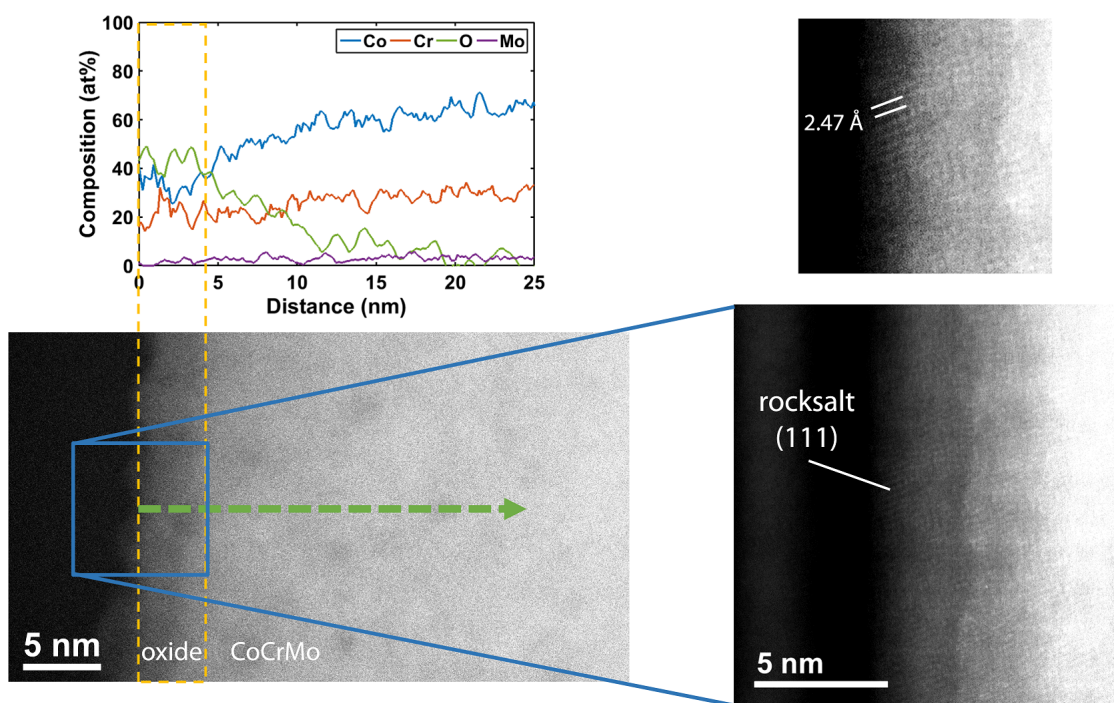


Figure 4.6. The EDS linescan of the oxide layer formed during aqueous corrosion indicated that the oxide composition contains a significant amount of Cr, confirming that nonequilibrium solute capture occurred during oxide formation.

4.4 Work in Progress

Since the cations can form organometallic compounds with HA and albumin proteins, Cr depletion in the oxides can be accounted for. However, HA has been shown to reduce the corrosion resistance of the alloy in the literature, so a current collaboration is underway to clarify the role of HA in CoCrMo corrosion in simulated synovial fluids. To isolate the effect of HA and avoid the formation of organometallic compounds, an electrolyte solution that consists of only Dulbecco's phosphate buffered saline (DPBS) and HA was tested. The electrochemical protocol is also modified accordingly to include potentiodynamic polarization, which is used to characterize the alloy behavior in this electrolyte, and potentiostatic anodic polarization at +0.7 V, which is used to observe the corrosion current in the transpassive domain. As shown in Figure 4.7, the CoCrMo alloy immersed in DPBS + HA has a transition to the transpassive domain at around +0.6 V. For the other two electrolyte solutions, which are DPBS and DPBS + NCS + HA, the alloy remains in the passive domain throughout the potentiodynamic scan. This is further supported by the potentiostatic polarization, which shows that the current continues to increase in the DPBS + HA solution, while there is practically no current with the other two solutions, as seen in Figure 4.8. This suggests that the alloy remains in the passive state in those cases.

The electrochemical measurements indicate that the solutions containing HA fared much worse compared to solutions containing DPBS only. Furthermore, the addition of proteins significantly improved the corrosion resistance, suggesting that proteins can compensate for the preferential interaction between HA and Cr and prevent the dissolution of the protective oxide layer. Since phosphate ions and proteins are known to contribute to the electrochemical behavior of CoCrMo even in small concentrations, characterization of the oxide film is necessary to elucidate the effects of each electrolyte component on alloy passivation. Preliminary TEM observations of the oxide layers in a CoCrMo sample immersed in DPBS + HA indicate that the oxide is porous and has mainly rocksalt crystallography, as seen in Figure 4.9. Additional TEM studies can elucidate the oxides on the samples tested without HA and

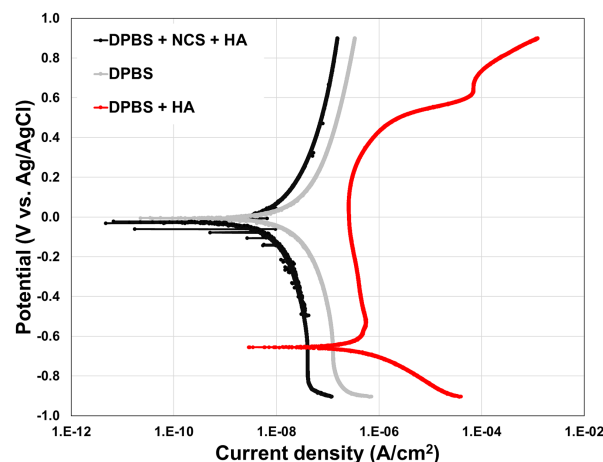


Figure 4.7. Potentiodynamic scans from -0.9 V to 0.9 V (vs. Ag/AgCl) on CoCrMo alloy samples immersed in three different model synovial fluids containing different combinations of Dulbecco's phosphate buffered saline (DPBS), newborn calf serum (BCS) protein, and HA. Without proteins, the presence of HA significantly decreases the corrosion resistance of CoCrMo. Adapted from [161].

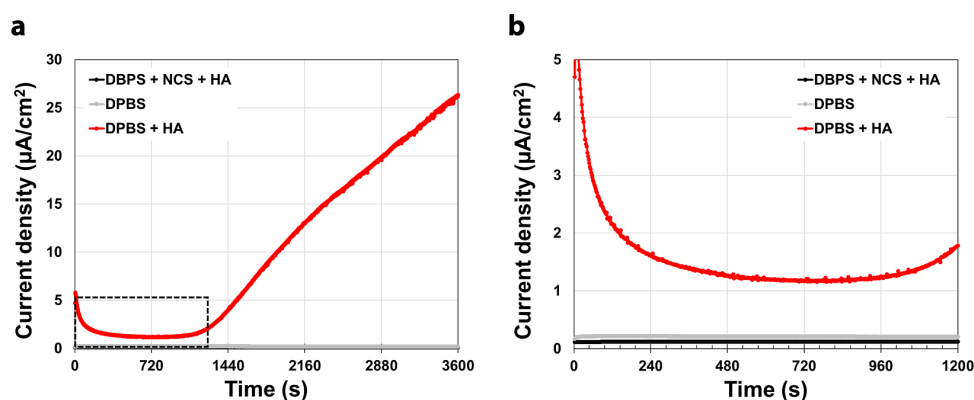


Figure 4.8. (a) Potentiostatic anodic polarization at +0.7 V (vs. Ag/AgCl) for 1 hour indicates that current increases significantly in the DPBS + HA solution, while there is practically no current in the other solutions, suggesting that the alloy remains in the passive state in those cases. (b) The dotted area in (a) is magnified to show the respective current densities in the DPBS and DPBS + NCS + HA solutions.

with additional proteins in order to determine the whether the oxides in those cases form a complete Cr_2O_3 passive layer. These results will provide additional insights into how HA modifies passive oxide layer and the role it plays in tribocorrosive conditions. These results will be left for a future publication.

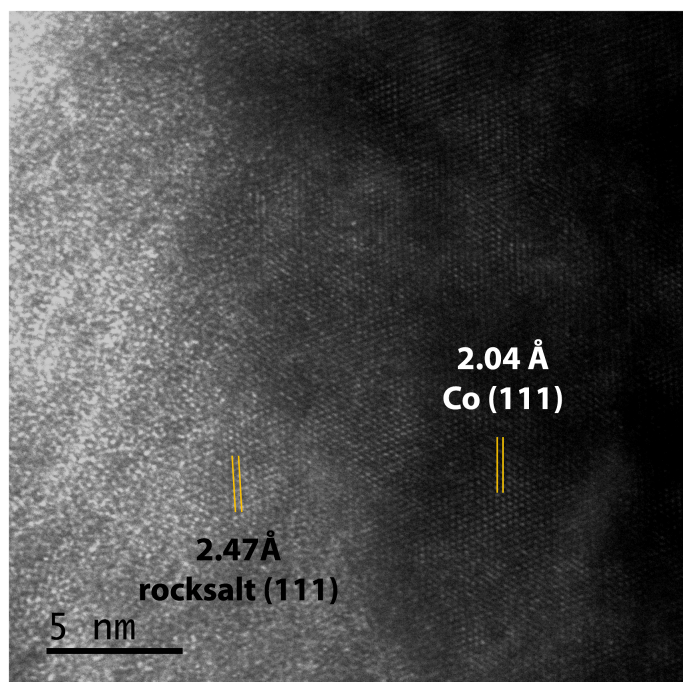


Figure 4.9. TEM reveals that the oxide formed on a CoCrMo sample immersed in DPBS + HA is porous and has mainly rocksalt crystallography.

4.5 Conclusions

The crystallography and chemistry of oxides formed during the corrosion of a CoCrMo alloy in simulated synovial fluids containing albumin proteins and hyaluronic acid were studied by nanoscale characterization. High-resolution TEM and EDS compositional linescans enabled the characterization and comparison of oxide films formed during corrosion in biological fluids and in a Cl^- -containing electrolyte. The results of this chapter indicated that the presence of hyaluronic acid alter the reactions involved in the growth of a protective oxide film, confirming previous electrochemical results for electrolytes containing hyaluronic acid that showed lower corrosion resistance and higher anodic currents. Although the oxides formed during corrosion in model synovial fluids and the Cl^- electrolyte both have rocksalt crystallography, the oxides on the CoCrMo alloys corroded in model synovial fluids do not contain solute capture, suggesting a secondary mechanism is dominant. Hyaluronic acid can form complexes during anodization in the presence of albumin proteins, resulting in Cr depletion and non-protective oxide islands on the alloy surface. Preliminary results from

a separate electrochemical study without albumin proteins confirmed that hyaluronic acid forms metal complexes with Cr and inhibits the formation of passive oxide films, resulting in significantly reduced corrosion resistance of the CoCrMo alloy. Based on these results, it is important to establish not only the electrochemical behavior of CoCrMo alloys in simulated synovial fluids that contain hyaluronic acid, but also the morphology and chemistry of the passive oxide layer in the presence of hyaluronic acid molecules to fully elucidate the role of hyaluronic acid in the dissolution of CoCrMo alloys.

Thermodynamics of the Formation of Nonstoichiometric Spinel Oxides

When an alloy is undergoing oxidation and corrosion, a number of oxide phases with varying chemical compositions can form. In the classic Wagner theory, cations, anions, and ionic defects are assumed to be in local equilibrium at interfaces and throughout the bulk oxide, with a quasi steady-state diffusion of charged species across the oxide that drives the metal oxidation [162]. It is commonly assumed that the most thermodynamically stable oxide phases indicated in phase diagrams [163, 164] or Pourbaix diagrams [22] will form. This assumption generally holds for slow-growing and thick oxide films; however, it has been shown that a metastable oxide [165–168] or hydroxide [160, 169] can form in early-stage oxidation or corrosion when the film is very thin, resulting in a departure from local equilibrium conditions. Nonequilibrium solute capture (see Chapter 3), which is a phenomenon where metastable oxides have unusual combinations of crystal structures and chemical compositions that deviate from thermodynamic limits, has been extensively studied experimentally in multiple Cr-containing alloy systems [40, 41, 108, 109]. For CoCrMo alloys, I have shown that defective corundum and spinel oxide phases can form during early-stage oxidation. In all observed cases of solute capture, there are either rapidly moving interfaces or a large net flux across a static interface, indicating that a kinetic condition is required in addition to a thermodynamic condition for solute capture to occur. While the kinetic condition is the critical parameter, a thermodynamic assessment of nonstoichiometric oxide phases can determine whether such phases can be in a metastable state and elucidate whether solute capture can occur [123].

This chapter will focus on the thermodynamic conditions for solute capture in Ni-Cr spinel oxides, which are commonly observed in high-temperature oxidation of Ni-Cr alloys [162, 166, 170–173], with DFT calculations to determine whether nonstoichiometric spinels can be

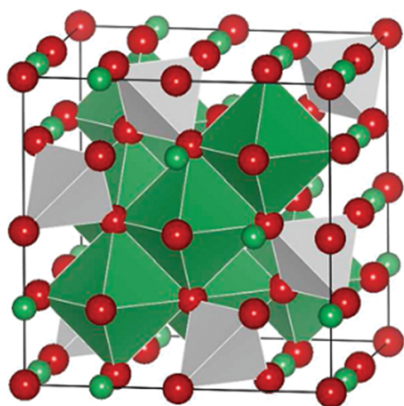
formed. The structure of this chapter is as follows. First, I will review the general background of the spinel oxides, their relevance in oxidation applications, and the thermodynamics and kinetics of forming them. Next, I will describe some of the complexities of the electronic and magnetic structures of spinels and how they are treated in the DFT calculations. Following that, I will demonstrate that the stoichiometry of the Ni-Cr spinel oxide can extend beyond the thermodynamically stable NiCr_2O_4 , as DFT calculated formation energies of the non-stoichiometric spinels are compared to calculated energies of rocksalt and corundum phases. The DFT results are mapped onto a plot that shows the formation energy versus the metal cation composition, and the convex hull, which connects the lowest energy structures, can be used to compare the relative thermodynamic stability of each calculated oxide phase. Lastly, a few possible experiments to validate whether nonstoichiometric Ni-Cr spinel oxides can form will be discussed at the end of the chapter.

5.1 Background on Spinel Oxides

Spinel oxides are commonly obtained in oxidation experiments of binary and multi-component alloys and can act as a protective scale in addition to corundum oxide. Recent studies have attempted to use a spinel-based coating to protect alloys from oxidation [174, 175]. Spinel has a cubic crystal structure ($\text{Fd}\bar{3}\text{m}$, space group 227) and the conventional unit cell consists of 8 face-centered cubic (fcc) cells with the oxygen anions occupying the fcc lattice points. Of the available tetrahedral sites (interstitial sites formed by 4 oxygen anions) and octahedral sites (interstitial formed by 6 oxygen anions) in the unit cell, there are 8 tetrahedral sites and 16 octahedral sites that are occupied by the cations. In a normal spinel oxide structure, divalent A cations occupy the tetrahedral sites and trivalent B cations occupy the octahedral sites, confirming that the stoichiometry of a normal spinel is AB_2O_4 . However, there is also the inverse spinel structure, in which half of the trivalent B cations occupy the tetrahedral sites and the other half of B with all the divalent A cations occupy the octahedral sites [176]. The normal spinel and inverse spinel structures are shown in Figure

5.1 Correspondingly, the inverse spinels will have slightly different stoichiometries as they are typically written as B_2AO_4 or $B[AB]O_4$ to denote which cations occupy which sites. I will return to the electronic structures of spinels later in the chapter.

Normal spinel structure



Inverse spinel structure

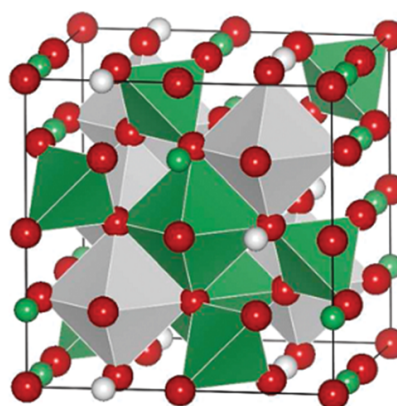


Figure 5.1. Crystal structures of a normal spinel and a inverse spinel. A atoms are in gray, B atoms are in green, and oxygen atoms are in red. Adapted from [177].

Spinel oxides are commonly observed in high-temperature oxidation of Ni-Cr and Co-Cr alloys [101, 103, 104, 162, 166, 170–173, 178], although they can also exist in early-stage oxidation at intermediate temperatures [179]. It has been shown the chromite spinels such as $NiCr_2O_4$ and $CoCr_2O_4$ have lower cation diffusivities compared to Cr_2O_3 ; however, the published diffusion coefficients can be somewhat unreliable as the measurements can differ by orders of magnitude [112]. Additionally, the protective nature of spinel oxides can also be questionable due to their porosity, which can be significant if the spinel oxide was formed rapidly [101, 180]. Solid-state reaction experiments between single crystal NiO and CoO with Cr_2O_3 powder have revealed differences in the formation of $NiCr_2O_4$ and $CoCr_2O_4$. In the case of $NiCr_2O_4$, it has been showed that the receding surface of the NiO is morphologically stable. On the contrary, the CoO receding surface is morphologically unstable during the formation of $CoCr_2O_4$, suggesting that the Co cation diffusion across the spinel oxide is significantly more rapid [113]. Other studies, which used inert diffusion markers, have confirmed that $NiCr_2O_4$

forms via the counterdiffusion of Ni and Cr cations through the spinel (originally proposed by Wagner [181]), while demonstrating that CoCr_2O_4 forms via the unidirectional diffusion of Co cations and O anions through the spinel [182, 183]. Diffusion marker experiments have also shown that the mechanism for NiCr_2O_4 and CoCr_2O_4 formation can differ greatly depending on the porosity of the reacting oxide phases [112]. For instance, the rate of NiCr_2O_4 formation from dense, crack-free NiO and Cr_2O_3 phases are orders of magnitude smaller than when the reaction is carried out with porous oxides, as the mechanism is controlled by vapor-phase transport of oxygen through the pores. However, as the early-stage oxides formed in oxidation reactions can be porous, this suggests that the kinetic condition for nonequilibrium solute capture is often met as rapid diffusion can lead to the formation of nonstoichiometric spinels.

Lastly, I will turn to the thermodynamic conditions for forming chromite spinels. There is a large amount of thermodynamic assessments of the enthalpy of formation of chromite spinels based on high-temperature equilibrium data [184–188]; however, these values tend to have a large scatter for NiCr_2O_4 , with the standard enthalpy of formation (ΔH_f°) values deviating by 50-70 kJ/mol ($\sim \pm 5\%$) [189]. This disparity is largely unexplained and often attributed to different measurement methods, which typically use electromotive force (e.m.f.) measurements with a solid-oxide electrolyte or equilibrium constant measurements at high temperatures to determine the activities of oxides [190, 191]. Furthermore, thermodynamic modelling for spinel has often been difficult owing to the nonstoichiometric nature of spinel oxides. For instance, the phase diagram for the $\text{CoO-Cr}_2\text{O}_3$ system indicates that a nonstoichiometric spinel phase $(\text{Co}_{1-x}\text{Cr}_x)_3\text{O}_4$ is thermodynamically stable for $x \leq 2/3$ [159]. Although NiCr_2O_4 is known thermodynamically as a line compound (fixed stoichiometry) [190, 191], I am interested in examining if nonstoichiometric Ni-Cr spinel oxides can be metastable. Given that the kinetic conditions for solute capture is probably met, the thermodynamic condition can determine whether solute capture is possible in Ni-Cr spinels.

5.2 DFT Methods

DFT allows for the calculations of the structure, thermodynamic stability, and electronic properties of nonstoichiometric spinel oxides that do not have any existing experimental data. However, the electronic and magnetic structures of spinels need to be considered in order to compute their formation energies with appropriate accuracy. As introduced in the beginning of the chapter, inverse spinel oxides can further introduce complexities to the electronic structures of these oxides. Additionally, a spinel can also have a defective structure, where the divalent or trivalent cations randomly occupy the tetrahedral and octahedral sites. Since certain cations have distinct preferences for tetrahedral or octahedral sites, the crystal field stabilization energy (CFSE) of each cation can be used to determine the preferred cation distribution across the interstitial sites. As NiCr_2O_4 contains transition metals with $3d$ electrons, the Ni and Cr both prefer to be in high-spin states, as O^{2-} is a rather weak-field ligand. However, chromite spinels are typically normal spinels as Cr^{3+} has a much stronger preference for the octahedral site than Ni^{2+} does, so it is more energetically favorable for Cr^{3+} to occupy the octahedral sites. In reality, it has been shown that numerous valence states can exist in oxidation and corrosion [40] and sometimes cations can oxidize one another [123], so I will assume the DFT calculations will find the most energetically favorable structure.

Magnetism in spinel oxides also cannot be neglected. Depending on the cation distributions of the spinels, they can be ferromagnetic, antiferromagnetic, or even ferrimagnetic in the case of inverse spinels. For NiCr_2O_4 , which is an antiferromagnetic normal spinel, the number of spins in the Ni^{2+} high-spin states and the number of spins in the Cr^{3+} high-spin states are equivalent. While there are several previous DFT results for NiCr_2O_4 , it is unclear whether a complete search over spin states was performed, so incorrect conclusions may be reached as certain spin states are only the local minima. Based upon a search shown in a recent study [123], the antiferromagnetic unit cell belongs to the space group $\text{Imm}2$, with DFT lattice parameters of $6.03 \times 6.03 \times 8.53 \text{ \AA}$.

DFT calculations in this chapter were performed with the all-electron augmented plane wave + local orbitals (APW+lo) WIEN2K code [83, 84] for spinel structures of varying Ni and Cr compositions. The spin-polarized calculations used the PBE functional exchange-correlation potential [85], a hybrid fraction of 0.25 for the 3d electrons using the on-site hybrid approach [80–82], a RKmax of 6.5 and a k-point mesh of $5 \times 5 \times 5$, with atomic positions and densities converged with a parallel fixed-point algorithm [86]. All structures were fully relaxed, and the lattice parameters were optimized as a function of the volume while maintaining the same space group. As a secondary check, the treatment of transition metal oxides was compared to experimental thermodynamic data such as the heats of formation for NiO and Cr₂O₃, and the difference is smaller than the intrinsic errors in typical DFT calculations.

The bond-valence sums (BVS) of the ions in the unit cell were analyzed in addition to the formation energies, optimized structures, and density of states, bond-valence sums (BVS) were analyzed. BVS provides a simple way to characterize the structural stability with respect to the coordination and bonding for atoms in an ionic compound [87–89]. The BVS can also be used to interpret the valence of the metal ions in these oxides, which can be complex as many transition metals are multivalent and can exhibit multiple valences in a single compound during oxidation and corrosion.

5.3 Results and Discussion

For all structures ranging from pure Ni spinel (Ni₃O₄) to pure Cr spinel (Cr₃O₄), the Ni and Cr cations are in the high-spin states, suggesting that the most thermodynamically stable structures were found for each composition. The CIFs for the DFT relaxed structures for each composition are listed in the Appendix. As shown previously [123], the DFT calculated formation energy for NiCr₂O₄ is compared to the existing thermodynamic data with good agreement, with the DFT values only about 10 kJ/mol higher. The free entropy of mixing in NiO and Cr₂O₃ reactants was also considered, but since this value is only a few kJ/mol it is neglected in this assessment. Full values of the energies at both STP and 1000 K with 1

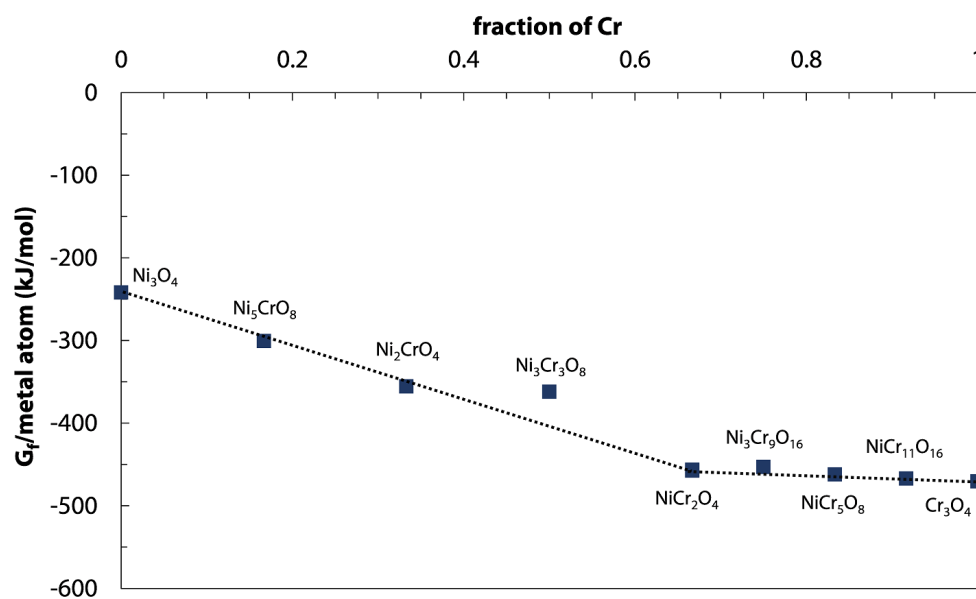
atm of oxygen are summarized in Table 5.1 and shown in Figures 5.2 and 5.3. All calculated structures, with the exception of $\text{Ni}_3\text{Cr}_3\text{O}_8$, lie near the convex hull constrained to the spinel structure.

The results are compared to previous DFT calculations of nonstoichiometric oxides that can exist in oxidation and corrosion contexts [123], shown in Figure 5.4. Specifically, these four cases are considered for this assessment:

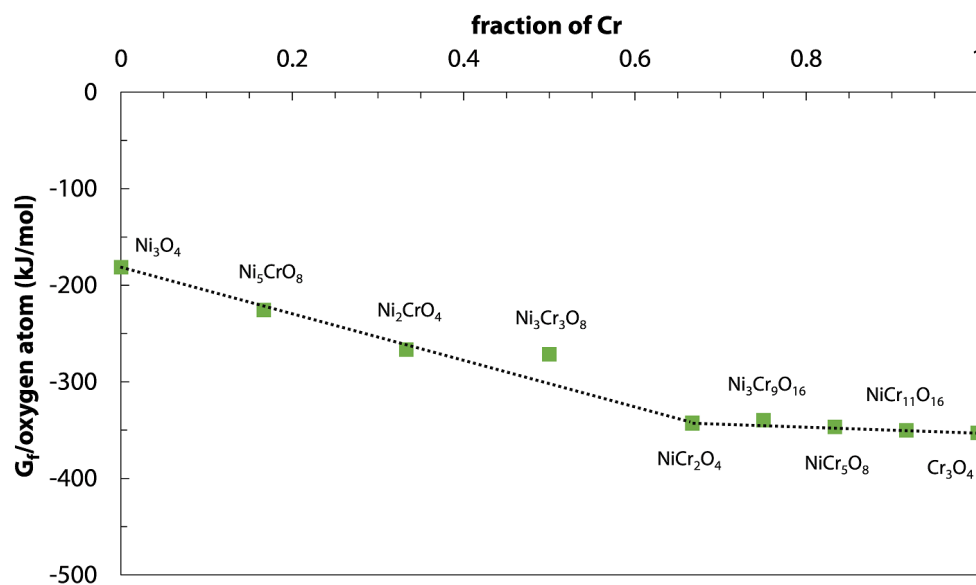
- (1) Ni^{2+} and Cr^{3+} in the rocksalt structure with half a Ni^{2+} vacancy per Cr^{3+} to preserve valence neutrality;
- (2) Ni^{2+} and Cr^{3+} in the corundum structure with 1.5 Ni^{2+} per Cr^{3+} removed to preserve valence neutrality;
- (3) Ni^{2+} and Cr^{3+} in the corundum structure with site substitution;
- (4) Ni^{2+} and Cr^{3+} in the rocksalt structure with site substitution.

Sherman et al. suggested that there are metastable compositions across the entire compositional range of Ni and Cr concentrations for both rocksalt and corundum crystallographies [123]. To expand on that conclusion, spinels can also form metastable structures across the entire compositional range too, as all of the calculate structures have energies that are significantly lower than that of the alloy composition. The energies are normalized by metal atoms and oxygen atoms to demonstrate the dominant diffusing species for each case. For the limit that cation vacancy diffusion is dominant, and the metal-oxide interface is static, growth is occurring at the outer surface and the thermodynamic driving force is the energy change per metal atom. On the other hand, when anion diffusion is dominant and the outer oxide surface is static, growth is occurring at the metal-oxide interface and the thermodynamic driving force is the energy change per oxygen atom.

By direct comparison, the convex-hull for the energy of formation normalized by metal atoms (G_f/M) across all crystallographies, shown in Figure 5.4, follows a different shape than the constrained convex-hull shown in Figure 5.3a for the same conditions. The

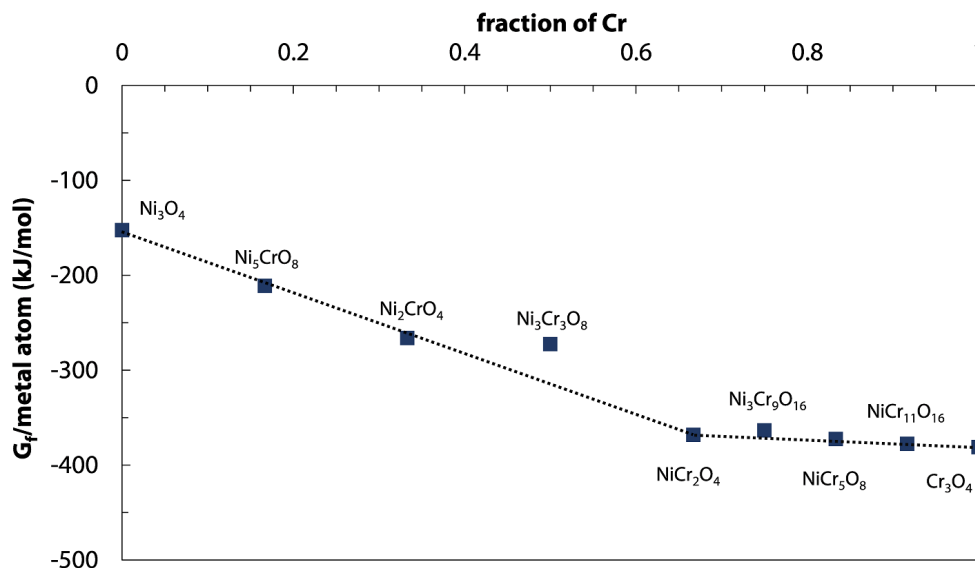


(a)

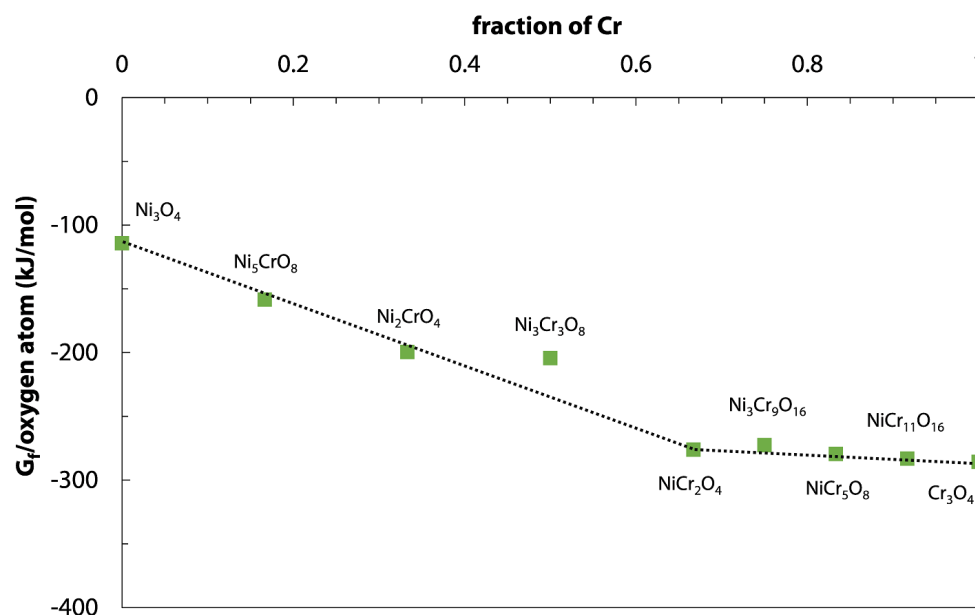


(b)

Figure 5.2. Plots of the free energy of formation of different spinel oxides with varying amounts of Ni and Cr at STP. Individual points indicate the DFT energies shown in Table 5.1 and the dotted line represents in the convex hull constrained to the spinel structure. The energies shown are (a) normalized per metal atom and (b) normalized per oxygen atom, in order to demonstrate the dominant diffusing species for each case.



(a)



(b)

Figure 5.3. Plots of the free energy of formation of different spinel oxides with varying amounts of Ni and Cr at 1000 K and 1 atm of oxygen. Individual points indicate the DFT energies shown in Table 5.1 and the dotted line represents in the convex hull constrained to the spinel structure. The energies shown are (a) normalized per metal atom and (b) normalized per oxygen atom, in order to demonstrate the dominant diffusing species for each case.

Table 5.1. DFT energies normalized by metal atoms and oxygen atoms are shown for each spinel oxide at STP and 1000 K.

Compound	Cr fraction	G_f/M (STP)	G_f/O (STP)	G_f/M (1000 K)	G_f/O (1000 K)
Ni_3O_4	0.000	-241.8	-181.3	-152.3	-114.2
Ni_5CrO_8	0.167	-300.7	-225.5	-211.2	-158.4
Ni_2CrO_4	0.333	-355.5	-266.6	-266.0	-199.5
$\text{Ni}_3\text{Cr}_3\text{O}_8$	0.500	-361.9	-271.4	-272.4	-204.3
NiCr_2O_4	0.667	-457.6	-339.6	-363.4	-272.5
$\text{Ni}_3\text{Cr}_9\text{O}_{16}$	0.750	-452.9	-343.2	-368.1	-276.1
NiCr_5O_8	0.833	-462.1	-346.6	-372.6	-279.4
$\text{NiCr}_{11}\text{O}_{16}$	0.917	-467.1	-350.3	-377.6	-283.2
Cr_3O_4	1.000	-470.4	-352.8	-380.9	-285.7

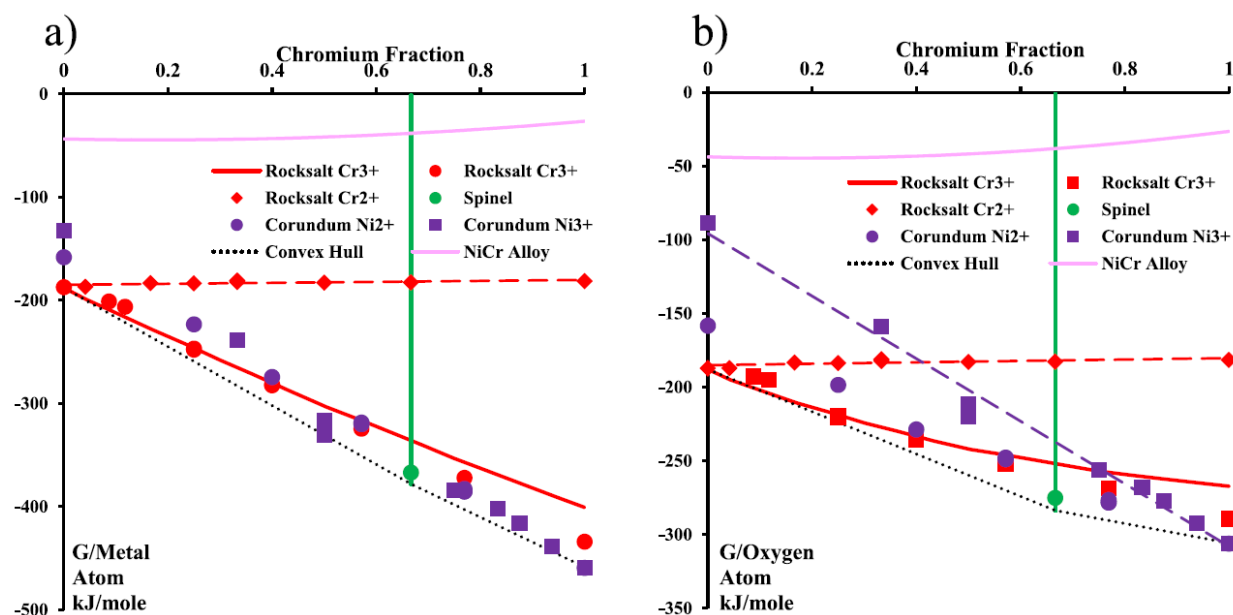


Figure 5.4. The free energies of various crystallographic phases with varying amounts of Ni and Cr at 1000 K and 1 atm of oxygen. Individual points indicate the DFT energies and the dotted line represents in the convex hull. The energies shown are (a) normalized per metal atom and (b) normalized per oxygen atom, in order to demonstrate the dominant diffusing species for each case. Adapted from [123].

Ni-rich side of the thermodynamically stable NiCr_2O_4 follows a similar trajectory, but the Cr-rich side plateaus and has a much flatter slope for the energies normalized by metal atoms. This suggests that when cation diffusion is the dominant in the oxide growth, the nonstoichiometric spinels rich in Ni are energetically more favorable than structures that are

rich in Cr. It is possible that nonstoichiometric spinels can be slightly richer in Cr; however, as the Cr fraction exceeds 0.66 the Cr-rich corundum phase dominates, up to Cr_2O_3 which is about 80 kJ/mol per metal atom lower in energy than Cr_3O_4 . The comparison between the oxygen diffusion case is slightly different. Both energy of formation normalized by oxygen atoms (G_f/O) convex-hulls in Figures 5.3b and 5.4 have a change in slope at 0.66 Cr fraction (NiCr_2O_4); however, since the spinel end members are higher in energy compared to their rocksalt and corundum counterparts, it is unlikely for a nonstoichiometric spinel to form in the high Ni or high Cr regimes when oxygen diffusion is dominant. In fact, the entire Ni-rich side of the thermodynamically stable NiCr_2O_4 is dominated by rocksalt structures with Ni^{2+} and Cr^{3+} , as their energies are 30-70 kJ/mol per oxygen atom lower than the spinels across those compositions. When the Cr fraction exceeds NiCr_2O_4 , the nonstoichiometric spinel structures are thermodynamically favorable up until when the Cr fractions reaches around 0.9. This suggests that if oxygen diffusion was dominant, the most of the nonstoichiometric spinel compositions that are rich in Cr are metastable and can possibly be observed.

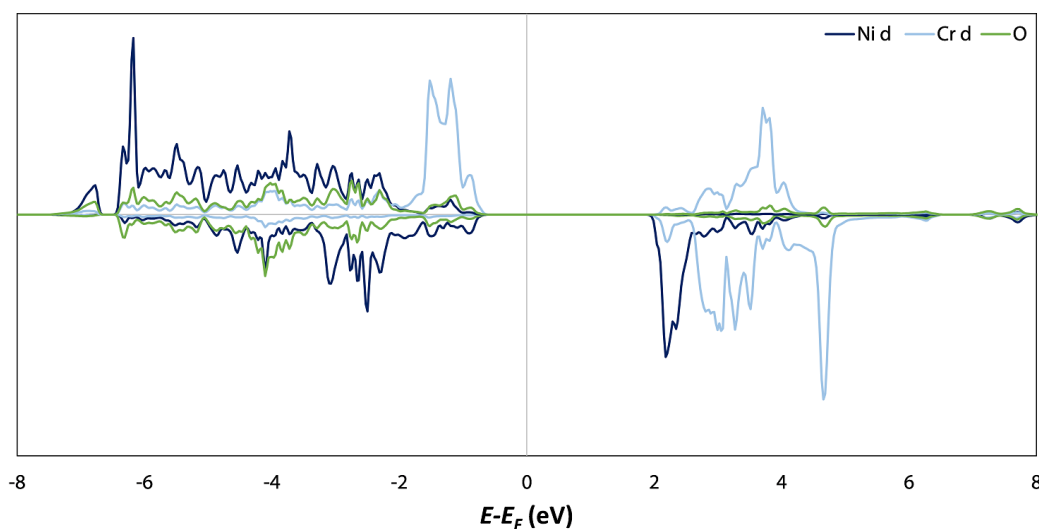


Figure 5.5. Density of states for NiCr_2O_4 , showing the Ni and Cr $3d$ states and the O $2p$ states. Up spins are above the x axis and down spins are below.

As a final confirmation that these structures are well-ordered, their densities of states and BVS are analyzed. Only the end members in the constrained convex hull and the

stoichiometric spinel NiCr_2O_4 (Figure 5.5) were considered in this analysis, as the rest of the structures are expected to behave similarly to one of the three cases (insulator, semiconductor, or metallic). For the Ni_3O_4 structure, the density of states indicate that it is metallic, as shown in Figure 5.6. BVS analysis for Ni_3O_4 suggests that Ni^{3+} can oxidize Cr^{3+} to Cr^{4+} to reduce the energy of the system, as Ni^{3+} is thermodynamically unfavorable. As there is no Cr in Ni_3O_4 to lower the energy of the structure, the Ni^{2+} cations are all oxidized to varying degrees as shown in the BVS values for Ni_3O_4 in Table 5.2. In addition it has also been shown previously that Ni can act as p-type dopant in spinel oxides [192], so a large quantity of Ni would result in metallic behavior. The density of states of Cr_3O_4 , shown in Figure 5.7, correspond to a classic semiconductor with a band gap of 1.5 eV, with the valence band defined primarily by Cr^{2+} states and the conduction band defined by Cr^{3+} states. As Cr^{3+} strongly prefers the octahedral interstitial sites in the spinel structure, the tetrahedral sites are occupied by Cr^{2+} as verified by BVS values for Cr_3O_4 in Table 5.2.

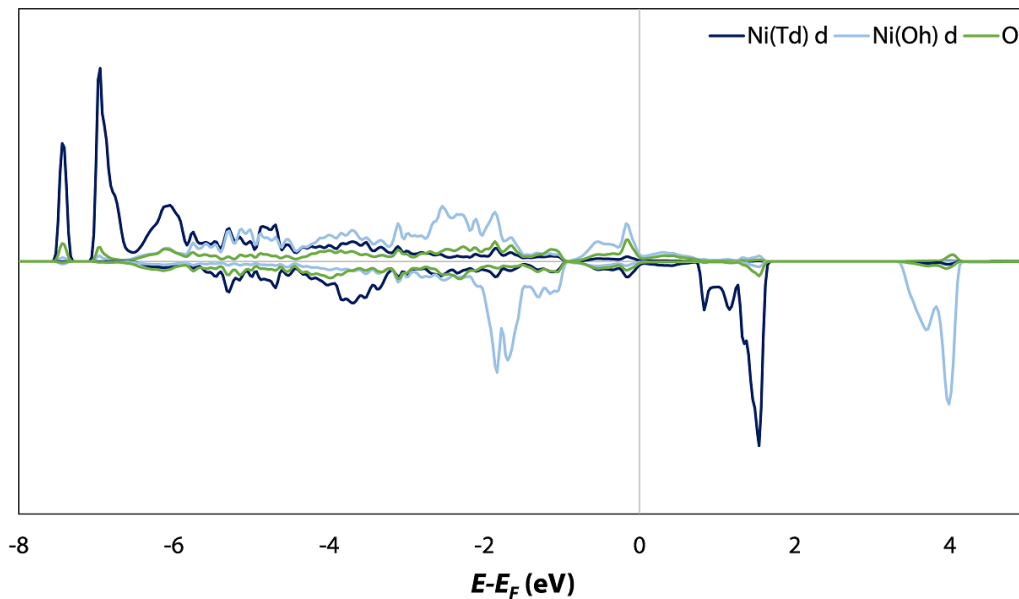


Figure 5.6. Density of states for Ni_3O_4 , showing the Ni 3d states and the O 2p states. Up spins are above the x axis and down spins are below.

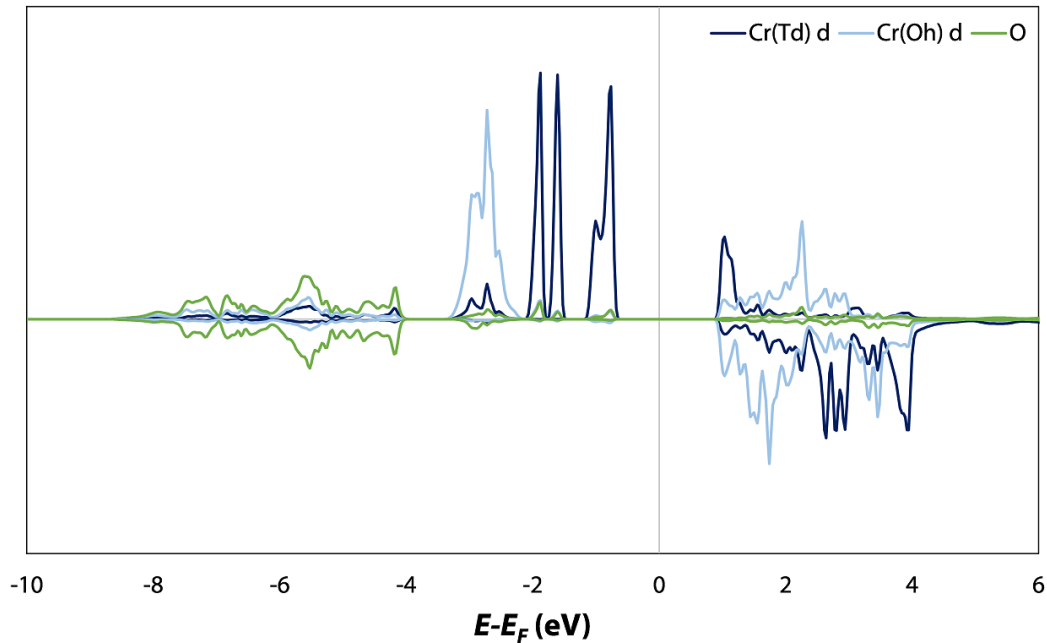


Figure 5.7. Density of states for Cr_3O_4 , showing the Cr 3d states and the O 2p states. Up spins are above the x axis and down spins are below.

Table 5.2. BVS for Ni, Cr, and O ions in NiCr_2O_4 , Ni_3O_4 , and Cr_3O_4 . Td denotes tetrahedral sites and Oh denotes octahedral sites.

NiCr_2O_4		Ni_3O_4		Cr_3O_4	
ion	BVS	ion	BVS	ion	BVS
Ni1 (Td)	1.74	Ni1 (Td)	2.30	Cr1 (Td)	1.81
Ni2 (Td)	1.74	Ni2 (Td)	2.30	Cr2 (Td)	1.81
Cr1 (Oh)	2.94	Ni3 (Oh)	2.48	Cr3 (Oh)	2.80
Cr2 (Oh)	2.94	Ni4 (Oh)	2.48	Cr4 (Oh)	2.80
O1	1.89	O1	1.82	O1	1.88
O2	1.92	O2	1.82	O2	1.82
O3	1.92	O3	1.82	O3	1.83
O4	1.89	O4	1.81	O4	1.88

5.4 Discussion and Conclusions

The results indicate that there is a wide range of metastable compositions across the spinel oxide crystallography. For the cases where cation diffusion is dominant, spinel structures with a Cr fraction of 0.66 or less are likely to form, as some of them are in fact the lowest energy structure for the given cation composition. For the cases where oxygen diffusion is dominant, nonstoichiometric spinel structures that have Cr fractions that exceed 0.66

are thermodynamically favorable up until when the Cr fractions reaches around 0.9. We note that this analysis only considered ordered low energy structures for each composition; however, mixed spinel structures, which are intermediate between normal and inverse spinels, and other disordered variants can exist. All the spinel structures considered in this chapter are significantly lower in free energy than the alloy across all compositions, suggesting that variable compositions outside the stoichiometric thermodynamic phases should be expected to be common in spinel oxides during high-temperature oxidation. This indicates that the thermodynamic conditions for nonequilibrium solute capture are satisfied for both cation and oxygen diffusion.

While the thermodynamic calculations of ordered nonstoichiometric spinels are useful to assess whether the spinel structures are likely to form, the kinetic conditions for nonequilibrium solute capture merit some discussion. In many kinetic studies of NiCr_2O_4 formation, the rate of formation can differ significantly based on the chemical purity and porosity of the reacting oxide phases [112]. Additional studies have also shown that rapid formation of NiCr_2O_4 can lead to high porosities, which allow the vapor-phase transport of oxygen through the pores [101, 180]. Since the initial oxides formed during high-temperature oxidation can be porous and contain solute capture, the rapid diffusion of cations and oxygen is expected. This suggests that it is likely for the kinetic conditions for nonequilibrium solute capture in Ni-Cr spinels to be met in most cases of oxidation at elevated temperatures. While there are some estimates that indicate the solute capture will occur for many cases of high-temperature oxidation and most cases of aqueous corrosion, detailed kinetic studies of nonstoichiometric spinels require additional work.

The densities of states analysis indicate that the spinels can range from insulators to semiconductors, or even metals depending on the composition. The stoichiometric NiCr_2O_4 is a well-ordered insulating oxide, which are typically associated with less frequent film breakdown from electrochemical studies of passivating oxides formed on Ni-Cr alloys. The doping of the stoichiometric NiCr_2O_4 spinel can have negative effects on the corrosion and

oxidation resistance of nonstoichiometric spinel oxides. As proposed by Cabrera and Mott [27], thin oxide films, formed during the initial stages of oxidation, can allow electrons to pass freely from the metal to the surface of the oxide to form negatively charged species. This results in an electric field within the oxide that provides a driving force for the transport of cations from the metal-oxide interface to the oxide surface to form additional layers of oxide. To extend the model to thicker films in the transient regime between beyond the Cabrera-Mott model, semiconducting or even metallic oxide films can maintain the transport of electrons to the oxide surface, affecting the early-stage oxidation resistance of the alloy. However, it is important to recognize that these semiconducting or metallic nonstoichiometric spinels are metastable and can evolve into more thermodynamically stable oxide phases in long-term oxidation.

Lastly, the evolution of nonstoichiometric Ni-Cr spinels over time also merits further work. For instance, it is important to understand the microstructure and oxidation resistance of oxide layers that evolve from nonstoichiometric spinels. For previous studies of spinel oxide formation, it has been shown that the cation diffusivity of NiCr_2O_4 are lower than that of Cr_2O_3 ; however, experimental observations indicate that NiCr_2O_4 is a less effective diffusion barrier owing to the formation of pores. Since the Ni-Cr spinels that contain solute capture are only predicted to exist in transient stages of oxidation, it is relevant to understand whether the nonstoichiometric spinels will promote or prevent the formation of dense protective oxides in long-term oxidation. This understanding will be important for predicting and controlling the long-term oxidation resistance of NiCr-based alloys.

In summary, a DFT thermodynamic assessment of the Ni-Cr spinel oxides indicate that there is a range of spinel structures with varying cation compositions that can form. The electronic structures of spinels can range from insulators to semiconductors, or even metals, and the valence states of the metal cations can vary based on the composition. Therefore, care is needed in the interpretation of valence results and the electronic properties of oxide layers based just upon spectroscopic information. Although these metastable oxides are predicted

to form in oxidative conditions, the compositions of the spinels are controlled by the kinetics of the formation of these structures. Given the interfacial velocities present in the formation of spinel structures, especially from porous defective reactant oxides, nonstoichiometric Ni-Cr spinels are likely to be observed experimentally. This provides additional opportunities to understand how these metastable spinels evolve over time and affect the long-term oxidation resistance of the base alloy, leading to critical insights into factors that can control and improve the oxidation resistance of NiCr-based alloys.

5.5 Future Work

Although there is some experimental evidence that suggest that Ni_3O_4 and Cr_3O_4 phases can exist [193, 194], a systematic validation of the various degrees of nonstoichiometry in Ni-Cr spinels and the conditions necessary for these phases to form is vital for understanding the mechanisms of nonequilibrium solute capture in spinels. Both of the experiments I propose in this chapter were scheduled to be completed in March 2020 but have been postponed indefinitely due to the coronavirus disease (COVID-19) pandemic impacting the United States [195].

The first experimental method I propose is alloy oxidation. Since we now have some knowledge about spinel formation in the context of oxidation, NiCr and NiCrMo alloys oxidized at moderate to high temperature for short periods of time may yield nonstoichiometric oxides. As detailed in a previous chapter, CoCrMo has been observed to form nonstoichiometric spinels due to its rapid formation kinetics. While the kinetic condition may not be as favorable, the porosity of the early-stage oxides formed on NiCr and NiCrMo alloys may allow for the kinetics to be rapid enough for solute capture to occur. In addition, there is evidence of nonstoichiometric spinels, albeit not Ni-Cr spinels, formed in a CoCrFeNi alloy when oxidized at 700 °C for only 30 min [109], suggesting similar temperatures and time scales can be applied to studying nonstoichiometric Ni-Cr spinels. Another oxidation study on a Ni-20Cr alloy confirmed with XRD that NiCr_2O_4 begins forming after 5 min of

oxidation at 600 °C [179]. I propose a systematic study of comparing spinel oxides formed on NiCr and NiCrMo at 600 °C and 700 °C for 10 min, 30 min, and 1 h. For the NiCrMo alloy, I also suggest attempting a high-temperature oxidation test at 1000 °C for 10 min, as NiCrMo is significantly more oxidation-resistant due to the promotion of corundum growth by Mo. The high temperature will allow the Cr_2O_3 and NiO phases to develop rapidly, possibly incorporating defects to accelerate the kinetics of spinel formation. As a final caveat, TEM characterization should occur as soon as possible after the oxidation exposure as the nonequilibrium oxides have been shown to age even at room temperature and nucleate the thermodynamically stable phases [40].

A second way of collecting experimental evidence of nonstoichiometric Ni-Cr spinels is by NiCr_2O_4 nanoparticle synthesis. A recent work [196] has shown that NiCr_2O_4 nanoparticles can be synthesized by mixing $\text{Cr}(\text{NO}_3)_3 \cdot 9\text{H}_2\text{O}$ and $\text{NiCl}_2 \cdot 6\text{H}_2\text{O}$ with a 2:1 molar ratio and precipitating out nanoparticles by adjusting the pH of the mixture to 12 with $\text{NH}_3 \cdot \text{H}_2\text{O}$. The precipitate powder exhibits spinel crystallography after annealing for 2 h at 1000 °C, while both corundum and spinel crystallographies are observed after annealing at 850 °C. I note that the XRD patterns shown by the authors of this study have rather broad peaks indicating a disordered spinel phase (Figure 5.8), so I anticipate that the spinel nanoparticles formed via this method will initially have nonequilibrium structures. I propose altering the molar ratio of the reactants in the initial mixture. By increasing the amount of $\text{NiCl}_2 \cdot 6\text{H}_2\text{O}$ or $\text{Cr}(\text{NO}_3)_3 \cdot 9\text{H}_2\text{O}$, a more Ni-rich or Cr-rich spinel can be synthesized. In addition, different annealing temperatures can be used to analyze the chemical composition of the spinels at various stages of growth. Since the nanoparticles that formed can be readily dispersed onto a TEM grid for characterization, the aging of the nanoparticles also can be avoided if there are in fact nonequilibrium solute capture in the spinels.

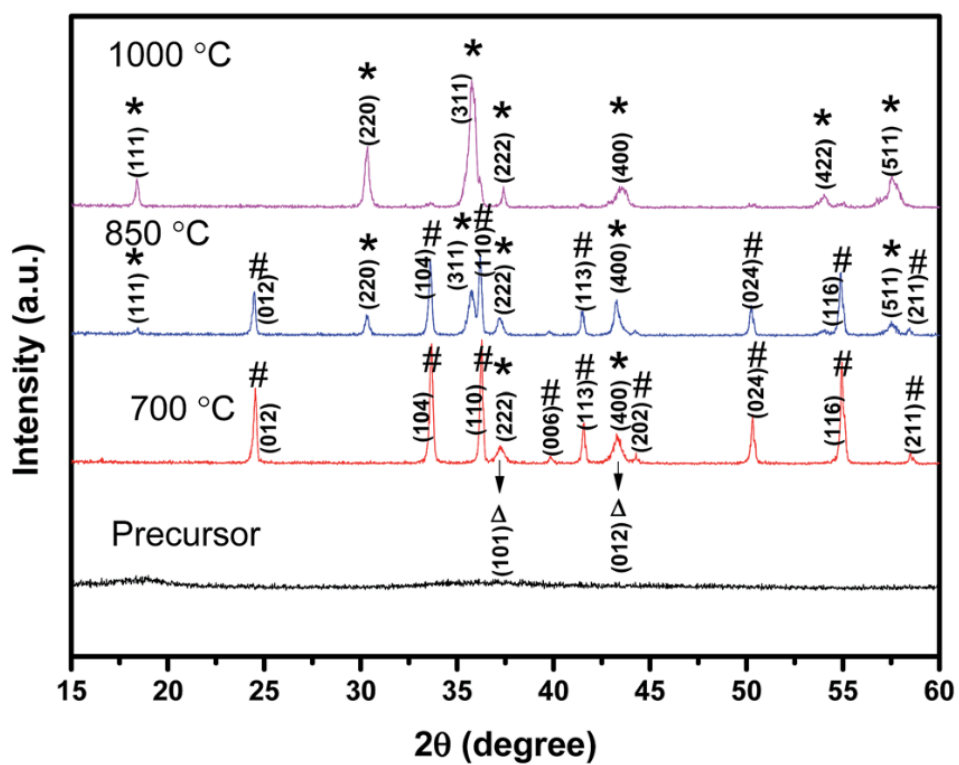


Figure 5.8. XRD patterns showing corundum (marked with #) and spinel (marked with *) crystallographies contain rather broad peaks indicating a disordered spinel phase has formed. Adapted from [196].

Early-Stage NiCrMo Oxidation Revealed by Cryo-TEM

As more exploratory work, a cryo-TEM approach has recently been implemented to understand early-stage aqueous corrosion in NiCrMo alloys. Many hydroxides that are formed at the surface of corroded alloys are unstable in an ambient environment and electron-beam sensitive, limiting the use of conventionally-prepared specimens for TEM characterization of these alloy-water interfaces. This experimental approach avoids sample dehydration by plunge freezing NiCrMo alloys corroded in a Cl^- -containing electrolyte. A cryo-FIB microscope was used to thin the sample to electron transparency, while preserving the air-sensitive alloy-water interface, and the sample was then cryo-transferred to a TEM for imaging and diffraction.

In this chapter, TEM results are presented that show the presence of rocksalt $\text{Ni}_{1-x}\text{Cr}_{2x/3}\text{O}$ and $\beta\text{-Ni}_{1-x}\text{Cr}_{2x/3}(\text{OH})_2$ phases in the corroded alloy. Additionally, their orientational relationship to the underlying alloy were revealed with electron diffraction and DF imaging, confirming the preservation of surface structure through the fully-cryogenic sample preparation and analysis. This opens many opportunities to study the passivation of alloys in aqueous electrolytes and characterize the growth of oxide and hydroxide films in various complex corrosion conditions such as in orthopedic implants. Lastly, this experimental approach can potentially provide additional insight into nonequilibrium solute capture and the valence states of the metal atoms in the hydroxide formed during aqueous corrosion. This work was performed collaboratively with Dr. Alexander Müller and Prof. Andrew Minor at the National Center of Electron Microscopy at Lawrence Berkeley National Laboratory and Dr. Xiao-xiang Yu at Northwestern University. The results and analysis presented in this chapter have been published in the journal *Ultramicroscopy* (see reference [160]).

6.1 Introduction

Nanoscale processes at solid-liquid interfaces play a critical role in many biological, chemical, and physical processes, ranging from fundamental phenomena such as crystal nucleation

and growth in solution and hydrogels to more complex ones such as electrochemical changes of metal/alloy surfaces during aqueous corrosion or the formation of solid-electrolyte interfaces (SEI) in batteries. The understanding of real-time nanoscale processes at these interfaces remains largely limited owing to the difficult nature of observing these phenomena *operando*. While *in situ* investigations of aqueous corrosion have been conducted with Raman spectroscopy [197–199], X-ray spectroscopy techniques [200–203], AFM [204–206], STM [207–210], and a surface force apparatus [211], these studies do not simultaneously acquire chemical and spatial information at sufficient resolutions to identify surface oxides and hydroxides or minor chemical changes at the metal-oxide interface. More recently, liquid cell TEM has been used for *in situ* TEM characterizations of electrochemical reactions such as lithiation [212–215], SEI formation [216–218], and aqueous corrosion [219, 220]. However, the high current density of the electron beam is extremely reducing [221] and can impact electrochemical processes. In consequence, electron beam effects have to be limited, resulting in a reduction of spatial resolution due to a reduced beam current. A recent appraisal [222] concluded that sub-nanometer spatial resolutions have not yet been achieved for *in situ* electrochemical experiments in the TEM.

Cryo-TEM avoids many of the problems described above and allows for the nanoscale characterization of the phases formed during early-stage aqueous corrosion by probing frozen, hydrated samples. Plunge freezing, a technique well-established for biological samples, is the process of rapidly freezing specimens in liquid ethane to prevent the transformation of water to the hexagonal ice phase and thereby preserve the near-native structure [223–226]. However, the specimens frozen with plunge freezing often will not be electron-transparent, as the formed ice layer is far too thick. Blotting can be used to reduce the thickness of the ice layer, but it is not reliable and often requires many attempts to produce a thin ice layer, especially when the form factor of a TEM sample changes. To overcome this, cryo-focused ion beam (FIB) can be used to thin and polish away excess ice to expose the interface between

the corroded alloy and the electrolyte (see 6.2), allowing the oxide and hydroxide phases at the interface to be examined with cryo-TEM [227, 228].

In this study, we will examine the early-stage aqueous corrosion of a NiCrMo alloy. It is well known that the addition of Mo to NiCr-based alloys inhibits the breakdown of passive films during aqueous corrosion, improving corrosion resistance [38, 39, 229–231]. During aqueous corrosion, different oxides and hydroxides form at the alloy surface. For instance, rocksalt NiO is commonly reported to form on corroded Ni metal and Ni-based alloys with a cube-on-cube epitaxial relationship (Figure 6.1) [232–234]. With HREM, EELS, and atom-probe tomography analyses of corroded and oxidized NiCrMo alloys, the surface oxides were determined as a combination of rocksalt and corundum crystal structures with Ni, Cr, and traces of Mo in the rocksalt and Ni and Cr in the corundum due to nonequilibrium solute capture [40]. As previous studies have shown that corundum Cr_2O_3 has a larger thermodynamic driving force than NiO in Ni-based alloys [235], these experimental observations contradict the assumption that the most thermodynamically stable oxide forms first. Instead the composition of the oxide is determined by the growth rate at the metal-oxide interface, and local thermodynamic equilibrium is not present. We note that the chemical formulas for oxides and hydroxides are written as $\text{Ni}_{1-x}\text{Cr}_{2x/3}\text{O}$ and $\text{Ni}_{1-x}\text{Cr}_{2x/3}(\text{OH})_2$ throughout this chapter, as the chemical compositions of these phases were not confirmed. Since there is a strong possibility that solute capture can occur in the formation of the oxide and hydroxide phases, it is appropriate to denote both Ni and Cr as constituent metals in the phases for completeness, as oxides with unusual and often inconsistent compositions were previously observed in a similar corrosive condition [40, 107]. What is not known in detail is to what extent stable hydroxides and oxyhydroxides [236–238] form near the surface in aqueous conditions, and any crystallographic relationships to the oxide or metal. Here, we present a workflow allowing for the preservation of the metal-electrolyte interface of NiCrMo alloy samples, and subsequent cryo-TEM characterization of the oxides and hydroxides in the near-native hydrated state, observing the early-stage aqueous corrosion in these corrosion-resistant alloys.

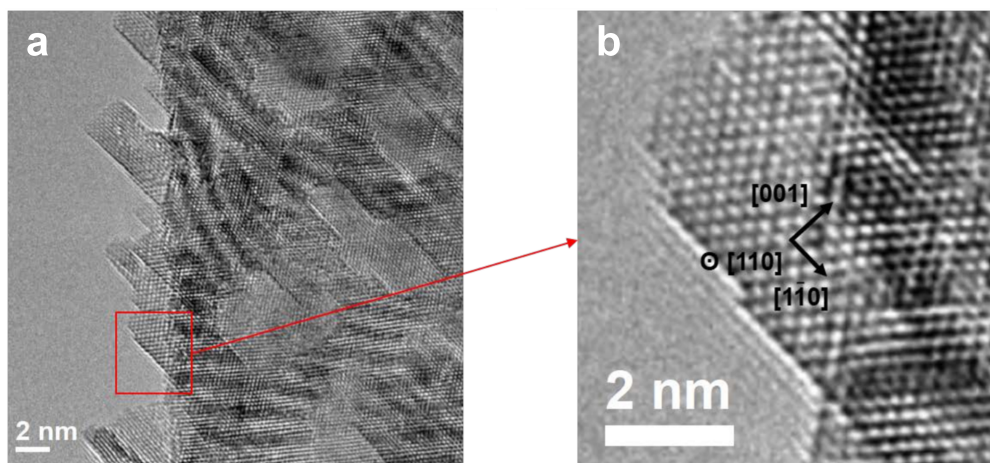


Figure 6.1. HREM images show that the rock-salt islands grown on NiCrMo substrate oxidized in sodium sulfate for 10^4 seconds. Adapted from [40].

6.2 Experimental Details

6.2.1 Sample Preparation

A Ni-22Cr-6Mo alloy was cut into discs with a diameter of 3 mm and a thickness of ~ 0.5 mm using a rotary disc cutter (South Bay Technology Model 360), and were mechanically thinned to thicknesses of $\sim 100 \mu\text{m}$ with silicon carbide lapping paper. The discs were mechanically dimpled (VCR Model D500i Dimpler) until their center was $\sim 25 \mu\text{m}$ thick. Then, each disc was cut into two halves using a wire saw (South Bay Technology Model 850) to make the thin edge of the sample (which contains the alloy-hydroxide-water interface) accessible to the Ga^+ beam of the FIB. If the disc was not sectioned, the edge would be obstructed by the top half of the disc during cryo-FIB milling. The samples were ultrasonically washed with acetone and thinned to electron transparency using the Ar^+ ion beam of a Fischione Model 1050 TEM Mill operated at 5 kV with a 6° milling angle for 2 h, followed by a final polish at 1 kV with a 2° milling angle for 1 h. The choice of ion milling, rather than electropolishing here was deliberate. As detailed in the next section, the samples were deliberately corroded for a long time to obtain a quasi steady-state, relatively thin oxide. For this purpose, it is advantageous to have an initial, somewhat damaged surface which is removed during the

corrosion treatment, rather than a semi-passivated surface after electropolishing which may have viscosity control agents at the surface.

6.2.2 Aqueous Corrosion and Freezing

The NiCrMo half-discs were corroded in 200 mL of a stock solution containing 0.1 M NaCl and 0.0001 M HCl in H₂O (pH \sim 4.0), with 5 μ L of H₂O₂ (30 % w/w) injected above the sample surface to increase oxidation rate. The condition was verified by Dr. Katie Lutton and Prof. John Scully at the University of Virginia to produce an electrochemical potential near +0.2 V versus a saturated calomel reference electrode, a potential within the passive region. Verification of the chemical potentiostat approach was achieved by observing identical oxides in electrochemical impedance experiments [40]. In all cases, the samples were corroded for 10⁴ s at room temperature. Then, they were removed from the aqueous solution, rapidly frozen via plunge freezing in liquid ethane [239], and transferred to a cryogenic grid box immersed in liquid nitrogen.

6.2.3 Cryo-FIB Milling

Due to the added ice layer formed during freezing, the pre-thinned samples were too thick for direct TEM imaging, and FIB milling was required to thin the samples and expose the oxide and hydroxide phases at the alloy-water interface. A Quorum PP3010T Cryo-FIB/SEM Preparation System, attached to a FEI Strata 235 dual-beam FIB, was used to image and mill the frozen alloy samples at low temperatures (\leq -140 °C). Firstly, the frozen samples were mounted into a Quorum 12406 sample shuttle such that the Ga⁺ beam inside the FIB hits the sample at a glancing angle. Using a transfer rod keeping the sample in a nitrogen atmosphere, the shuttle was then transferred into a cryo-preparation chamber, which was operated at a pressure of 10⁻⁷ mbar and kept at -160 °C to prevent a phase change to the hexagonal ice phase. Then, the shuttle was transferred into the FIB chamber through a connecting valve between the cryo-preparation chamber and the FIB and secured onto the stage kept at -160 °C. The frozen alloy samples were imaged with a 5 kV electron beam prior

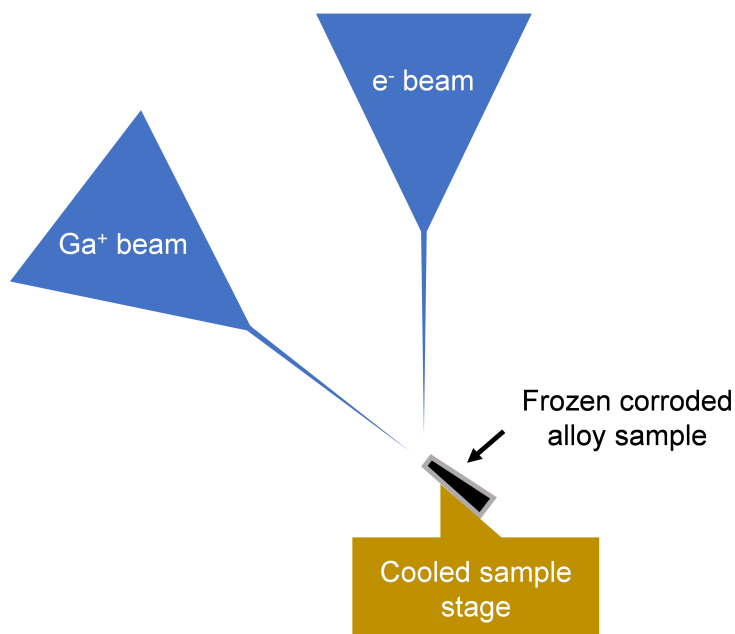


Figure 6.2. Schematic showing the cryo-FIB milling process of a frozen corroded NiCrMo alloy, which is mounted to a cooled stage.

to cryo-FIB milling. In contrast to the traditional TEM sample preparation using the FIB, where a series of cleaning cross-sections are completed on a single lamella, we selected regions along the thin ion-milled portion of the 3 mm half-disc and milled it from one side with a 30 kV Ga⁺ ion beam. An illustration of the workflow inside the FIB is shown in Figure 6.2. This milling method reduced the excess ice and the thickness of the alloy at the very edge of the sample and added notched markers for easier identification during cryo-TEM imaging. An ion beam current of 100 pA was initially used to line mill toward the sample with stage tilt angles of 5-10°, then the current was decreased stepwise down to 20 pA for the final cleaning step. The beam current values used have been shown to produce sufficiently thin lamellae of hydrogels and liquid-solid interfaces in oxide particles [240], demonstrating that the areas of interest at the alloy-water interface can be preserved with cryo-FIB milling.

6.2.4 Cryo-TEM Characterization

The FIB milled sample was transferred to a cooled Gatan 915 double tilt cryo-transfer holder, which has a shutter to prevent the sample from being exposed to air during the

transfer. Cryo-TEM characterization was performed on a FEI Titan TEM operated at 300 kV with a Gatan Orius 830 ($2k \times 2k$) CCD camera for diffraction pattern and image collection. Selected-area electron diffraction (SAED) patterns and corresponding dark field (DF) images from various regions of a polycrystalline diffraction ring were taken near the thin sample edge.

6.2.5 TEM Characterization of Conventionally-Prepared Specimens

For TEM characterization of conventionally-prepared specimens, the NiCrMo half-discs were dried in air after aqueous corrosion instead of being plunge-frozen from their hydrated state. Electron diffraction and high-resolution imaging of the dehydrated samples were performed on a JEOL JEM-2100F TEM operated at 200 kV.

6.3 Results

When milling the sample, the ice layer resulted in a smooth surface formed, whereas the alloy showed significant curtaining. This allowed for easy identification of the two different materials during milling such that we could observe a 10-20 μm thick ice layer was preserved by plunge freezing. Such a thick layer would not be electron-beam transparent in the TEM, requiring it to be thinned. The cryo-FIB milling approach provided locally thin regions with smooth surfaces at the alloy-water interface. With SEM and FIB imaging of the NiCrMo half-disc, we observed minor ice contamination on the alloy surface (Figure 6.3) that grew during the cryo-transfer processes. The FIB milling not only reduced the overall thickness of the vitreous ice layer, but also removed most of the small ice crystals in the regions of interest (Figure 6.4). This allowed for characterization of the phases at the alloy-water interface during semi steady-state aqueous corrosion without extraneous scattering signals in images and diffraction patterns. As mentioned in the Methods and Materials section, several regions along the edge of the half-disc were thinned with the ion beam. In cryo-TEM images, the differences between FIB milled and unmilled regions become more apparent (Figure 6.5a). The FIB milled regions are electron-transparent and local diffraction contrast can be

discerned, whereas adjacent regions are almost completely covered by ice which blocks the electron beam.

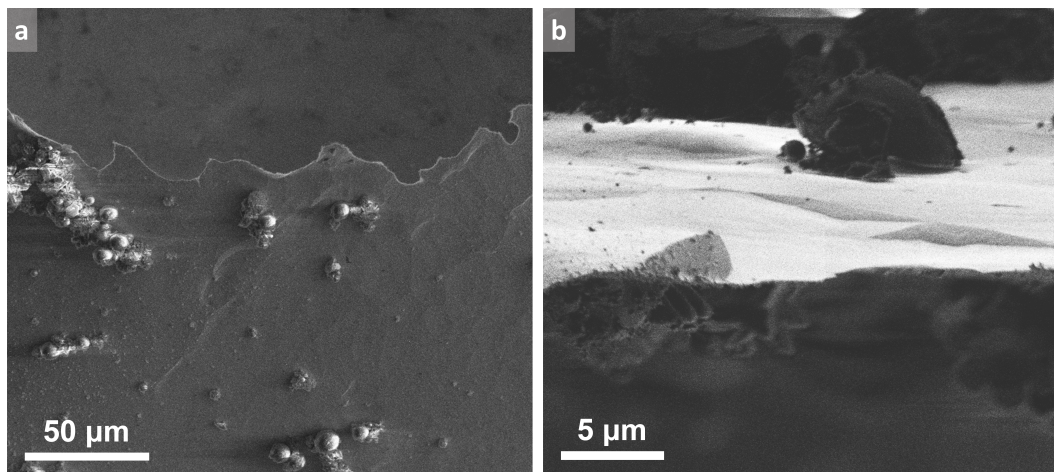


Figure 6.3. (a) Cryo-SEM secondary electron image of the frozen corroded NiCrMo half-disc. The irregular top edge is the region that was pre-thinned to electron transparency with Ar^+ ion milling and the bright particles are ice crystals, which charge in the electron beam. (b) A top-down FIB secondary electron image of (a) shows that ice contamination (dark particles) is more significant in the lower part of the half-disc, away from the thin alloy edge.

SAED patterns taken from the thinned region show that the alloy-oxide-hydroxide region was successfully preserved (Figure 6.5b). In cryo-TEM images of milled regions, we only observe the presence of the native ice layer from the initial plunge freezing as opposed to hexagonal ice crystals. From SAED patterns of two different sites in the region shown in Figure 6.5, we can conclude the presence of oxides, hydroxides, and in some cases, vitreous ice. Specifically, polycrystalline diffraction rings indicate that the rocksalt $\text{Ni}_{1-x}\text{Cr}_{2x/3}\text{O}$ phase forms on the NiCrMo alloy surface, as expected from previous TEM characterizations of conventionally-prepared samples from the same alloy system [40] and similar oxidation experiments for Ni metal and other NiCr-based alloy systems [166, 208, 209, 233].

In addition to the rocksalt phase, polycrystalline $\beta\text{-Ni}_{1-x}\text{Cr}_{2x/3}(\text{OH})_2$ is identified in the SAED patterns. While we can be definitive that the crystal structure matches that of $\beta\text{-Ni}(\text{OH})_2$ we cannot exclude the strong possibility that Cr has been solute captured

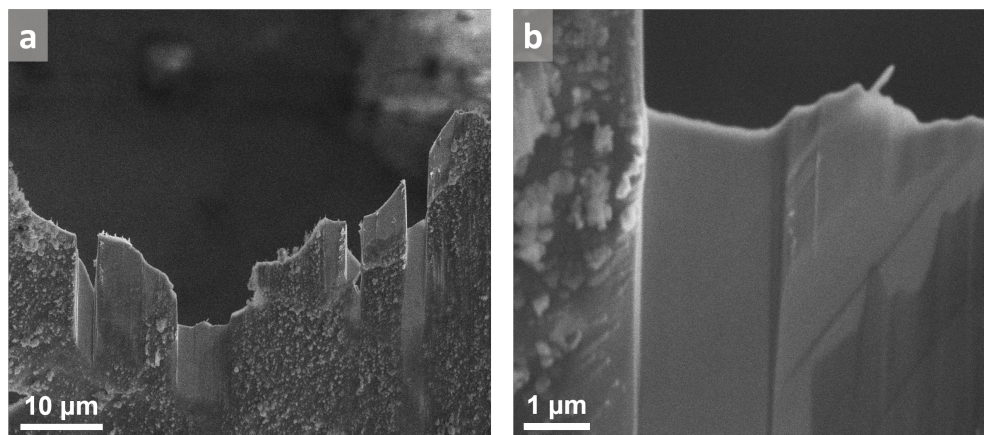


Figure 6.4. Secondary electron image of (a) the cryo-FIB milled regions that also served as notched markers to identify regions of interest for cryo-TEM imaging. (b) Higher magnification image showing that the regions that were thinned have significantly less contamination in comparison with unthinned regions.

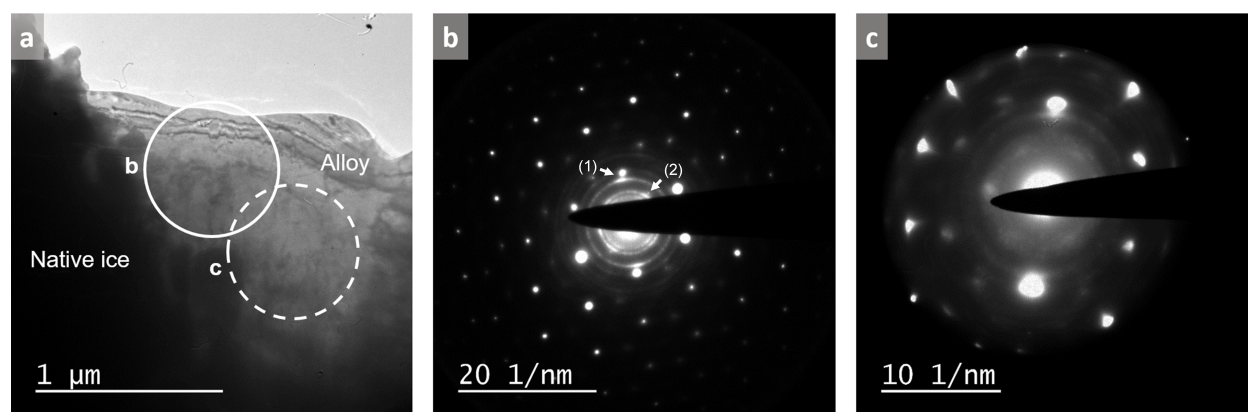


Figure 6.5. (a) Cryo-TEM imaging of cryo-FIB milled region. SAED patterns from alloy regions show (b) polycrystalline $\beta\text{-Ni}_{1-x}\text{Cr}_{2x/3}(\text{OH})_2$ with rocksalt $\text{Ni}_{1-x}\text{Cr}_{2x/3}\text{O}$ and (c) rocksalt and corundum oxide phases. (b) Orientational relationships between (1) the (110) $\text{Ni}_{1-x}\text{Cr}_{2x/3}(\text{OH})_2$ ring and the (220) Ni spots and (2) the (101) $\text{Ni}_{1-x}\text{Cr}_{2x/3}\text{O}$ ring and the (111) rocksalt spots are observed. (c) In the thicker part of the sample, the inner diffraction rings are more diffuse and correspond to vitreous ice and the major diffraction vectors of polycrystalline corundum.

in the hydroxide, i.e. it is $\beta\text{-Ni}_{1-x}\text{Cr}_{2x/3}(\text{OH})_2$ [241, 242]. With DF imaging on the $\beta\text{-Ni}_{1-x}\text{Cr}_{2x/3}(\text{OH})_2$ polycrystalline diffraction rings, the location of $\beta\text{-Ni}_{1-x}\text{Cr}_{2x/3}(\text{OH})_2$ at the surface of the NiCrMo was confirmed (Figure 6.6), suggesting that the hydrated alloy with the oxide and hydroxide phases is successfully preserved by the plunge freezing and cryo-FIB

preparation process. The $\beta\text{-Ni}_{1-x}\text{Cr}_{2x/3}(\text{OH})_2$ phase was not observed in previous TEM characterizations of aqueous corrosion in conventionally-prepared Ni and NiCr specimens when the samples were dehydrated after corrosion. The DF images also indicate that the $\beta\text{-Ni}_{1-x}\text{Cr}_{2x/3}(\text{OH})_2$ crystallites, which are about 5-10 nm in diameter, form a layer at the edge of the alloy sample. Furthermore, some of the $\beta\text{-Ni}_{1-x}\text{Cr}_{2x/3}(\text{OH})_2$ crystallites are also distributed on the top surface of the alloy that lies parallel to the projection plane. As shown in Figure 6.6c, many small $\beta\text{-Ni}_{1-x}\text{Cr}_{2x/3}(\text{OH})_2$ crystallites oriented in the (101) direction formed on the surface of the alloy bulk. This kind of crystallite distribution was not observed in the DF image of the $\beta\text{-Ni}_{1-x}\text{Cr}_{2x/3}(\text{OH})_2$ oriented in the (110) direction.

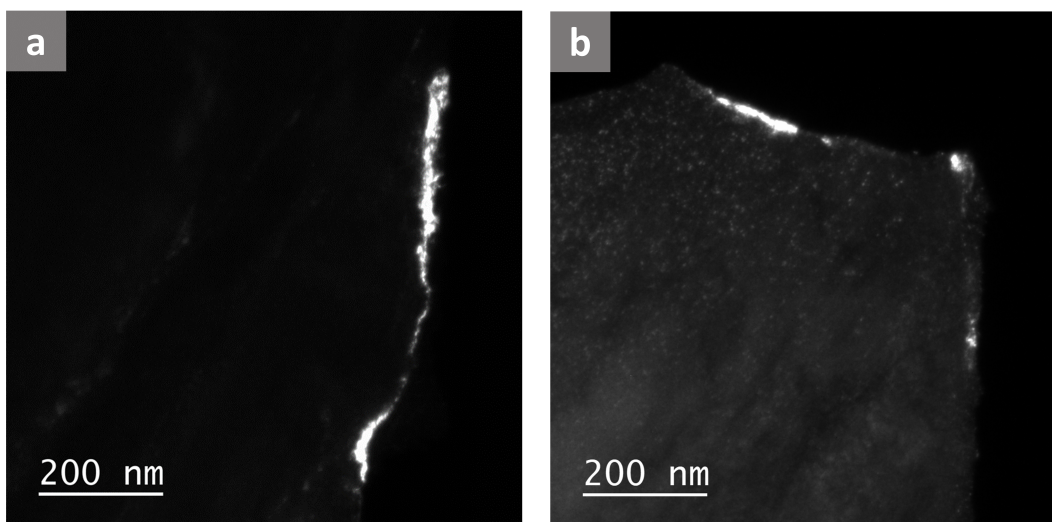


Figure 6.6. Dark-field images taken from (a) the (110) $\text{Ni}_{1-x}\text{Cr}_{2x/3}(\text{OH})_2$ diffraction ring and (b) the (101) $\text{Ni}_{1-x}\text{Cr}_{2x/3}(\text{OH})_2$ diffraction ring. As indicated in both images, the $\text{Ni}_{1-x}\text{Cr}_{2x/3}(\text{OH})_2$ nanocrystals contributing to the diffraction lie on the edges of the Ni-alloy bulk.

The $\beta\text{-Ni}(\text{OH})_2$ phase is a well-ordered phase which shows sharp diffraction peaks [243, 244]. For completeness, we should mention that there is one other hydroxide phase reported in the literature, $\alpha\text{-Ni}(\text{OH})_2$ [243, 244]. The $\alpha\text{-Ni}(\text{OH})_2$ phase is significantly more disordered, and shows broad diffraction features in the literature (Fig. 6.7). As there is significant overlap of the diffraction features with those of vitreous ice [224] and to some extent, $\beta\text{-Ni}(\text{OH})_2$ [238, 244], we cannot exclude the possible presence of some $\alpha\text{-Ni}_{1-x}\text{Cr}_{2x/3}(\text{OH})_2$ along with

β -Ni_{1-x}Cr_{2x/3}(OH)₂ in the samples. Since it is probable that hydroxides exist in the form of hydrogels prior to freezing, the Ni(OH)₂ is probably trapped in a metastable state.

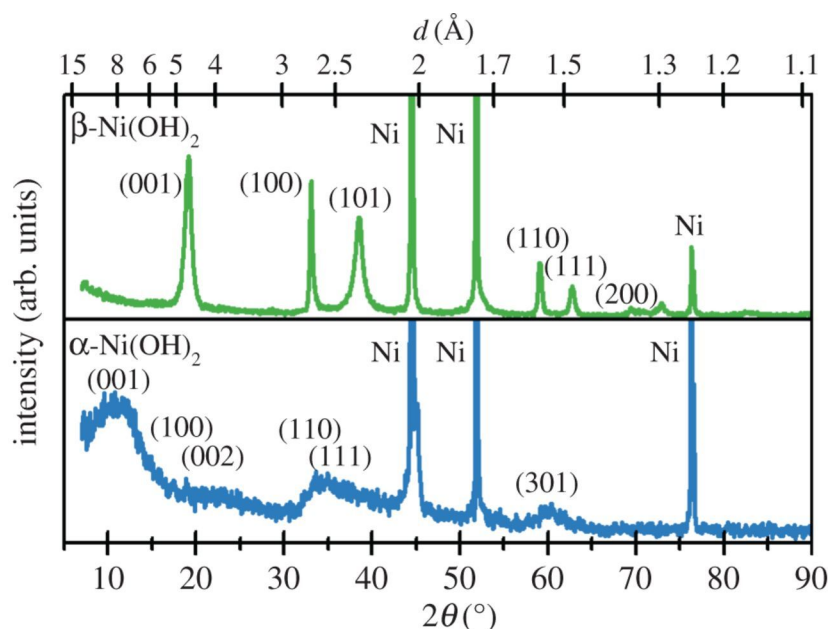


Figure 6.7. X-ray diffraction patterns of β -Ni(OH)₂ and α -Ni(OH)₂. Adapted from [238].

We can further conclude orientational relationships between β -Ni_{1-x}Cr_{2x/3}(OH)₂, rocksalt, and the bulk alloy from the SAED patterns. The polycrystalline rings have an inhomogeneous intensity distribution, indicating preferential orientation of the β -Ni_{1-x}Cr_{2x/3}(OH)₂ crystallites. The (110) diffraction ring of β -Ni_{1-x}Cr_{2x/3}(OH)₂ in particular has intensity maxima near the (220) diffraction spots of Ni. In addition, we observe evidence of other orientational relationships from the weaker diffraction spots; for instance, the (101) β -Ni_{1-x}Cr_{2x/3}(OH)₂ ring is more intense near the (111) rocksalt spots (Figure 6.5b). This observation differs from previous diffraction studies of the cube-on-cube epitaxy between rocksalt and Ni [233] or NiCr alloys [40] in conventionally-prepared samples.

The characterization of conventionally-prepared samples was independently verified for this paper using the same aqueous corrosion treatment. Rocksalt Ni_{1-x}Cr_{2x/3}O islands were observed with HREM on a corroded NiCrMo (Figure 6.8a). Consistent with literature [40, 233, 234], electron diffraction of the islands showed that the rocksalt phase grew on the bulk

Ni metal with a cube-on-cube epitaxy (Figure 6.8b). In contrast to the cryo-TEM results of the frozen-hydrated sample as discussed earlier, the polycrystalline β - $\text{Ni}_{1-x}\text{Cr}_{2x/3}(\text{OH})_2$ phase was not observed in this non-cryogenic TEM sample preparation and characterization, indicating the need for a cryogenic approach to reveal the complex orientational relationships between the oxides and hydroxides with the bulk metal.

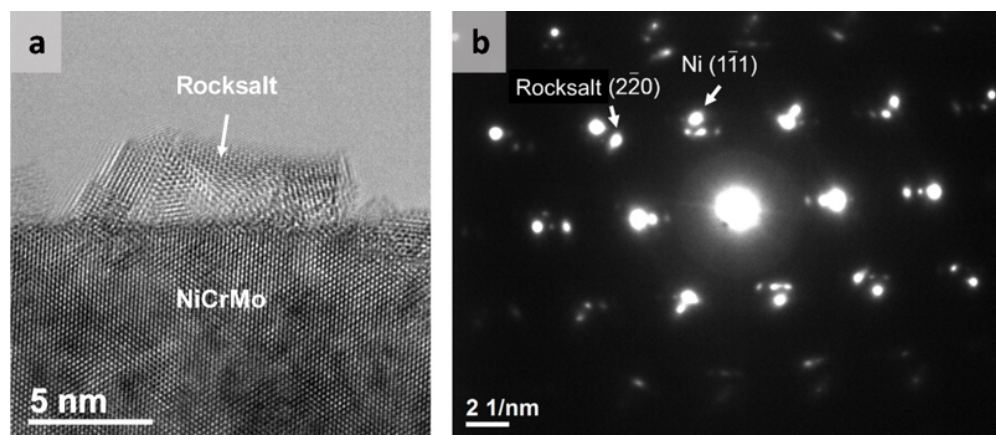


Figure 6.8. Conventionally-prepared NiCrMo sample shows the growth of rocksalt $\text{Ni}_{1-x}\text{Cr}_{2x/3}\text{O}$ islands. (a) HREM image and (b) the corresponding SAED pattern obtained from the $\text{Ni}_{1-x}\text{Cr}_{2x/3}\text{O}$ - metal interface shows cube-on-cube epitaxy.

6.4 Discussion

The results presented indicate that it is possible to examine aqueous corroded samples by a cryogenic approach, and obtain local structural information that is not accessible by other means. As observed in other studies, these samples are complex polycrystalline and non-conformal oxides/hydroxides, not the simple series of layers, all of equal thickness, commonly hypothesized in the literature [245–249]. While elements of the epitaxial arrangements are consistent with prior work in furnace oxidation [233] and aqueous corrosion [207–209], a different type of epitaxy was identified. In both cases, parallel cube-on-cube $\text{Ni}_{1-x}\text{Cr}_{2x/3}\text{O}$ on Ni epitaxy was observed in the passive oxide layer. Additionally, $\text{Ni}(\text{OH})_2$ was identified on Ni(111) single crystal surfaces in both alkaline and acidic solutions via in situ electrochemical STM, and the thickness and morphology of the hydroxide layer were determined to vary with

the passivation potential [207]; in some cases there was probably an underlying oxide between the metal and the hydroxide which STM would not detect. While preferred orientations of the $\text{Ni}(\text{OH})_2$ were not found for the electrochemical conditions of the study by Zuili et al. [207], we have identified two separate cases of preferred orientation for $\beta\text{-Ni}_{1-x}\text{Cr}_{2x/3}(\text{OH})_2$. In contrast to previous observations, where only amorphous granular $\text{Ni}(\text{OH})_2$ or a partial monolayer of the $\text{Ni}(\text{OH})_2$ (0001) basal plane were identified, we observed a polycrystalline $\beta\text{-Ni}_{1-x}\text{Cr}_{2x/3}(\text{OH})_2$ layer with $\beta\text{-Ni}_{1-x}\text{Cr}_{2x/3}(\text{OH})_2$ (101) crystallites preferentially oriented in the six-fold Ni (111) and rocksalt (111) direction, as well as $\beta\text{-Ni}_{1-x}\text{Cr}_{2x/3}(\text{OH})_2$ (110) crystallites that were preferentially oriented along the two-fold Ni (220). Electron diffraction of the hydroxide and the passive oxide layer has shown that the hydroxide conforms to the structure of the underlying passive layer. In agreement with previous studies of the lattice mismatch between NiO and $\text{Ni}(\text{OH})_2$ (7.5%) [207, 232, 237], the lattice mismatches for the two orientational relationships observed in this study were both between 5-7%. The crystallite sizes for $\beta\text{-Ni}_{1-x}\text{Cr}_{2x/3}(\text{OH})_2$, which range from 5-10 nm, are also in good agreement with previous studies of granular $\text{Ni}(\text{OH})_2$ structures, where grain size sizes between 2 and 8 nm were measured [207].

Despite the successful preservation of the surface structure through cryogenic preparation and analysis, many unanswered questions remain about these complex systems. The literature suggests that chloride ions could be trapped in the hydroxide (substituting for OH^-) during aqueous corrosion [245, 250], which motivates further study. There are also many open issues as to whether the hydroxide phase is purely nickel hydroxide or whether it incorporates chromium and/or molybdenum. The valence states are also important to understand the electrochemical reactions, for instance whether one has Mo^{4+} or Ni^{3+} in the hydroxide. This merits further attention. Minor chemical and electronic fluctuations in the hydroxide have little effect on its structure and morphology, causing these details to be overlooked in diffraction-based studies such as this one. These effects will be studied in more detail and with more advanced methods in future work.

The approach is not without its limitations. For instance, specimen drift and charging remain a challenge in cryo-TEM [251]. Minor chemical fluctuations, such as the capture of chromium and molybdenum in the oxide and hydroxide, are often localized and would require HAADF imaging and EDS. Identification of the valence states would require EELS. While EDS and EELS are standard chemical characterization techniques for TEM, considerable experimental design is required to ensure the collected spectra are representative of the hydrated alloy sample during cryo-TEM characterization. These challenges are being addressed with promising results [252]. The results presented in this chapter are just the first steps in establishing a cryo-TEM based technique to understand early-stage oxidation processes.

6.5 Conclusions

With a combined cryo-FIB and cryo-TEM approach, a corroded NiCrMo alloy was investigated in its a frozen-hydrated state during aqueous corrosion. While the morphology of the corroded alloy can be imaged with the cryo-FIB microscope, the cryo-TEM can be used to observe the crystallography and possibly the chemistry of the oxide and hydroxide layers formed. Additionally, the presence of nonequilibrium phases can be studied in more detail, as the samples were cryo-immobilized and any kinetic effects such as oxide aging and evolution would be minimized. In this chapter, NiCrMo half-discs were mechanically polished and ion milled prior to aqueous corrosion, and the resulting corroded specimens were immediately plunge-frozen using liquid nitrogen. Cryo-FIB milling thinned down the ice layer to electron transparency. Cryo-TEM imaging and electron diffraction revealed the presence of rocksalt and polycrystalline $\text{Ni}_{1-x}\text{Cr}_{2x/3}(\text{OH})_2$ on the surface of the corroded NiCrMo, supporting that these phases were formed onto the alloy during aqueous corrosion in a Cl^- -containing electrolyte solution. The $\text{Ni}_{1-x}\text{Cr}_{2x/3}(\text{OH})_2$ phase, which has not been observed in previous TEM characterizations of corroded NiCrMo alloys, have multiple orientational relationships in the hydrated alloy sample. These complex orientational relationships between the oxides

and hydroxides with the bulk metal were studied with SAED and DF imaging, thereby establishing an efficient workflow which will allow detailed studies of orientational relationships in several materials systems undergoing aqueous corrosion.

***In situ* Observations of Graphitic Staples in Crumpled Graphene**

As described earlier in Section 2.2.2, *in situ* TEM allows for the ability to observe nanoscale and atomic scale details with real-time imaging as a material is deformed. The same experimental approach has been applied to understanding the atomic scale processes taking place in 2D layered materials such as graphite [253, 254] and molybdenum disulfide [255, 256] during sliding. Furthermore, similar *in situ* specialized TEM holders have been recently used to study electrical properties such as localized resistance in graphitic nanostructures [257] and piezoresistive responses in core-shell nanowires [258]. These results demonstrate that the *in situ* TEM approach can not only be used to characterize the local stress, strain, and defect structures of various materials under mechanical loading [259, 260], but the electromechanical couplings in these materials systems as well.

The work in this chapter demonstrates the versatility of the *in situ* AFM-TEM sliding holder. The same experimental approach has been applied to understanding the atomic scale processes taking place in 2D layered materials such as graphite [254] and molybdenum disulfide [255, 256]. Crumpled graphene, which is a mixture of regions that can act similar to single graphene sheets and local regions of nanoscale graphitic crystals, has a more complex nanoscale structure. Graphene is an exceptionally effective lubricant additive that performs well when crumpled rather than as flat sheets. *In situ* TEM of crumpled graphene sliding demonstrates that it possesses intra-sheet links and graphitic nanocrystals that provide additional mechanical stability and enable the material to reversibly deform. Crumpled graphene is closer to crumpled paper with additional staples between the sheets, with the intra-sheet links and graphitic nanocrystals acting as graphitic staples. The results and analysis from this chapter, along with the supplementary videos referenced below, have been published in the journal *Carbon* (see reference [261]). Video captions can be found in the

Appendix. This work is performed collaboratively with Prof. Albert Dato and Prof. Gordon Krauss from the Department of Engineering at Harvey Mudd College.

7.1 Introduction

The extraordinary mechanical and chemical properties of graphene, known for its atomically thin layer of carbon atoms arranged in a honeycomb lattice, are well understood and the number of potential applications that exploit them is rapidly increasing. For instance, graphene is one of the strongest materials measured to date [262] and is commonly used in multifunctional nanocomposites [263]. Combined with its unique electrical properties [264, 265], the mechanical behavior of graphene motivates its use in components with sliding interfaces in micro- and nanoelectromechanical systems [266–270]. Graphene is an attractive material for tribological applications because of its extreme mechanical properties, chemical stability [271], and low coefficient of friction [272]. Flat graphene sheets have proven effective [272, 273] for wear resistance in some cases, but for many applications one wants to deliver graphene via a liquid such as a lubricant oil [269, 274, 275]. Flat graphene sheets tend to aggregate due to strong van der Waals attractions, while crumpled graphene, which can be produced by the substrate-free gas-phase synthesis method [276–278] is resistant to aggregation due to its network of ridges and vertices [279–282]. Although crumpled graphene was shown to outperform other carbon-based lubricant additives in macroscale tribometer tests [275], the nanoscale tribological behavior is not well understood. It is generally believed that crumpled graphene behaves similarly to other crumpled thin sheets such as paper and foils [283–285], but this has not been directly verified.

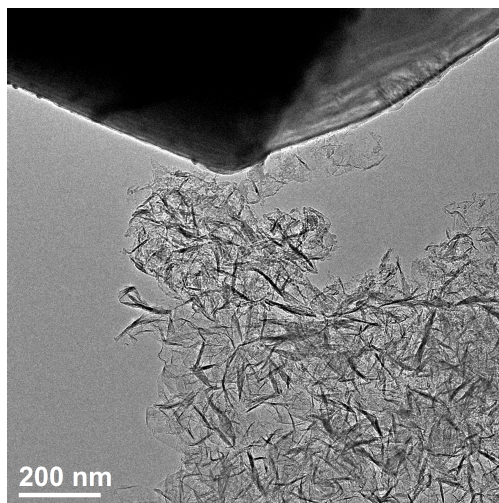


Figure 7.1. Graphitic staples in crumpled graphene nanosheets.

7.2 Experimental Methods

7.2.1 Crumpled Graphene Synthesis

Crumpled graphene sheets were synthesized in an atmospheric-pressure microwave (2.45 GHz) plasma reactor (MKS/ASTeX AX2518). Argon gas is passed through a quartz tube (21 mm internal diameter) at a rate of 1.71 L/min through a microwave guide to generate an argon plasma at an applied microwave forward power of 250 W. A jet nebulizer was used to generate an aerosol consisting of argon gas (2 L/min) and ethanol droplets (2×10^{-4} L/min). A smaller alumina tube (3 mm internal diameter) that was located within the quartz tube was used to pass the aerosol directly into the plasma. Ethanol droplets rapidly evaporated in the plasma and dissociated to form solid matter. The products were rapidly cooled and then collected downstream on nylon membrane filters. The solid carbon material was collected at a rate of 2 mg/min. The material produced by this method has been shown to be pure and highly ordered graphene [276–278]. The collected graphene sheets were sonicated in ethanol for 1 min, resulting in the formation of a homogeneous black suspension. The crumpled graphene synthesis was completed by Prof. Albert Dato and Prof. Gordon Krauss at Harvey Mudd College.

7.2.2 Transmission Electron Microscopy

Approximately 8-10 drops of the graphene solution were deposited on a fractured Si transmission electron microscopy TEM aperture grid glued on to a sharpened W needle, which allows the sample to be mounted into the AFM-TEM holder. The Si fragment sat on a hot plate set to 50 °C for quick solution evaporation. The Nanofactory Instruments AFM-TEM holder, which contained a Si AFM tip with a spring constant of 5.6 N/m [286], was inserted into a 200 kV FEI Tecnai F20ST TEM at Argonne National Laboratory, which was used to characterize the tribological behavior of graphene sheets. A schematic of the AFM-TEM holder is shown in Figure 7.2. The sample could move three-dimensionally in the holder via a piezomotor with resolutions of 0.2 Å in the x and y directions, and 0.025 Å in the z direction. *In situ* sliding was completed by moving the sample towards a stationary AFM tip. A TV-rate video camera was used to record the *in situ* sliding experiments. The graphene samples were re-examined *ex situ* in a 200 kV Hitachi H-8100 TEM and a 200 kV Hitachi HD-2300 STEM at Northwestern University before and after *in situ* TEM experiments.

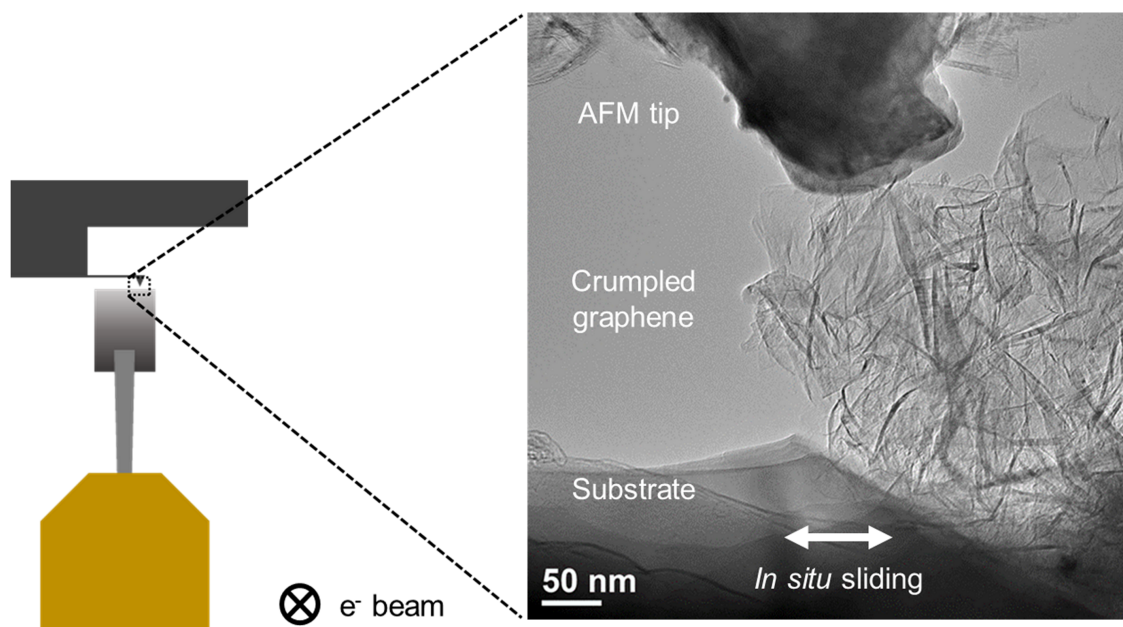


Figure 7.2. *In situ* sliding in the TEM is performed by moving the specimen against a stationary AFM tip.

7.3 Results and Discussion

We demonstrate here that crumpled graphene is not simply folded paper, but significantly different, using transmission electron microscopy (TEM) to visualize fiction and wear events *in situ* with high resolution. Starting from drop-casted graphene sheets (see Section 7.2.1), we analyzed the nanoscale structural changes of crumpled graphene in real-time and observed in addition to the graphene sheets two types of graphitic structure: local regions with two, perhaps three folded graphene layers in a single graphene sheet, which we will refer to as intra-sheet links, and small regions with many folded layers, which we will refer to as needle-like graphitic nanocrystals. We use here and in the following sections the term “graphitic“, since the evidence indicates that they are primarily sp^2 bonded regions, but we cannot exclude some sp^3 bonding at edges. The graphitic nanocrystals were verified using higher-resolution imaging and electron diffraction (Figure 7.3). These nanocrystals behave similarly to crosslinks in polymers, adding mechanical stability. The *in situ* sliding tests show that intra-sheet links within single graphene sheets changed morphology due to tensile and compressive forces. In contrast, regions that contain graphitic nanocrystals behaved like strong crosslinks and have little or no structural change during compression, tension, or shear. We will first discuss the larger-scale behavior, showing that it is comparable to prior

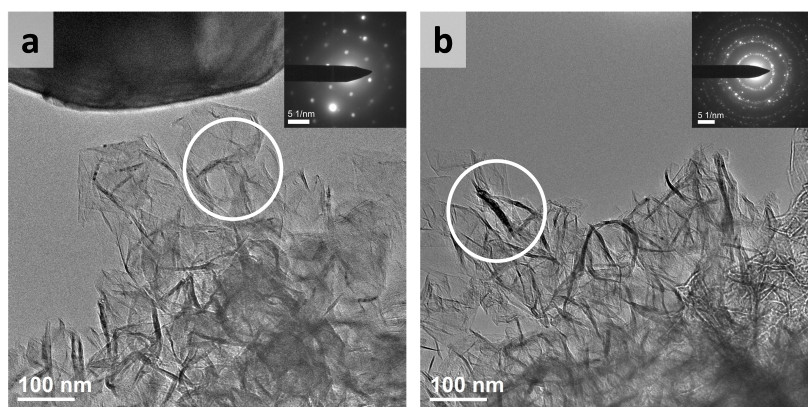


Figure 7.3. Transmission electron diffraction patterns taken from the regions in the respective TEM images, indicated by circles, show (a) intra-sheet links and (b) graphitic nanocrystals.

reports [280, 287] to cross-validate the more local *in situ* results which we will discuss later.

Initially dispersed nanosheets with no preferential organization were collected during the *in situ* sliding and formed a crumpled ball, which comprised of several crumpled graphene sheets (Figure 7.4 and Video S1). As sliding continued, more sheets were added to the solid. The combination of shear and compressive forces aided the formation of a spherical solid of intra-sheet links. The crumpled graphene ball, which is approximately 350-500 nm in diameter, exhibited characteristics of a non-deformable sphere and was formed from links between multiple graphene sheets. Experimentally we observed rolling in two different

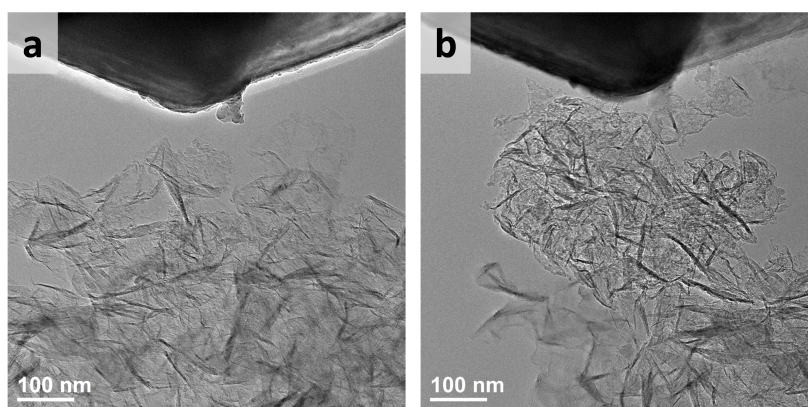


Figure 7.4. (a) Prior to sliding and compression, crumpled graphene sheets have no preferential order. (b) After sliding and compression, a 3D non-deformable solid with a higher density of graphitic regions, was formed.

planes – in both the plane parallel to and the plane perpendicular to the direction of sliding. As the solid reached a size of approximately 400-500 nm in diameter, it did not add any additional graphene sheets. We also observed stick-slip in the non-deformable solid (Video S1), which can be attributed to the individual graphene intra-sheet links at the surface of the sphere. These minor intra-sheet links could be thought of as large asperities on a rounded surface. This further confirmed that the solid was constructed of many individual intra-sheet links, which were able to resist the compressive forces on the AFM tip by pinning these individual crumpled sheets together and preventing the individual rippled layers from unfolding back to the original state. The crumpled graphene ball's resistance to compression matched the observed behavior of crumpled thin sheets [288–291], and the ridges in the crumpled graphene were also irreversibly wadded into folds [292]. We now turn to the local

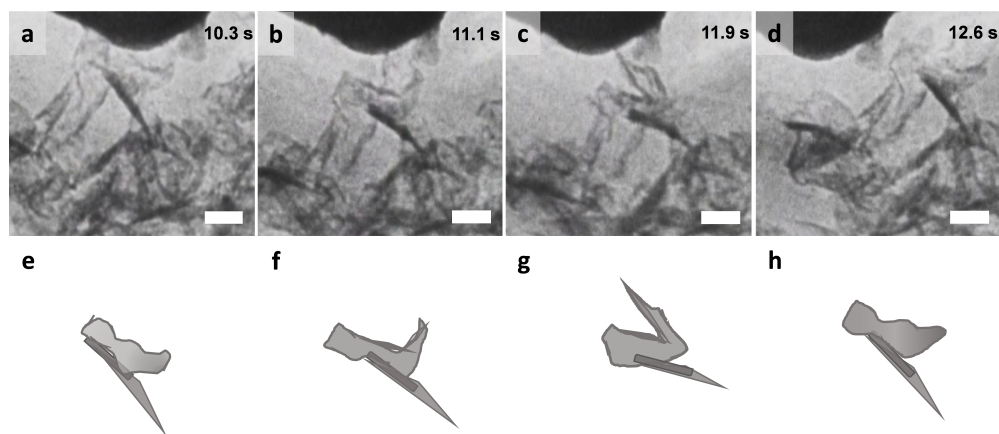


Figure 7.5. (a-d) TEM images extracted from Video S2 displaying that (b-c) the crumpled graphene sheet supported by a graphitic nanocrystal folds as it makes contact with the AFM tip, and then (d) unfolds as it passes the tip. As the graphene sheet folded, edges of the sheet were reoriented into graphitic regions. (e-h) Graphical models showing the structural changes occurring as the sheet was sliding against the tip. The sample is moving from left to right in this sequence. Scale bars, 50 nm.

processes taking place at the nanoscale, showing that localized regions within the crumpled graphene sheets changed structurally during sliding. Three examples are shown (Videos S2-S4). In the first example, a single crumpled graphene sheet changed structurally as it made contact with the AFM tip (Figure 7.5 and Video S2). The graphene sheet folded onto itself, and then unfolded to approximately its original shape as it slid past the tip. As the graphene sheet folded, we observed that the contrast in the sheet became stronger, indicating a transformation from single layer to few-layer graphene [293]. When the graphene unfolded, we observed the opposite. By sliding this single crumpled sheet back and forth, this structural change was reproduced, suggesting that this folding and unfolding process in crumpled graphene is reversible. We note that this process is comparable to what has been shown in experiments with controlled crumpling and unfolding of graphene [282, 294] and previous TEM observations of single layer regions and few-layer regions such as folded edges of graphene sheets [276, 293].

In the second example, we see folding and unfolding occurring in suspended graphene sheets (Figure 7.6 and Video S3). In some of the graphitic needle-like regions near the tip

we observed changes in contrast. Initially, some of the intra-sheet links in the graphene were darker, but became lighter as the sample was slid to the right of the tip (Figure 7.6a-b). As the graphene sheet pivoted around the tip, the contrast weakened. However, as the substrate was retracted from the tip, the contrast in the structure became stronger (Figure 7.6c). This points to the minor changes in the thickness of the edge of the graphene sheet during sliding, and the graphitic nanocrystals moving in and out of strong diffraction conditions as they tilt when the sample was moved. The folding and unfolding was more pronounced in the suspended graphene sheet, which was located between the aggregate attached to the tip and the graphene sheets that were secured to the Si substrate. As the sample slid past the tip, we see the folded graphene sheets, depicted by the strong contrast regions, unfold and also stretch in the direction that the substrate was traveling (Figure 7.6e-f). In this example, we also saw that the many of the smaller localized graphitic nanocrystals did not change during the folding and unfolding, consistent with the observations from the previous example.

In the third example (Figure 7.7 and Video S4), two needle-like nanocrystals, which formed the edges of a graphene sheet, were moving as the sample was sliding. The graphene sheet supported by the two needle-like graphitic nanocrystals collapsed as they moved closer together, and returned to its original configuration as the nanocrystals moved apart. This structural change was reversible. As the graphitic nanocrystals were in contact with the tip, we also observed changes in the contrast within the structure, suggesting that nanocrystals were rotating and tilting as they came in contact with the tip. This observation provides further evidence that both intra-sheet links and graphitic nanocrystals add rigidity to the graphene sheets.

The intra-sheet links that formed at crumpled regions can be compared to pivot points that facilitate the folding and unfolding of individual graphene sheets. During the folding and unfolding process (Video S2), intra-sheet links, which corresponded to the edges of the sheet, began bending the sheet onto itself. Eventually, the sheet collapsed as it passed the tip. As the graphene sheet moved farther away from the tip, the fold was relaxed and the crumpled

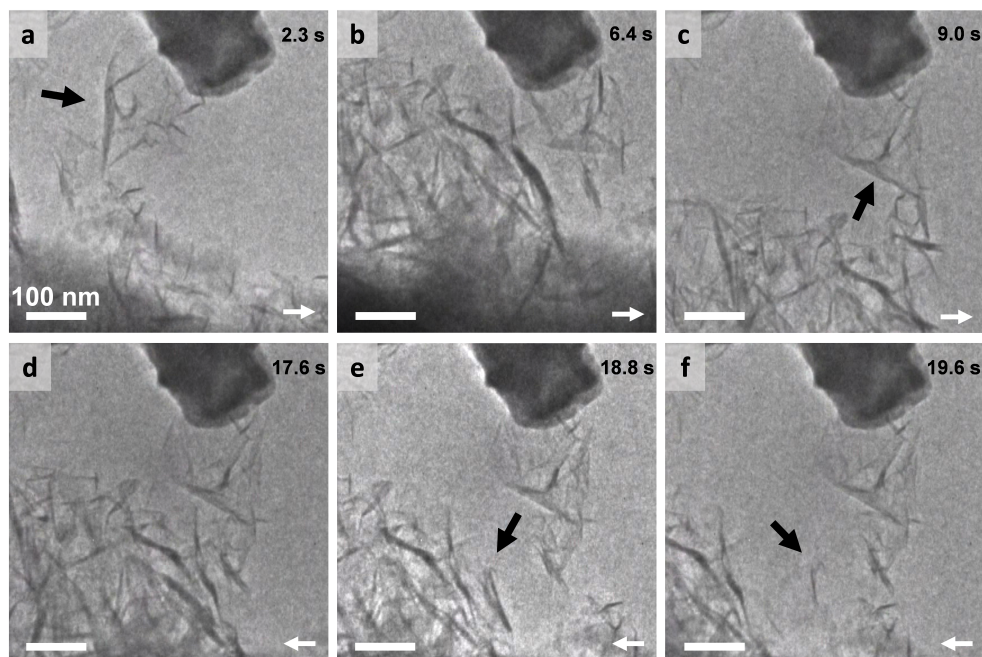


Figure 7.6. (a-c) As the sample is moving to the right, graphitic nanocrystals, indicated by the black arrows in (a) and (c), have minimal changes in contrast under this sliding condition. This suggests that there are no significant structural changes except for some minimal rotation about the tip. (d-f) As the sample moved to the left, a suspended intra-sheet link, indicated by the black arrows, almost unfolded completely. The localized intra-sheet link, which appeared very dark in (e), almost completely vanished in (f). White arrows indicate the sample's direction of travel.

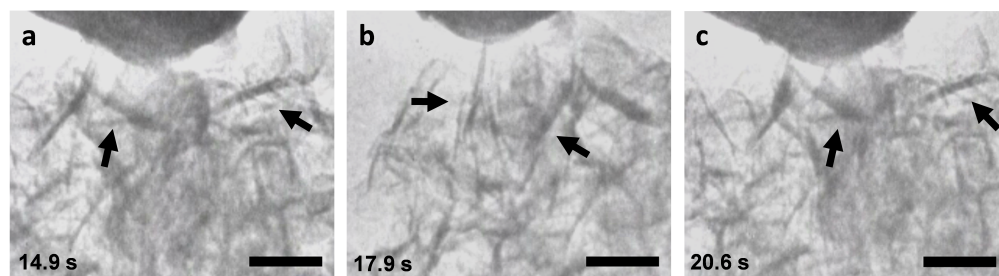


Figure 7.7. (a-c) Needle-like graphitic nanocrystals, indicated by arrows, acted as support for the graphene sheets. The nanocrystals converged as the sample slid toward the tip, and returned to their original configuration as the sample passed the tip. The interaction between the graphitic nanocrystals and the AFM tip collapsed the crumpled sheet. The sample is travelling from left to right in this sequence. Scale bars, 100 nm.

sheet returned to the unfolded state, albeit with slight changes in morphology. Note that the graphitic nanocrystals supporting the graphene sheet mostly maintained their structure during sliding; however, we discerned a slight change in position as the graphene sheet folded

and unfolded. This is the result of the reorientation of graphitic nanocrystals in the electron beam when the force was aligned longitudinally to the direction of atomic planes, allowing them to move. The change in TEM image contrast of the graphitic nanocrystal is not an indication of morphological change but rather a reorientation in the electron beam, as the nanocrystal did not vanish as previously observed in intra-sheet links (Figure 7.6e-f). The nanocrystals returned to their original positions relative to the graphene sheet, after the entire sheet slid past the tip and unfolded. From these observations, we find that the intra-sheet links formed by the crumpled regions are more elastic, but the graphitic nanocrystals are more rigid as they do not change structurally.

In densely packed solids such as crumpled paper balls or crumpled foils, the folds and crumples impart resistance to small compressive and shear forces [283, 289, 291, 292, 295, 296]. One can “smooth out” the crumples by applying tensile forces to the edges of the sheet. The experimentally observed folding and unfolding behavior of the crumpled graphene is similar to smoothing out crumpled paper, but there are inconsistencies, as previously suggested in molecular dynamics simulations [279]. Each individual graphene sheet has intrinsic intra-sheet links located where the crumples were formed. These ‘minor’ intra-sheet links allowed the sheets to fold and unfold when they were in contact with the AFM tip. In addition to this there is rigidity in the needle-like graphitic nanocrystals. While intra-sheet links with two to three folded layers of graphene exhibited elastic behavior, the graphitic nanocrystals are more rigid as they do not readily change. In most cases, the sliding imparts a force parallel to the sliding direction, limiting unfolding as the bending stiffness along that direction (graphitic plane direction) is high. When the applied force is longitudinal to the atomic plane, then nanocrystals reorient in the electron beam via tilt and rotation, resulting in changes in image contrast.

7.4 Conclusions

In summary, we report that the substrate-free gas-phase synthesis method is capable of producing aggregation-resistant crumpled graphene that contains intra-sheet links and graphitic nanocrystals. These graphitic structures behaved similarly to staples in crumpled graphene as they increased the rigidity and structural stability of graphene sheets, as revealed by *in situ* sliding experiments in the TEM. We have demonstrated that direct observations using *in situ* TEM is a powerful experimental approach for elucidating the nanoscale mechanical behavior of crumpled graphene. Additionally, graphitic staples in crumpled graphene could be used as a model system to tune the mechanical properties of other thin nanomaterials for tribological applications.

Modeling Electromechanical Couplings at Nanoscale Contacts

8.1 Introduction

In this chapter, I will present a recently developed model that combines classical contact mechanics with the flexoelectric effect to explain the thermodynamic driver for charge separation and charge transfer. This model will help understand the complex electromechanical couplings at nanoscale contacts, allowing us to estimate the mechanically induced polarizations to the first order across various material interfaces including polymers and ceramics. By quantifying the flexoelectric contributions at contacting surfaces, one may be able to design surfaces to maximize the potential differences in applications such as energy harvesters or to regulate these potential differences such as in biomimetic materials. The work in this chapter was completed in collaboration with Christopher Mizzi at Northwestern University and has been published in the journal *Physical Review Letters* (see reference [297]).

The triboelectric effect, which defined as the transfer of charge associated with rubbing or contacting two materials, has been known for at least thousands of years [298, 299]. The consequences of this transfer are known to be beneficial and detrimental; for instance, tribocharging is widely exploited in technologies such as laser printers and energy harvesters but can also cause electrostatic discharges that lead to fires or electronic equipment malfunction. It is accepted that it involves the transfer of charged species, either electrons [300–302], ions [303, 304], or charged molecular fragments [305], between two materials. The nature and identification of these charged species has been the focus of considerable research [299, 306], but an important unresolved issue is the thermodynamic driver for charge transfer; the process of separating and transferring charge must reduce the free energy of the system. Triboelectric charge transfer in insulators is not well-understood; proposed models include local heating [307] and trapped charge tunneling [308–310] but these models do not explicitly

address the significant mechanical deformations associated with bringing two materials into contact and rubbing them together.

Since the pioneering work of Bowden and Tabor [311] it has been known that friction and wear at the nanoscale is associated with the elastic and plastic deformations of many nanoscale asperities and the adhesion between. It is also well established that elastic deformation is thermodynamically linked to polarization: the linear coupling between strain and polarization is the piezoelectric effect and the linear coupling between strain gradient and polarization is the flexoelectric effect [312–314]. While piezoelectricity is well-known form of electromechanical coupling, they only occur for crystallographies which do not have an inversion center. In contrast, flexoelectric effects occur in all insulators independent of the crystallography. The coupling is a fourth-order tensor which can conveniently be scaled by the dielectric coefficient; this is known as the flexocoupling voltage. For many materials flexocoupling voltages are in the range of 1-10 V, although there are cases where it is significantly larger, for instance ~ 40 V for DyScO_3 [315]. Both the sign and the magnitude of the flexocoupling voltage in a given material can depend strongly upon the crystallographic orientation [314], and a few experimental values are given in Table 8.1. Furthermore, flexoelectric contributions can be large at the nanoscale due to the intrinsic size scaling of strain gradients [314–316]. Quite a few papers have analyzed the implications of these coupling terms in phenomena including nanoindentation [317, 318], fracture [319], and tunneling [320]. There also exists literature where the consequences of charging on friction have been studied [321–323], and frictional properties have been related to redistributions of interfacial charge density via first principles calculations [324]. However, triboelectricity, flexoelectricity, and friction during sliding are typically considered as three independent phenomena.

In this chapter, we hypothesize that the electric fields induced by inhomogeneous deformations at local asperities via the flexoelectric effect lead to significant surface potentials differences, which can act as the driver for triboelectric charge separation and transfer. The

Table 8.1. Examples of flexoelectric coefficient and flexocoupling voltage measurements for both oxides and polymers in the literature. Polymer measurements do not have specified signs, so f is treated as $|f|$ for those materials.

Reference	Material	μ (nC/m)	f (V)
[325]	SrTiO ₃ [001]	6.1	2.3
[325]	SrTiO ₃ [101]	-5.1	-1.9
[325]	SrTiO ₃ [111]	-2.4	-0.9
[315]	DyScO ₃ [110]	-8.4	-42
[326]	PVDF	13	160
[326]	Oriented PET	9.9	289
[326]	Polyethylene μm	5.8	273
[326]	Epoxy	2.9	84

flexoelectric effect may therefore be a very significant, and perhaps even the dominant, thermodynamic driver underlying triboelectric phenomena in many cases. To investigate this hypothesis in detail we analyze, within the conventional Hertzian [11] and Johnson-Kendall-Roberts (JKR) [12] contact models, the typical surface potential differences around an asperity in contact with a surface during indentation and pull-off. We find that surface potential differences in the range of ± 1 -10 V or more can be readily induced for typical polymers and ceramics at the nanoscale, and that the intrinsic asymmetry of the inhomogeneous strains during indentation and pull-off changes the sign of the surface potential difference.

8.2 Results

Nanoscale asperity contact consists of two main phenomena, indentation and pull-off, which are illustrated in Figure 8.1. To investigate the electric fields arising from the strain gradients associated with these two processes, we combine the constitutive flexoelectric equations with the classic Hertzian and JKR models, considering only vertical relative displacements for simplicity. The normal component of the electric field induced by a flexoelectric coupling in an isotropic non-piezoelectric half plane oriented normal to \hat{z} is given by in Equation 8.1:

$$E_z = -f \frac{\partial \epsilon}{\partial z} \Big|_{eff} = -f (3\epsilon_{zzz} + \epsilon_{zxx} + \epsilon_{xzx} + \epsilon_{xxz} + \epsilon_{zyy} + \epsilon_{yzy} + \epsilon_{yyz}) \quad (8.1)$$

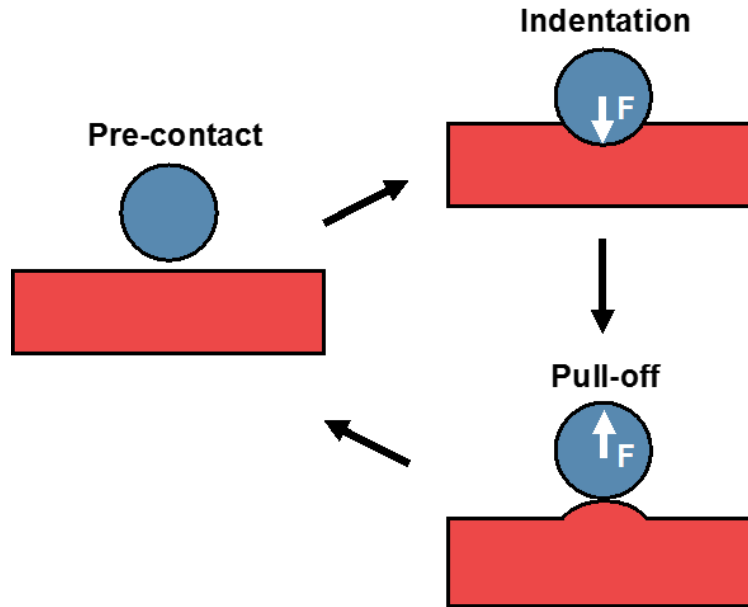


Figure 8.1. Schematic of asperity contact between a rigid sphere (shown in blue) and an elastic body (shown in red). The elastic body will deform during both indentation and pull-off, resulting in a net strain gradient opposite to the direction of the applied force (F).

Where E_z is the electric field linearly induced by $\frac{\partial \epsilon}{\partial z}|_{eff}$ the effective strain gradient. The proportionality constant f is the flexocoupling voltage (the flexoelectric coefficient divided by the dielectric constant) and the effective strain gradient is the sum of the symmetry-allowed strain gradient components (where $\epsilon_{jkl} = \partial \epsilon_{jk} / \partial x_l$).

First, we will analyze the indentation case. Because of the axial symmetry assumptions of the Hertzian contact theory, only five strain gradient components in Equation 8.1 are symmetrically inequivalent during indentation. The strain gradient components can be visualized as contour plots, shown in Figure 8.2. From these plots it is evident that the strain gradient components have complex spatial distributions, the details of which depend on the materials properties of the deformed body (Young's modulus, Poisson's ratio) as well as external parameters (applied force, indenter size). Further insight can be gained by calculating the average effective strain gradient within the indentation volume, which is taken to be the cube of the deformation radius. The average effective strain gradient is negative and scales inversely with indenter size, independent of the materials properties of

the deformed body and the applied force. The former is intuitive since a material deformed by an indenter should develop a curvature opposite to the direction of the applied force, and the latter is a consequence of averaging. Recall the effective strain gradient in Equation 8.1 linearly induces an electric field via the flexoelectric effect. It is comprised of a number of strain gradient components, each with complex spatial distributions. Therefore, to get a sense of the overall magnitude and impact of the effective strain gradient, it is convenient to average it. A natural choice of integration volume is the deformation volume defined as a^3 , where a is the deformation radius:

$$\overline{\frac{\partial \epsilon}{\partial z}} \Big|_{eff} = \frac{1}{a^3} \int \frac{\partial \epsilon}{\partial z} \Big|_{eff} \quad (8.2)$$

This is particularly convenient because for indentation, $\frac{\partial \epsilon}{\partial z} \Big|_{eff}$ is a function of materials parameters and the applied force via a . Similarly, for pull-off $\frac{\partial \epsilon}{\partial z} \Big|_{eff}$ is a function of materials parameters via a . Therefore, averaging over the deformation volume effectively removes all dependences except for the indenter radius. This is confirmed numerically. Moreover, since

$$E_z = -f \frac{\partial \epsilon}{\partial z} \Big|_{eff} \quad (8.3)$$

and f is a constant, it follows that an average electric field can be defined as

$$\bar{E}_z = -f \overline{\frac{\partial \epsilon}{\partial z}} \Big|_{eff} \quad (8.4)$$

which is also independent of materials properties and applied parameters except the indenter size. As shown in Figure 8.2f, the average effective strain gradient associated with Hertzian indentation is on the order of -10^8 m^{-1} in all materials at the nanoscale. Such large strain gradients immediately suggest the importance of flexoelectric couplings [314, 315].

For pull-off we use JKR theory, which incorporates adhesion effects between a spherical indenter and an elastic half-space into the Hertz contact model. The tensile force required

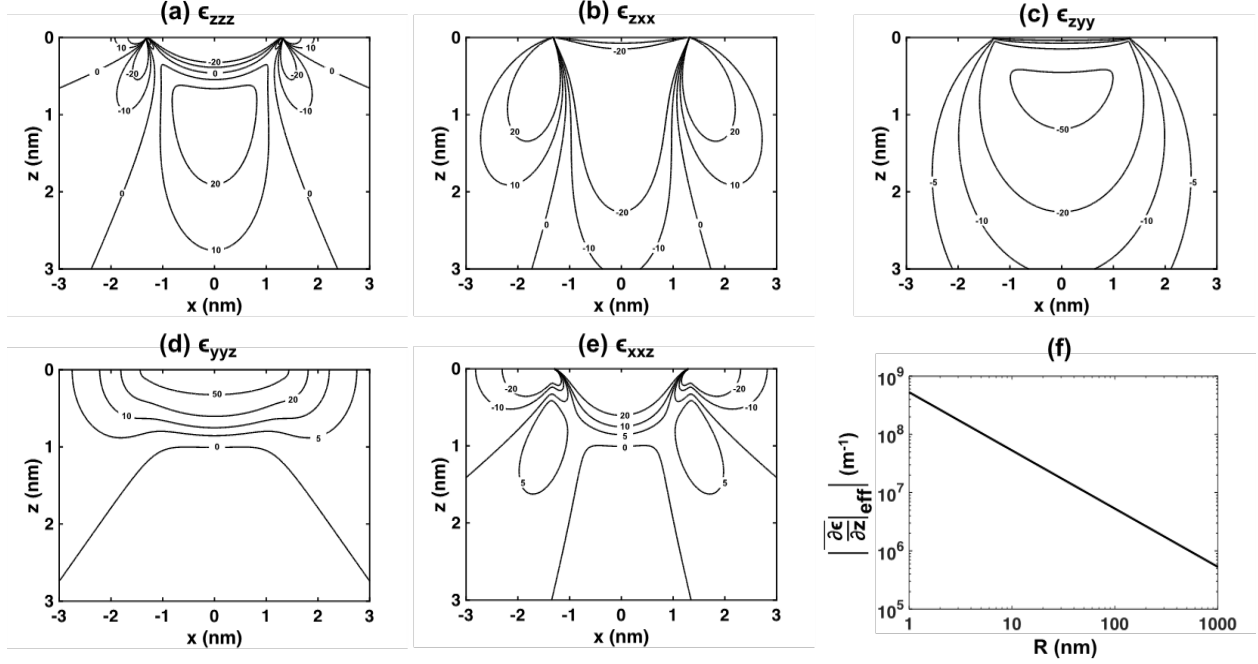


Figure 8.2. (a-e) There are 5 symmetrically inequivalent strain gradients that arise from Hertzian indentation of an elastic half-space that can flexoelectrically couple to the normal component of the electric field. Contour lines indicate the constant value of the strain gradient in units of 10^6 m^{-1} , z is the direction normal to the surface with positive values going into the bulk, and x is the in-plane direction. The origin is at the central point of contact. (f) The magnitude of the average effective strain gradient $|\frac{\partial \epsilon}{\partial z}|_{eff}$ as a function of indenter radius (R). The average effective strain gradient is the sum of the all the strain components shown (a-e) averaged over the indentation/pull-off volumes.

to separate the indenter from the surface, also known as the pull-off force, can be written as

$$F_{adh} = -\frac{3}{2}\pi\Delta\gamma R \quad (8.5)$$

where $\Delta\gamma$ is the adhesive energy per unit area and R is the radius of the spherical indenter. Replacing the applied force in the Hertzian indentation strain gradient expressions with this force yields pull-off strain gradients immediately before contact is broken. This analysis for the pull-off case yields strain gradient distributions qualitatively similar to those shown in Figure 8.2, except with opposite signs because the force is applied in the opposite direction.

Importantly, as in the indentation case, the average effective strain gradient within the pull-off volume scales inversely with indenter size, is independent of the materials properties of the deformed body, and is on the order of 10^8 m^{-1} in all materials at the nanoscale.

After understanding the strain gradient distributions and the flexoelectric response at asperity deformations, we now turn to quantifying these responses. Obtaining analytical expressions for the normal component of the electric field in the deformed body induced by indentation and pull-off involves substituting the strain gradient components shown in Figure 8.2 into Equation 8.1. This electric field component is shown in Figure 8.3 for the indentation case with a positive flexocoupling voltage. The pull-off case is similar, but the signs of the electric fields are reversed. Since the electric field induced by the flexoelectric effect is the effective strain gradient scaled by the flexocoupling voltage, its magnitude is linearly proportional to the flexocoupling voltage and inversely proportional to the indenter size. The average electric field within the indentation/pull-off volume is on the order of 10^8 - 10^9 V/m for all materials at the nanoscale assuming a conservative flexocoupling voltage of 1 V [313, 314, 327]; some specific flexocoupling voltages are given in Table 8.1.

The electric fields induced by the flexoelectric effect in the bulk of the deformed body will generate a potential on its surface. Figure 8.4 depicts the surface potential difference calculated from the normal component of the electric field along the deformed surface of a typical polymer with a flexocoupling voltage of 10 V [313, 314, 327]. We note that the available measured flexocoupling voltages for polymers indicates that this may be underestimated, as many literature values significantly exceed 10 V. The pull-off surface potential difference tends to be larger in magnitude and spatial extent than the indentation surface potential difference. In both cases the magnitude of the maximum surface potential difference is sensitive to the materials properties of the deformed body (Young's modulus, Poisson's ratio, adhesion energy, flexocoupling voltage) and external parameters (applied force, indenter size).

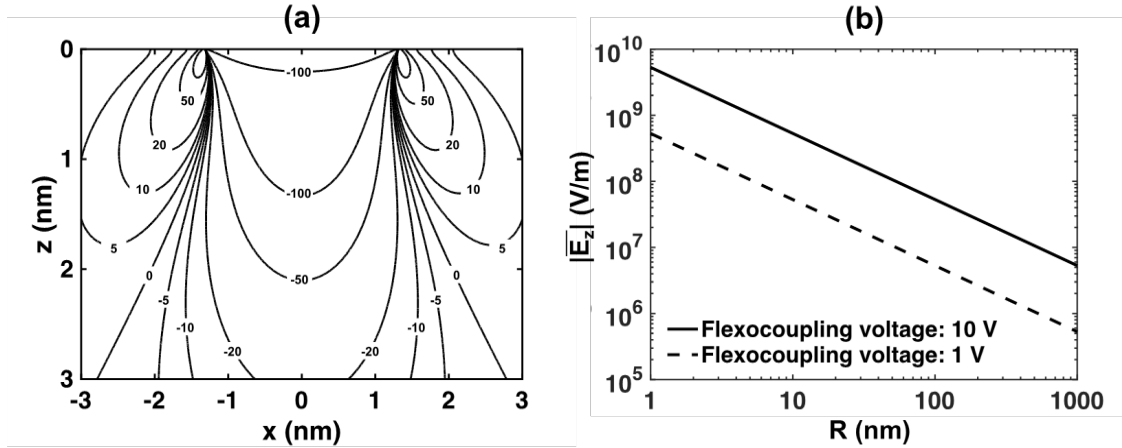


Figure 8.3. (a) Normal component of the electric field induced by Hertzian indentation via a flexoelectric coupling. Contour lines indicate electric field in units of MV/m, z is the direction normal to the surface with positive values going into the bulk, and x is the in-plane direction. The origin is the central point of contact. (b) Magnitude of the average electric field ($|\bar{E}_z|$) in the indentation/pull-off volumes (at asperities) as a function of indenter radius (R) for flexocoupling voltages of 1 V and 10 V.

Specifically, the surface potential differences for indentation and pull-off scale as:

$$V_{\text{indentation,min}} \propto f \left(\frac{F}{R^2 Y} \right)^{1/3} \quad (8.6)$$

$$V_{\text{pull-off,max}} \propto f \left(\frac{\Delta\gamma}{R Y} \right)^{1/3} \quad (8.7)$$

Where $V_{\text{indentation,min}}$ is the minimum surface potential difference for indentation, $V_{\text{pull-off,max}}$ is the maximum surface potential difference for pull-off, f is the flexocoupling voltage, F is the applied force, R is the indenter radius, Y is the Young's modulus, and $\Delta\gamma$ is the energy of adhesion.

The above analysis indicates that large strain gradients arising from deformations by nanoscale asperities yield surface potential differences via a flexoelectric coupling in the ± 1 -10 V range, as a conservative estimate. The magnitude of this surface potential difference is sufficient to drive charge transfer, suggesting that flexoelectric couplings during indentation and pull-off can be responsible for triboelectric charging. Furthermore, this model implies

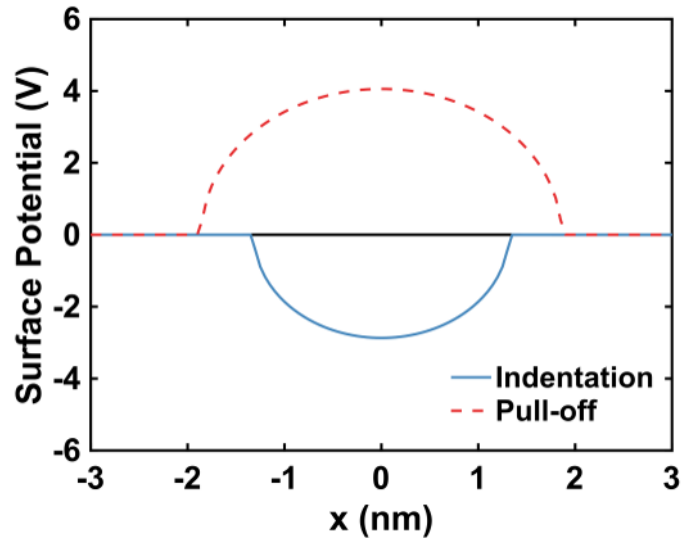


Figure 8.4. Electric potential difference along the surface of the deformed body for indentation (blue solid line) and pull-off (red dashed line). The x axis represents the in-plane direction and the origin is the central point of contact.

that the direction of charge transfer is controlled by a combination of the direction of the applied force and local topography (whether the asperity indenting or pulling-off), as well as the sign of the flexocoupling voltage.

8.3 Discussion and Conclusions

Our model is consistent with a range of experimental observations. First, it has been observed that tribocurrents exhibit bipolar characteristics associated with stick-slip [328]. This bipolar nature is consistent with the change in the sign of the surface potential difference for indentation and pull-off predicted by our model. We note that these experiments had some shear component which is not exactly the same as our analysis and complicates the problem due to the breakdown of circular symmetry. While this will yield a more complex strain gradient distribution than our simplified model, the total potential difference will be the sum of normal and shear contributions which does not alter our general conclusions. Second, the measured tribocurrent has been shown to scale with the indentation force to the power of $\frac{1}{3}$ [329], which matches the scaling of the indentation surface potential difference

with force. Thirdly, charging between similar materials [330–333] and the formation of non-uniform tribocharge patterns [334–337] can be explained by considering the effect of local surface topography and crystallography on the direction of charge transfer. For instance, local variation in surface topography determines which material locally acts as the asperity, and consequently dictate the direction in which charge transfers. In addition, it is established for crystalline materials that both the magnitude and sign of the flexocoupling voltage can change with crystallographic orientation (see Table 8.1). Finally, recent work has demonstrated that macroscopic curvature biases tribocharging so that convex samples tend to charge negative and concave samples tend to charge positive; this coupling between curvature and charge transfer direction is a natural consequence of our flexoelectric model [338].

In addition to the above qualitative conclusions, it is relevant to explore whether flexoelectricity can quantitatively explain experimental triboelectric charge transfer measurements. An important quantitative parameter in the triboelectric literature is the magnitude of triboelectric surface charge density which has been measured in a number of systems including spherical particles [333, 339] and patterned triboelectric devices [340, 341], and normally enters models as an empirical parameter [342, 343]. We hypothesize that the upper bound for the triboelectric surface charge density is set by the flexoelectric polarization, i.e. charge will transfer until the flexoelectric polarization is screened. As shown in Table 8.2, this hypothesis agrees with existing tribocharge measurements on a wide range of length scales to within an order of magnitude without invoking anomalous flexoelectric coefficients and other adjustable parameters.

Table 8.2. Comparison between measure triboelectric surface charge (σ_{tribo}) and calculated flexoelectric polarization (P_{FxE}) for feature sizes in the mm to μm range assuming a flexoelectric coefficient of 1 nC/m.

Reference	Feature size	σ_{tribo} ($\mu\text{C}/\text{m}^2$)	P_{FxE} ($\mu\text{C}/\text{m}^2$)
[339]	2.3 mm	0.5	0.4
[333]	326 μm	0.2	1.6
[333]	251 μm	0.5	2.1
[340, 341]	10 μm	97.4	106.1

These results make a strong case that the flexoelectric effect drives triboelectric charge separation and transfer, and that nanoscale friction, flexoelectricity, and triboelectricity occur simultaneously and are linked. In summary, the macroscopic forces during sliding on insulators cause local inhomogeneous strains at contacting nanoscale asperities which induce significant local electric fields, which in turn, drive charge separation.

8.4 Future Opportunities

The model presented in this chapter is not only limited to inorganic materials, but is quite general. As one extension it is known that semi-crystalline layers are formed at the confined spaces during sliding in a lubricant [344], so it is not unreasonable that flexoelectric effects can drive charge separation in lubricants. Another extension to this is biological materials, as flexoelectric effects in biological membranes [345] and biominerals [346] are well-established. Recent experimental work suggests that flexoelectricity in hydroxyapatite induces sufficient electric potential for programmed cell death and bone remodeling [346]. We also note the magnitude of the flexoelectricity-induced electric fields and surface potential differences at asperities (and crack tips [319]) suggest flexoelectricity can play a role in triboluminescence [347–349], triboplasma generation [350] or tribochemical reactions. Such hypotheses merit additional work.

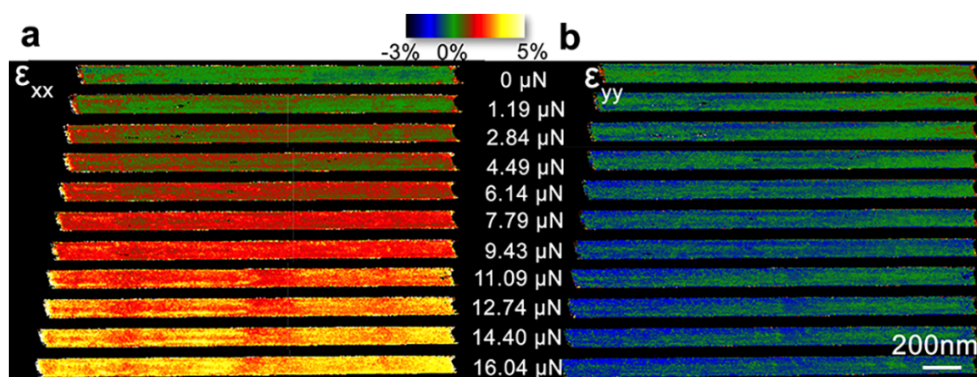


Figure 8.5. Strain distribution within core-shell InAs nanowires under tensile stress is observed by STEM combined with nanobeam electron diffraction. Adapted from [258].

As a final note, one of the limiting factors of flexoelectric effect is the lack of flexocoupling voltages and flexoelectric coefficients in the literature. Establishing a library of these values for common insulators, both polymers and ceramics, via an established three-point bending measurement technique, can lead to more relevant estimates of the flexoelectric contribution at nanoscale contacts. Lastly, experimental validation of the flexoelectric polarizations at deforming surfaces can be completed with an *in situ* TEM. *In situ* straining, mechanical measurement, and electrical characterization have been recently combined to characterize electromechanical couplings such as piezoresistive and piezoelectric effects in nanowires [258]. To investigate the correlation between mechanical strain and the electrical transport properties, a nanoindenter TEM holder with an electrical push-to-pull microelectromechanical system device can be used for the *in situ* studies. By combining this approach with strain mapping analysis based on STEM with nanobeam electron diffraction, strain inhomogeneities including localized strain gradients can then be measured (Figure 8.5). Consequently, the flexoelectric contributions of a material and its defects under different mechanical stimuli can be quantified by directly correlating strain gradients with *in situ* electrical responses.

CHAPTER 9

Conclusions**9.1 Oxidation and Corrosion**

In summary, the early-stage oxidation and corrosion of CoCrMo and NiCrMo alloys were characterized by transmission electron microscopy. Extensive analysis of the crystallography and chemistry of nanoscale oxide layers revealed several cases of nonequilibrium solute capture. The investigation of early-stage oxidation of CoCrMo alloys at a moderate temperature revealed that grain boundaries play a role in assisting the formation of oxides that contain solute capture. Rapid diffusion at grain boundaries formed defective oxide layers that allowed cation diffusion to continue at a fast rate, resulting in spinel oxides with Cr concentrations that exceed the thermodynamic limits. Another study on the aqueous corrosion of CoCrMo alloys in Cl^- solutions showed that the oxide layer had predominantly rocksalt crystallography and contained a significant amount of Cr, greatly exceeding the thermodynamic solubility of Cr in rocksalt CoO. In contrast, CoCrMo alloys corroded in model synovial fluids containing hyaluronic acid, which has been found to lower the corrosion resistance of CoCrMo alloys, do not contain solute capture. This suggested that a secondary mechanism was dominant: hyaluronic acid formed metal complexes during anodization, resulting in Cr depletion and non-protective oxide islands on the alloy surface. Lastly, a cryo-transmission electron microscopy observation of aqueous corrosion in NiCrMo alloys revealed the presence of rocksalt and polycrystalline $\text{Ni}_{1-x}\text{Cr}_{2x/3}(\text{OH})_2$ on the surface of the corroded NiCrMo, supporting that these phases were formed onto the alloy during corrosion in a Cl^- -containing solution. Despite the successful preservation of the surface through cryogenic sample preparation and analysis, it is still an open question whether the hydroxide phase is purely nickel hydroxide or whether it incorporates Cr and/or Mo. This merits more detailed studies with more advanced methods in future work.

9.2 Tribology and Triboelectricity

Turning to tribology, mechanical deformations of crumpled graphene, which consisted of flexible intra-sheet links and rigid nanocrystals, were observed with *in situ* transmission electron microscopy. The nanomechanical behaviors of intra-sheet links and graphitic nanocrystals showed the origins of enhanced mechanical stability and wear resistance of crumpled graphene. A theoretical model combined contact mechanics and flexoelectricity to model the electromechanical couplings at nanoscale contacts. This study established that the macroscopic forces during sliding on insulators caused local inhomogeneous strains at contacting nanoscale asperities, which induced significant local electric fields, driving charge separation. These findings indicate that the link between flexoelectricity and triboelectricity is important for understanding the complex nature of localized electrical properties at nanoscale asperities and can lead to the better designs of surfaces to be tailored for specific applications. Additionally, the versatile *in situ* TEM approach can be combined with more advanced characterization tools to relate mechanical strain with the electrical transport properties of materials. This opens doors for future opportunities to quantify the flexoelectric contributions of a material and its defects under different mechanical stimuli by directly correlating strain gradients with *in situ* electrical responses.

Bibliography

1. Dowson, D. *History of tribology* 2nd Ed. (Professional Engineering Publishing, London, 1998).
2. Donaldson, J. A. The use of gold in dentistry - an historical overview, part I. *Gold Bulletin* **13**, 117–124 (1980).
3. Mathew, M. T., Srinivasa Pai, P., Pourzal, R., Fischer, A. & Wimmer, M. A. Significance of Tribocorrosion in Biomedical Applications: Overview and Current Status. *Advances in Tribology* **2009**, 1–12 (2009).
4. Jost, H. P. Tribology - Origin and future. *Wear* **136**, 1–17 (1990).
5. Holmberg, K. & Erdemir, A. Influence of tribology on global energy consumption, costs and emissions. *Friction* **5**, 263–284 (2017).
6. Koch, G. H., Brongers, M. P. H., Thompson, N. G., Virmani, Y. P. & Payer, J. H. *Corrosion Costs and Preventative Strategies in the United States* tech. rep. (FHWA-RD-01-156, NACE International, 2016).
7. Bhushan, B. Contact Mechanics of Rough Surfaces in Tribology: Single Asperity Contact. *Applied Mechanics Reviews* **49**, 275–298 (1996).
8. Williams, J. *Engineering tribology* 3rd Ed. (Cambridge University Press, New York, 2005).
9. Bhushan, B. Contact mechanics of rough surfaces in tribology: multiple asperity contact. *Tribology Letters* **4**, 1–35 (1998).
10. Archard, J. F. Contact and rubbing of flat surfaces. *Journal of Applied Physics* **24**, 981–988 (1953).
11. Hertz, H. Über die Berührung fester elastischer Körper. *Journal für die Reine und Angewandte Mathematik* **1882**, 156–171 (1882).
12. Johnson, K. L., Kendall, K. & Roberts, A. D. Surface Energy and Contact of Elastic Solids. *Proceedings of the Royal Society of London A* **324**, 301–313 (1971).

13. Johnson, K. L. Mechanics of adhesion. *Tribology International* **31**, 413–418 (1998).
14. Maugis, D. Adhesion of spheres: The JKR-DMT transition using a dugdale model. *Journal of Colloid and Interface Science* **150**, 243–269 (1992).
15. Bowden, F. P., Moore, A. J. W. & Tabor, D. The ploughing and adhesion of sliding metals. *Journal of Applied Physics* **14**, 80–91 (1943).
16. Marks, L. D., Warren, O. L., Minor, A. M. & Merkle, A. R. Tribology in full view. *MRS Bulletin* **33**, 1168–1173 (2008).
17. Wimmer, M., Sprecher, C., Hauert, R., Täger, G. & Fischer, A. Tribochemical reaction on metal-on-metal hip joint bearings. *Wear* **255**, 1007–1014 (2003).
18. Wimmer, M. A. *et al.* Wear mechanisms in metal-on-metal bearings: The importance of tribochemical reaction layers. *Journal of Orthopaedic Research* **28**, 436–443 (2010).
19. Carpick, R. W. & Salmeron, M. Scratching the surface: Fundamental investigations of tribology with atomic force microscopy. *Chemical Reviews* **97**, 1163–1194 (1997).
20. Martin, J. M., Le Mogne, T., Boehm, M. & Grossiord, C. Tribochemistry in the analytical UHV tribometer. *Tribology International* **32**, 617–626 (1999).
21. Pourbaix, M. *Atlas of Electrochemical Equilibria in Aqueous Solutions* 2nd Ed. (English) (National Association of Corrosion Engineers, 1974).
22. Beverskog, B. & Puigdomenech, I. Pourbaix diagrams for the ternary system of iron-chromium-nickel. *Corrosion* **55**, 1077–1087 (1999).
23. Kirchheim, R. *et al.* The passivity of iron-chromium alloys. *Corrosion Science* **29**, 899–917 (1989).
24. Zhang, L. & Macdonald, D. D. Segregation of alloying elements in passive systems—I. XPS studies on the Ni-W system. *Electrochimica Acta* **43**, 2661–2671 (1998).
25. Castle, J. E. & Mann, G. M. The mechanism of formation of a porous oxide film on steel. *Corrosion Science* **6**, 253–262 (1966).
26. Hashimoto, K., Asami, K., Kawashima, A., Habazaki, H. & Akiyama, E. The role of corrosion-resistant alloying elements in passivity. *Corrosion Science* **49**, 42–52 (2007).

27. Cabrera, N. & Mott, N. F. Theory of the oxidation of metals. *Reports on Progress in Physics* **12**, 163–184 (1949).
28. Macdonald, D. D. The Point Defect Model for the Passive State. *Journal of The Electrochemical Society* **139**, 3434–3449 (1992).
29. Lin, L. F., Chao, C. Y. & Macdonald, D. D. A Point Defect Model for Anodic Passive Films: II. Chemical Breakdown and Pit Initiation. *Journal of The Electrochemical Society* **128**, 1194–1198 (1981).
30. Chao, C. Y. A Point Defect Model for Anodic Passive Films. *Journal of The Electrochemical Society* **128**, 1187–1194 (1981).
31. Olefjord, I. & Elfstrom, B.-O. The Composition of the Surface during Passivation of Stainless Steels. *Corrosion* **38**, 46–52 (1982).
32. Olefjord, I. Surface Composition of Stainless Steels during Anodic Dissolution and Passivation Studied by ESCA. *Journal of The Electrochemical Society* **132**, 2854–2861 (1985).
33. Marks, L. Competitive chloride chemisorption disrupts hydrogen bonding networks: DFT, crystallography, thermodynamics, and morphological consequences. *Corrosion* **74**, 295–311 (2018).
34. Yu, X.-X., Gulec, A., Cwalina, K. L., Scully, J. R. & Marks, L. D. New insights on the role of chloride during the onset of local corrosion: TEM, APT, surface energy, and morphological instability. *Corrosion* **75**, 616–627 (2019).
35. Olsson, C. O. A. The influence of nitrogen and molybdenum on passive films formed on the austenoferritic stainless steel 2205 studied by AES and XPS. *Corrosion Science* **37**, 467–479 (1995).
36. Dowling, N. J. E., Kim, Y. H., Ahn, S. K. & Lee, Y. D. Effect of alloying elements and residuals on corrosion resistance of type 444 stainless steel. *Corrosion* **55**, 187–199 (1999).

37. Lloyd, A. C., Noël, J. J., McIntyre, S. & Shoesmith, D. W. Cr, Mo and W alloying additions in Ni and their effect on passivity. *Electrochimica Acta* **49**, 3015–3027 (2004).
38. Hayes, J. R., Gray, J. J., Szmodis, A. W. & Orme, C. A. Influence of chromium and molybdenum on the corrosion of nickel-based alloys. *Corrosion* **62**, 491–500 (2006).
39. Mishra, A. K. & Shoesmith, D. W. Effect of alloying elements on crevice corrosion inhibition of nickel-Chromium-Molybdenum- Tungsten alloys under aggressive conditions: An electrochemical study. *Corrosion* **70**, 721–730 (2014).
40. Yu, X. X. *et al.* Nonequilibrium Solute Capture in Passivating Oxide Films. *Physical Review Letters* **121**, 145701 (2018).
41. Yu, X. X. *et al.* In situ observations of early stage oxidation of Ni-Cr and Ni-Cr-Mo alloys. *Corrosion* **74**, 939–946 (2018).
42. M’Ndange-Pfupfu, A., Ciston, J., Eryilmaz, O., Erdemir, A. & Marks, L. D. Direct observation of tribochemically assisted wear on diamond-like carbon thin films. *Tribology Letters* **49**, 351–356 (2013).
43. Smigelskas, A. D. and Kirkendall, E. O. Zinc Diffusion in Alpha Brass. *Transactions of AIME* **171**, 130–142 (1947).
44. Shewmon, P. G. & Bechtold, J. H. Marker movements in titanium-molybdenum diffusion couples and the Zener theory of Do. *Acta Metallurgica* **3**, 452–455 (1955).
45. Tu, K. Interdiffusion in Thin Films. *Annual Review of Materials Science* **15**, 147–176 (1985).
46. Sato, N. A theory for breakdown of anodic oxide films on metals. *Electrochimica Acta* **16**, 1683–1692 (1971).
47. Heuer, A., Kahn, H., Natishan, P., Martin, F. & Cross, L. Electrostrictive stresses and breakdown of thin passive films on stainless steel. *Electrochimica Acta* **58**, 157–160 (2011).
48. Radice, S., Liu, S., Pourzal, R., Laurent, M. P. & Wimmer, M. A. Effects of Bovine Serum Albumin and Hyaluronic Acid on the Electrochemical Response of a CoCrMo

- Alloy to Cathodic and Anodic Excursions. *Journal of Bio- and Tribo-Corrosion* **5**, 104 (2019).
49. Batson, P. E., Dellby, N. & Krivanek, O. L. Sub-ångstrom resolution using aberration corrected electron optics. *Nature* **418**, 617–620 (2002).
 50. Haider, M. *et al.* A spherical-aberration-corrected 200 kV transmission electron microscope. *Ultramicroscopy* **75**, 53–60 (1998).
 51. Hawkes, P. W. & Krivanek, O. L. In *Springer Handbook of Microscopy* (eds Hawkes, P. W. & Spence, J. C. H.) 625–679 (Springer International Publishing, 2019).
 52. Mate, C. M., McClelland, G. M., Erlandsson, R. & Chiang, S. Atomic-scale friction of a tungsten tip on a graphite surface. *Physical Review Letters* **59**, 1942–1945 (1987).
 53. Bennewitz, R. *et al.* Atomic-scale stick-slip processes on Cu(111). *Physical Review B* **60**, R11301–R11304 (1999).
 54. Dienwiebel, M. *et al.* Superlubricity of graphite. *Physical Review Letters* **92**, 126101 (2004).
 55. Dienwiebel, M., Pradeep, N., Verhoeven, G. S., Zandbergen, H. W. & Frenken, J. W. Model experiments of superlubricity of graphite. *Surface Science* **576**, 197–211 (2005).
 56. Hirano, M. & Shinjo, K. Superlubricity and frictional anisotropy. *Wear* **168**, 121–125 (1993).
 57. Sheehan, P. E. & Lieber, C. M. Nanotribology and Nanofabrication of MoO₃ Structures by Atomic Force Microscopy. *Science* **272**, 1158–1161 (1996).
 58. Sheehan, P. E. & Lieber, C. M. Friction between van der Waals Solids during Lattice Directed Sliding. *Nano Letters* **17**, 4116–4121 (2017).
 59. Gnecco, E. *et al.* Velocity dependence of atomic friction. *Physical Review Letters* **84**, 1172–1175 (2000).
 60. Bhushan, B. & Kwak, K. J. Velocity dependence of nanoscale wear in atomic force microscopy. *Applied Physics Letters* **91**, 163113 (2007).

61. Paolicelli, G., Tripathi, M., Corradini, V., Candini, A. & Valeri, S. Nanoscale frictional behavior of graphene on SiO₂ and Ni(111) substrates. *Nanotechnology* **26**, 055703 (2015).
62. Spear, J. C., Ewers, B. W. & Batteas, J. D. 2D-nanomaterials for controlling friction and wear at interfaces. *Nano Today* **10**, 301–314 (2015).
63. Jansen, L., Hölscher, H., Fuchs, H. & Schirmeisen, A. Temperature dependence of atomic-scale stick-slip friction. *Physical Review Letters* **104**, 256101 (2010).
64. Barel, I., Urbakh, M., Jansen, L. & Schirmeisen, A. Unexpected temperature and velocity dependencies of atomic-scale stick-slip friction. *Physical Review B* **84**, 115417 (2011).
65. Li, Q., Lee, C., Carpick, R. W. & Hone, J. Substrate effect on thickness-dependent friction on graphene. *Physica Status Solidi (B) Basic Research* **247**, 2909–2914 (2010).
66. Frisbie, C. D., Rozsnyai, L. F., Noy, A., Wrighton, M. S. & Lieber, C. M. Functional Group Imaging by Chemical Force Microscopy. *Science* **265**, 2071–2074 (1994).
67. McDevitt, N. T., Donley, M. S. & Zabinski, J. S. Utilization of Raman spectroscopy in tribochemistry studies. *Wear* **166**, 65–72 (1993).
68. Scharf, T. W. & Singer, I. L. Monitoring transfer films and friction instabilities with in situ Raman tribometry. *Tribology Letters* **14**, 3–8 (2003).
69. Cann, P. M. & Spikes, H. A. In lubro studies of lubricants in EHD contacts using FTIR absorption spectroscopy. *Tribology Transactions* **34**, 248–256 (1991).
70. Martin, J. M., Liang, H., Le Mogne, T. & Malroux, M. Low-temperature friction in the XPS analytical ultrahigh vacuum tribotester. *Tribology Letters* **14**, 25–31 (2003).
71. Gnecco, E., Bennewitz, R. & Meyer, E. Abrasive Wear on the Atomic Scale. *Physical Review Letters* **88**, 215501 (2002).
72. Bhaskaran, H. *et al.* Ultralow nanoscale wear through atom-by-atom attrition in silicon-containing diamond-like carbon. *Nature Nanotechnology* **5**, 181–185 (2010).

73. Gotsmann, B. & Lantz, M. A. Atomistic wear in a single asperity sliding contact. *Physical Review Letters* **101**, 125501 (2008).
74. Kizuka, T., Yamada, K., Deguchi, S., Naruse, M. & Tanaka, N. Cross-sectional time-resolved high-resolution transmission electron microscopy of atomic-scale contact and noncontact-type scannings on gold surfaces. *Physical Review B - Condensed Matter and Materials Physics* **55**, R7398–R7401 (1997).
75. Kizuka, T., Yamada, K., Deguchi, S., Naruse, M. & Tanaka, N. Time-resolved high-resolution electron microscopy of atomic scale solid-state direct bonding of gold tips. *Journal of Electron Microscopy* **46**, 151–160 (1997).
76. Kizuka, T., Tanaka, N., Deguchi, S. & Naruse, M. Time-Resolved High-Resolution Transmission Electron Microscopy Using a Piezo-Driving Specimen Holder for Atomic-Scale Mechanical Interaction. *Microscopy and Microanalysis* **4**, 218–225 (1998).
77. Anisimov, V. I., Zaanen, J. & Andersen, O. K. Band theory and Mott insulators: Hubbard U instead of Stoner I. *Physical Review B* **44**, 943–954 (1991).
78. Bengone, O., Bengone, O., Alouani, M., Blöchl, P. & Hugel, J. Implementation of the projector augmented-wave LDA+U method: Application to the electronic structure of NiO. *Physical Review B* **62**, 16392–16401 (2000).
79. Anisimov, V. I., Aryasetiawan, F. & Lichtenstein, A. I. First-principles calculations of the electronic structure and spectra of strongly correlated systems: the LDA + U method. *Journal of Physics: Condensed Matter* **9**, 767–808 (1997).
80. Tran, F., Blaha, P., Schwarz, K. & Novák, P. Hybrid exchange-correlation energy functionals for strongly correlated electrons: Applications to transition-metal monoxides. *Physical Review B* **74**, 155108 (2006).
81. Tran, F. *et al.* Force calculation for orbital-dependent potentials with FP-(L)APW + lo basis sets. *Computer Physics Communications* **179**, 784–790 (2008).
82. Novák, P., Kuneš, J., Chaput, L. & Pickett, W. E. Exact exchange for correlated electrons. *Physica Status Solidi (B) Basic Research* **243**, 563–572 (2006).

83. Blaha, P. *et al.* An augmented plane wave + local orbitals program for calculating crystal properties. *Technische Universitat Wien, Austria* (2018).
84. Blaha, P. *et al.* WIEN2k : An APW + lo program for calculating the properties of solids WIEN2k : An APW + lo program for calculating the properties of solids. *Journal of Chemical Physics* **152**, 074101 (2020).
85. Perdew, J. P., Burke, K. & Ernzerhof, M. Generalized gradient approximation made simple. *Physical Review Letters* **77**, 3865–3868 (1996).
86. Marks, L. D. Fixed-point optimization of atoms and density in DFT. *Journal of Chemical Theory and Computation* **9**, 2786–2800 (2013).
87. Brown, I. D. & Altermatt, D. Bond-valence parameters obtained from a systematic analysis of the Inorganic Crystal Structure Database. *Acta Crystallographica Section B Structural Science* **41**, 244–247 (1985).
88. Brown, I. D. Recent developments in the methods and applications of the bond valence model. *Chemical Reviews* **109**, 6858–6919 (2009).
89. Brown, I. D. *The chemical bond in inorganic chemistry: the bond valence model* 2nd Ed. (Oxford University Press, 2016).
90. Milošev, I. & Strehblow, H. H. The composition of the surface passive film formed on CoCrMo alloy in simulated physiological solution. *Electrochimica Acta* **48**, 2767–2774 (2003).
91. Hodgson, A. W. E. *et al.* Passive and transpassive behaviour of CoCrMo in simulated biological solutions. *Electrochimica Acta* **49**, 2167–2178 (2004).
92. Kocijan, A., Milošev, I. & Pihlar, B. Cobalt-based alloys for orthopaedic applications studied by electrochemical and XPS analysis. *Journal of Materials Science: Materials in Medicine* **15**, 643–650 (2004).
93. Lewis, A. C., Kilburn, M. R., Papageorgiou, I., Allen, G. C. & Case, C. P. Effect of synovial fluid, phosphate-buffered saline solution, and water on the dissolution and

- corrosion properties of CoCrMo alloys as used in orthopedic implants. *Journal of Biomedical Materials Research - Part A* **73**, 456–467 (2005).
94. Igual Muñoz, A., Schwiesau, J., Jolles, B. M. & Mischler, S. In vivo electrochemical corrosion study of a CoCrMo biomedical alloy in human synovial fluids. *Acta Biomaterialia* **21**, 228–236 (2015).
 95. Panigrahi, P. *et al.* Intergranular pitting corrosion of CoCrMo biomedical implant alloy. *Journal of Biomedical Materials Research - Part B Applied Biomaterials* **102**, 850–859 (2014).
 96. Bettini, E., Leygraf, C., Lin, C., Liu, P. & Pan, J. Influence of Grain Boundaries on Dissolution Behavior of a Biomedical CoCrMo Alloy: In-Situ Electrochemical-Optical, AFM and SEM/TEM Studies. *Journal of The Electrochemical Society* **159**, C422–C427 (2012).
 97. Valero-Vidal, C., Casabn-Julín, L., Herraiz-Cardona, I. & Igual-Muñoz, A. Influence of carbides and microstructure of CoCrMo alloys on their metallic dissolution resistance. *Materials Science and Engineering C* **33**, 4667–4676 (2013).
 98. Hoffman, E. E., Lin, A., Liao, Y. & Marks, L. D. Grain boundary assisted crevice corrosion in CoCrMo alloys. *Corrosion* **72**, 1445–1461 (2016).
 99. Lin, A., Hoffman, E. E. & Marks, L. D. Effects of Grain Boundary Misorientation and Chromium Segregation on Corrosion of CoCrMo Alloys. *Corrosion* **73**, 256–267 (2017).
 100. Phalnikar, C. A., Evans, E. B. & Baldwin, W. M. High Temperature Scaling of Cobalt-Chromium Alloys. *Journal of The Electrochemical Society* **103**, 429–438 (1956).
 101. Kofstad, P. K. & Hed, A. Z. High-Temperature Oxidation of Co-10 w/o Cr Alloys: I. Microstructure of Oxide Scales. *Journal of The Electrochemical Society* **116**, 224–229 (1969).
 102. Kofstad, P. K. & Hed, A. Z. High Temperature Oxidation of Co-10 w/o Cr Alloys: II. Oxidation Kinetics. *Journal of The Electrochemical Society* **116**, 229–234 (1969).

103. Stott, F. H., Wright, I. G., Hodgkiess, T. & Wood, G. C. Factors affecting the high-temperature oxidation behavior of some dilute nickel- and cobalt-base alloys. *Oxidation of Metals* **11**, 141–150 (1977).
104. Wright, I. G. & Wood, G. C. The isothermal oxidation of Co-Cr alloys in 760 Torr oxygen at 1000°C. *Oxidation of Metals* **11**, 163–191 (1977).
105. Przybylski, K. & Szwagierczak, D. Kinetics and mechanism of high-temperature oxidation of dilute cobalt-chromium alloys. *Oxidation of Metals* **17**, 267–295 (1982).
106. Wood, G. C. High-temperature oxidation of alloys. *Oxidation of Metals* **2**, 11–57 (1970).
107. Cwalina, K. L. *et al.* In Operando Analysis of Passive Film Growth on Ni-Cr and Ni-Cr-Mo Alloys in Chloride Solutions. *Journal of The Electrochemical Society* **166**, C3241–C3253 (2019).
108. Yu, X. X., Perepezko, J. H. & Marks, L. D. Crystallographic Anisotropy of Nonequilibrium Solute Capture. *Acta Materialia*, submitted (2020).
109. Yu, X. X., Taylor, M., Perepezko, J. H. & Marks, L. D. Competition between Thermodynamics, Kinetics and Growth Mode in the Early-stage Oxidation of a CoCrFeNi High-Entropy Alloy. *Acta Materialia*, submitted (2020).
110. Ramanathan, R. & Voorhees, P. W. Kinetics of Solute Capture in Rocksalt Oxides During Oxidation of Binary Alloys, in progress (2020).
111. Codaro, E. N., Melnikov, P., Ramires, I. & Guastaldi, A. C. Corrosion behavior of a cobalt-chromium-molybdenum alloy. *Russian Journal of Electrochemistry* **36**, 1117–1121 (2000).
112. Armijo, J. S. *Mechanisms and kinetics of nickel chromite and cobalt chromite spinel formation* tech. rep. (Stanford Research Institute, Menlo Park, CA, 1969).
113. Pfeiffer, T. & Schmalzried, H. Spinel Formation: A Detailed Analysis. *Zeitschrift für Physikalische Chemie* **161**, 1–17 (1989).

114. Chen, M., Hallstedt, B. & Gauckler, L. J. Thermodynamic assessment of the Co-O system. *Journal of Phase Equilibria* **24**, 212–227 (2003).
115. Hauffe, K., Jänsch-Kaiser, G. & Sharp, D. H. In *Corrosion Handbook* (Wiley-VCH Verlag GmbH, Weinheim, Germany, 2008).
116. Chen, J. *et al.* Low temperature complete combustion of methane over cobalt chromium oxides catalysts. *Catalysis Today* **201**, 12–18 (2013).
117. Lutton Cwalina, K., Demarest, C. R., Gerard, A. Y. & Scully, J. R. Revisiting the effects of molybdenum and tungsten alloying on corrosion behavior of nickel-chromium alloys in aqueous corrosion. *Current Opinion in Solid State and Materials Science* **23**, 129–141 (2019).
118. Metikoš-Huković, M., Pilić, Z., Babić, R. & Omanović, D. Influence of alloying elements on the corrosion stability of CoCrMo implant alloy in Hank's solution. *Acta Biomaterialia* **2**, 693–700 (2006).
119. Zhang, X., Li, Y., Tang, N., Onodera, E. & Chiba, A. Corrosion behaviour of CoCrMo alloys in 2 wt% sulphuric acid solution. *Electrochimica Acta* **125**, 543–555 (2014).
120. Handwerker, C. A., Dynys, J. M., Cannon, R. M. & Coble, R. L. Metal Reference Line Technique for Obtaining Dihedral Angles from Surface Thermal Grooves. *Journal of the American Ceramic Society* **73**, 1365–1370 (1990).
121. Saylor, D. M. & Rohrer, G. S. Measuring the Influence of Grain-Boundary Misorientation on Thermal Groove Geometry in Ceramic Polycrystals. *Journal of the American Ceramic Society* **82**, 1529–1536 (2004).
122. Kim, J. H. *et al.* The role of grain boundaries in the initial oxidation behavior of austenitic stainless steel containing alloyed Cu at 700°C for advanced thermal power plant applications. *Corrosion Science* **96**, 52–66 (2015).
123. Sherman, Q. C., Voorhees, P. W. & Marks, L. D. Thermodynamics of solute capture during the oxidation of multicomponent metals. *Acta Materialia* **181**, 584–594 (2019).

124. Pourzal, R., Catelas, I., Theissmann, R., Kaddick, C. & Fischer, A. Characterization of wear particles generated from CoCrMo alloy under sliding wear conditions. *Wear* **271**, 1658–1666 (2011).
125. Liao, Y. *et al.* CoCrMo metal-on-metal hip replacements. *Physical Chemistry Chemical Physics* **15**, 746–756 (2013).
126. Pandit, H. *et al.* Pseudotumours associated with metal-on-metal hip resurfacings. *Journal of Bone and Joint Surgery - Series B* **90**, 847–851 (2008).
127. Jacobs, J. J. *et al.* Metal-on-metal bearing surfaces. *Journal of the American Academy of Orthopaedic Surgeons* **17**, 69–76 (2009).
128. Fricka, K. B., Ho, H., Peace, W. J. & Engh, C. A. Metal-on-Metal local tissue reaction is associated with corrosion of the head taper junction. *Journal of Arthroplasty* **27**, 26–31 (2012).
129. Ingham, E. & Fisher, J. The role of macrophages in osteolysis of total joint replacement. *Biomaterials* **26**, 1271–1286 (2005).
130. Jacobs, J. J. & Hallab, N. J. Loosening and osteolysis associated with metal-on-metal bearings: A local effect of metal hypersensitivity? *Journal of Bone and Joint Surgery - Series A* **88**, 1171–1172 (2006).
131. Urban, R. M. *et al.* Dissemination of wear particles to the liver, spleen, and abdominal lymph nodes of patients with hip or knee replacement. *Journal of Bone and Joint Surgery - Series A* **82**, 457–477 (2000).
132. Igual Muñoz, A. & Mischler, S. Interactive Effects of Albumin and Phosphate Ions on the Corrosion of CoCrMo Implant Alloy. *Journal of The Electrochemical Society* **154**, C562–C570 (2007).
133. Milošev, I., Hmeljak, J. & Cör, A. Hyaluronic acid stimulates the formation of calcium phosphate on CoCrMo alloy in simulated physiological solution. *Journal of Materials Science: Materials in Medicine* **24**, 555–571 (2013).

134. Li, Y.-S., Wang, K., He, P., Huang, B. X. & Kovacs, P. Surface-enhanced Raman spectroelectrochemical studies of corrosion films on implant Co-Cr-Mo alloy in biosimulating solutions. *Journal of Raman Spectroscopy* **30**, 97–103 (1999).
135. Valero Vidal, C. & Igual Muñoz, A. Electrochemical characterisation of biomedical alloys for surgical implants in simulated body fluids. *Corrosion Science* **50**, 1954–1961 (2008).
136. Valero Vidal, C., Olmo Juan, A. & Igual Muñoz, A. Adsorption of bovine serum albumin on CoCrMo surface: Effect of temperature and protein concentration. *Colloids and Surfaces B: Biointerfaces* **80**, 1–11 (2010).
137. Hanawa, T., Hiromoto, S. & Asami, K. Characterization of the surface oxide film of a Co-Cr-Mo alloy after being located in quasi-biological environments using XPS. *Applied Surface Science* **183**, 68–75 (2001).
138. Milošev, I. The effect of biomolecules on the behaviour of CoCrMo alloy in various simulated physiological solutions. *Electrochimica Acta* **78**, 259–273 (2012).
139. Gispert, M. P., Serro, A. P., Colaço, R. & Saramago, B. Friction and wear mechanisms in hip prosthesis: Comparison of joint materials behaviour in several lubricants. *Wear* **260**, 149–158 (2006).
140. Liao, Y. *et al.* Graphitic tribological layers in metal-on-metal hip replacements. *Science* **334**, 1687–1690 (2011).
141. Fischer, A., Weiß, S. & Wimmer, M. A. The tribological difference between biomedical steels and CoCrMo-alloys. *Journal of the Mechanical Behavior of Biomedical Materials* **9**, 50–62 (2012).
142. Pourzal, R. *et al.* Investigation of the role of tribofilms in self-mating CoCrMo systems utilizing a quartz crystal microtribometer. *Tribology International* **72**, 161–171 (2014).
143. Mathew, M. T. *et al.* Construction of a tribocorrosion test apparatus for the hip joint: Validation, test methodology and analysis. *Wear* **271**, 2651–2659 (2011).

144. Mathew, M. T., Jacobs, J. J. & Wimmer, M. A. Wear-corrosion synergism in a CoCrMo hip bearing alloy is influenced by proteins. *Clinical Orthopaedics and Related Research* **470**, 3109–3117 (2012).
145. Yan, Y., Neville, A. & Dowson, D. Biotribocorrosion of CoCrMo orthopaedic implant materials-Assessing the formation and effect of the biofilm. *Tribology International* **40**, 1492–1499 (2007).
146. Mischler, S. & Muñoz, A. I. Wear of CoCrMo alloys used in metal-on-metal hip joints: A tribocorrosion appraisal. *Wear* **297**, 1081–1094 (2013).
147. Swann, D. A. *et al.* Role of hyaluronic acid in joint lubrication. *Annals of the Rheumatic Diseases* **33**, 318–326 (1974).
148. Radice, S., Yao, J., Babauta, J., Laurent, M. P. & Wimmer, M. A. The effect of hyaluronic acid on the corrosion of an orthopedic CoCrMo-alloy in simulated inflammatory conditions. *Materialia* **6**, 100348 (2019).
149. Igual Muñoz, A. & Mischler, S. Electrochemical Quartz Crystal Microbalance and X-Ray Photoelectron Spectroscopy study of cathodic reactions in Bovine Serum Albumin containing solutions on a Physical Vapour Deposition-CoCrMo biomedical alloy. *Electrochimica Acta* **180**, 96–103 (2015).
150. Ouerd, A., Alemany-Dumont, C., Normand, B. & Szunerits, S. Reactivity of CoCrMo alloy in physiological medium: Electrochemical characterization of the metal/protein interface. *Electrochimica Acta* **53**, 4461–4469 (2008).
151. Yan, Y., Yang, H., Su, Y. & Qiao, L. Albumin adsorption on CoCrMo alloy surfaces. *Scientific Reports* **5**, 1–10 (2015).
152. Hedberg, Y. *et al.* Surface-protein interactions on different stainless steel grades: Effects of protein adsorption, surface changes and metal release. *Journal of Materials Science: Materials in Medicine* **24**, 1015–1033 (2013).
153. Hedberg, Y. S. Role of proteins in the degradation of relatively inert alloys in the human body. *npj Materials Degradation* **2**, 26 (2018).

154. DesJardins, J. *et al.* Increased total knee arthroplasty ultra-high molecular weight polyethylene wear using a clinically relevant hyaluronic acid simulator lubricant. *Proceedings of the Institution of Mechanical Engineers. Part H* **220**, 609–623 (2006).
155. García-Alonso, M. C., Llorente, I., Díaz, I. & Escudero, M. L. Interaction of Hyaluronic Acid with CoCr Alloy Under Immersion and Wear–Corrosion Processes. *Tribology Letters* **66**, 122 (2018).
156. Galandáková, A. *et al.* Characteristics of synovial fluid required for optimization of lubrication fluid for biotribological experiments. *Journal of Biomedical Materials Research - Part B Applied Biomaterials* **105**, 1422–1431 (2017).
157. Martin, E. J., Pourzal, R., Mathew, M. T. & Shull, K. R. Dominant role of molybdenum in the electrochemical deposition of biological macromolecules on metallic surfaces. *Langmuir* **29**, 4813–4822 (2013).
158. Gusieva, K. *et al.* Repassivation Behavior of Individual Grain Facets on Dilute Ni-Cr and Ni-Cr-Mo Alloys in Acidified Chloride Solution. *Journal of Physical Chemistry C* **122**, 19499–19513 (2018).
159. Hansson, A. N., Linderöth, S., Mogensen, M. & Somers, M. A. X-ray diffraction investigation of phase stability in the Co-Cr-O and the Fe-Co-Cr-O systems in air at 1323 K. *Journal of Alloys and Compounds* **402**, 194–200 (2005).
160. Lin, A. Y. W., Müller, A., Yu, X. X., Minor, A. M. & Marks, L. D. Early-stage NiCrMo oxidation revealed by cryo-transmission electron microscopy. *Ultramicroscopy* **200**, 6–11 (2019).
161. Radice, S., Fischer, A. & Wimmer, M. A. *Tribocorrosion of CoCrMo-alloys in Various Model Synovial Fluids: The Role of Hyaluronic Acid* in *ORS 2020 Annual Meeting* (2020), 288.
162. Atkinson, H. V. A review of the role of short-circuit diffusion in the oxidation of nickel, chromium, and nickel-chromium alloys. *Oxidation of Metals* **24**, 177–197 (1985).

163. Saltykov, P., Fabrichnaya, O., Golczewski, J. & Aldinger, F. Thermodynamic modeling of oxidation of Al-Cr-Ni alloys. *Journal of Alloys and Compounds* **381**, 99–113 (2004).
164. Ingham, B., Hendy, S. C., Laycock, N. J. & Ryan, M. P. Estimates of Thermodynamic Stability of Iron-Chromium Spinels in Aqueous Solution Based on First-Principles Calculations. *Electrochemical and Solid-State Letters* **10**, C57–C59 (2007).
165. Chattopadhyay, B. & Wood, G. C. The transient oxidation of alloys. *Oxidation of Metals* **2**, 373–399 (1970).
166. Wood, G. C. & Chattopadhyay, B. Transient oxidation of Ni-base alloys. *Corrosion Science* **10**, 471–480 (1970).
167. Yang, J. C., Schumann, E., Levin, I. & Rühle, M. Transient oxidation of NiAl. *Acta Materialia* **46**, 2195–2201 (1998).
168. Stellwag, B. The mechanism of oxide film formation on austenitic stainless steels in high temperature water. *Corrosion Science* **40**, 337–370 (1998).
169. Sennour, M. *et al.* A detailed TEM and SEM study of Ni-base alloys oxide scales formed in primary conditions of pressurized water reactor. *Journal of Nuclear Materials* **402**, 147–156 (2010).
170. Wood, G. C., Hodgkiess, T. & Whittle, D. P. A comparison of the scaling behaviour of pure iron-chromium and nickel-chromium alloys in oxygen. *Corrosion Science* **6**, 129–147 (1966).
171. Douglass, D. The oxidation mechanism of dilute Ni-Cr alloys. *Corrosion Science* **8**, 665–678 (1968).
172. McIntyre, N. S., Chan, T. C. & Chen, C. Characterization of oxide structures formed on nickel-chromium alloy during low pressure oxidation at 500–600°C. *Oxidation of Metals* **33**, 457–479 (1990).
173. Calvarin, G., Molins, R. & Huntz, A. M. Oxidation Mechanism of Ni-20Cr Foils and Its Relation to the Oxide-Scale Microstructure. *Oxidation of Metals* **53**, 25–48 (2000).

174. Chen, X., Hou, P. Y., Jacobson, C. P., Visco, S. J. & De Jonghe, L. C. Protective coating on stainless steel interconnect for SOFCs: Oxidation kinetics and electrical properties. *Solid State Ionics* **176**, 425–433 (2005).
175. Wei, P., Deng, X., Bateni, M. R. & Petric, A. Oxidation and electrical conductivity behavior of spinel coatings for metallic interconnects of solid oxide fuel cells. *Corrosion* **63**, 529–536 (2007).
176. Navrotsky, A. & Kleppa, O. J. The thermodynamics of cation distributions in simple spinels. *Journal of Inorganic and Nuclear Chemistry* **29**, 2701–2714 (1967).
177. Stevanović, V., D’Avezac, M. & Zunger, A. Universal electrostatic origin of cation ordering in A₂BO₄ spinel oxides. *Journal of the American Chemical Society* **133**, 11649–11654 (2011).
178. Douglass, D. L. & Armijo, J. S. The influence of manganese and silicon on the oxidation behavior of Co-20Cr. *Oxidation of Metals* **3**, 185–202 (1971).
179. Takei, A. & Nii, K. The Growth Process of Oxide Layers in the Initial Stage of Oxidation of 80Ni-20Cr Alloy. *Transactions of the Japan Institute of Metals* **17**, 211–219 (1976).
180. Kofstad, P. On the formation of porosity and microchannels in growing scales. *Oxidation of Metals* **24**, 265–276 (1985).
181. Wagner, C. On the Mechanism of Formation of Ionically Bonded Higher Order (Double Salts, Spinel, Silicates). *Zeitschrift für Physikalische Chemie* **34**, 309–316 (1936).
182. Lindner, R. & Akerstrom, A. Self-Diffusion and Reaction in Oxide and Spinel Systems. *Zeitschrift für Physikalische Chemie* **6**, 162–177 (1956).
183. Sockel, H. G. *Morphology and Kinetics of Spinel Formation* PhD thesis (University of Goettingen, 1965).
184. Kunnmann, W., Rogers, D. B. & Wold, A. The use of CO-CO₂ atmospheres for the preparation and free energy determinations of several oxide systems. *Journal of Physics and Chemistry of Solids* **24**, 1535–1538 (1963).

185. Davies, H. & Smeltzer, W. W. Oxygen and Metal Activities of the Chromium-Nickel-Oxygen System Between 900° and 1100°C. *Journal of The Electrochemical Society* **121**, 543–549 (1974).
186. Müller, F. & Kleppa, O. J. Thermodynamics of formation of chromite spinels. *Journal of Inorganic and Nuclear Chemistry* **35**, 2673–2678 (1973).
187. Schaefer, S. C. *Electrochemical Determination of Thermodynamic Properties of NiCr₂O₄ and CoCr₂O₄* tech. rep. (United States Department of the Interior, Bureau of Mines, 1986).
188. Kung, S.-C. Gibbs energy of formation of nickel chromite. *Metallurgical Transactions B* **22**, 673–675 (1991).
189. Kurepin, V. A., Kulik, D. A., Hitpold, A. & Nicolet, M. *Thermodynamic Modelling of Fe-Cr-Ni Spinel Formation at the Light-Water Reactor Conditions* tech. rep. (Paul Scherrer Institute, Villigen, 2002).
190. Taylor, J. R. & Dinsdale, A. T. Thermodynamic assessment of the Ni-O, Cr-O and Cr-Ni-O systems using the ionic liquid and compound energy models. *Zeitschrift fuer Metallkunde/Materials Research and Advanced Techniques* **81**, 354–366 (1990).
191. Rudnyi, E. B., Kaibicheva, E. A., Sidorov, L. N., Varshavskii, M. T. & Men, A. N. (Ion + molecule) equilibrium technique applied to the determination of the activities of Cr₂O₃ and NiO. Standard molar Gibbs energy of formation of NiCr₂O₄. *The Journal of Chemical Thermodynamics* **22**, 623–632 (1990).
192. Shi, X., Bernasek, S. L. & Selloni, A. Formation, electronic structure, and defects of Ni substituted spinel cobalt oxide: A DFT+U study. *Journal of Physical Chemistry C* **120**, 14892–14898 (2016).
193. Buckett, M. I. & Marks, L. D. Electron irradiation damage in NiO. *Surface Science* **232**, 353–366 (1990).

194. Lin, C. H., Chen, S. Y. & Shen, P. Defects, Lattice Correspondence, and Optical Properties of Spinel-like Cr₃O₄ Condensates by Pulsed Laser Ablation in Water. *The Journal of Physical Chemistry C* **113**, 16356–16363 (2009).
195. Anderson, R. M., Heesterbeek, H., Klinkenberg, D. & Hollingsworth, T. D. How will country-based mitigation measures influence the course of the COVID-19 epidemic? *The Lancet* **395**, 931–934 (2020).
196. Xu, X., Gao, J. & Hong, W. Ni-based chromite spinel for high-performance supercapacitors. *RSC Advances* **6**, 29646–29653 (2016).
197. Thierry, D. *et al.* In-Situ Raman Spectroscopy Combined with X-Ray Photoelectron Spectroscopy and Nuclear Microanalysis for Studies of Anodic Corrosion Film Formation on Fe-Cr Single Crystals. *Journal of The Electrochemical Society* **135**, 305–310 (1988).
198. Maslar, J. E., Hurst, W. S., Bowers, J. J., Hendricks, J. H. & Aquino, M. I. In situ Raman spectroscopic investigation of nickel hydrothermal corrosion. *Corrosion* **58**, 225–231 (2002).
199. Maslar, J. E., Hurst, W. S., Bowers, W. J., Hendricks, J. H. & Windsor, E. S. Alloy 600 Aqueous Corrosion at Elevated Temperatures and Pressures: An In Situ Raman Spectroscopic Investigation. *Journal of The Electrochemical Society* **156**, C103–C113 (2009).
200. Yamamoto, S. *et al.* In situ x-ray photoelectron spectroscopy studies of water on metals and oxides at ambient conditions. *Journal of Physics: Condensed Matter* **20**, 184025 (2008).
201. Jiang, P. *et al.* In situ soft X-ray absorption spectroscopy investigation of electrochemical corrosion of copper in aqueous NaHCO₃ solution. *Electrochemistry Communications* **12**, 820–822 (2010).

202. Milošev, I., Metikoš-Huković, M. & Strehblow, H.-H. Passive film on orthopaedic TiAlV alloy formed in physiological solution investigated by X-ray photoelectron spectroscopy. *Biomaterials* **21**, 2103–2113 (2000).
203. Schmuki, P., Virtanen, S., Davenport, A. J. & Vitus, C. M. Transpassive Dissolution of Cr and Sputter-Deposited Cr Oxides Studied by In Situ X-Ray Near-Edge Spectroscopy. *Journal of The Electrochemical Society* **143**, 3997–4005 (1996).
204. Davoodi, A., Pan, J., Leygraf, C. & Norgren, S. Integrated AFM and SECM for in situ studies of localized corrosion of Al alloys. *Electrochimica Acta* **52**, 7697–7705 (2007).
205. Kowal, K., DeLuccia, J., Josefowicz, J. Y., Laird, C. & Farrington, G. C. In Situ Atomic Force Microscopy Observations of the Corrosion Behavior of Aluminum-Copper Alloys. *Journal of The Electrochemical Society* **143**, 2471–2481 (1996).
206. Martin, F. A., Bataillon, C. & Cousty, J. In situ AFM detection of pit onset location on a 304L stainless steel. *Corrosion Science* **50**, 84–92 (2008).
207. Zuili, D., Maurice, V. & Marcus, P. Surface Structure of Nickel in Acid Solution Studied by In Situ Scanning Tunneling Microscopy. *Journal of The Electrochemical Society* **147**, 1393–1400 (2000).
208. Suzuki, T., Yamada, T. & Itaya, K. In Situ Electrochemical Scanning Tunneling Microscopy of Ni(111), Ni(100), and Sulfur-Modified Ni(100) in Acidic Solution. *The Journal of Physical Chemistry* **100**, 8954–8961 (1996).
209. Seyeux, A., Maurice, V., Klein, L. H. & Marcus, P. In situ scanning tunnelling microscopic study of the initial stages of growth and of the structure of the passive film on Ni(111) in 1 mM NaOH(aq). *Journal of Solid State Electrochemistry* **9**, 337–346 (2005).
210. Kunze, J., Maurice, V., Klein, L. H., Strehblow, H.-H. & Marcus, P. In situ STM study of the effect of chlorides on the initial stages of anodic oxidation of Cu(111) in alkaline solutions. *Electrochimica Acta* **48**, 1157–1167 (2003).

211. Merola, C. *et al.* In situ nano- to microscopic imaging and growth mechanism of electrochemical dissolution (e.g., corrosion) of a confined metal surface. *Proceedings of the National Academy of Sciences* **114**, 9541–9546 (2017).
212. Huang, J. Y. *et al.* In Situ Observation of the Electrochemical Lithiation of a Single SnO₂ Nanowire Electrode. *Science* **330**, 1515–1520 (2010).
213. Liu, X. H. *et al.* In Situ TEM Experiments of Electrochemical Lithiation and Delithiation of Individual Nanostructures. *Advanced Energy Materials* **2**, 722–741 (2012).
214. Gu, M. *et al.* Demonstration of an electrochemical liquid cell for operando transmission electron microscopy observation of the lithiation/delithiation behavior of Si nanowire battery anodes. *Nano Letters* **13**, 6106–6112 (2013).
215. Holtz, M. E. *et al.* Nanoscale imaging of lithium ion distribution during in situ operation of battery electrode and electrolyte. *Nano Letters* **14**, 1453–1459 (2014).
216. Zeng, Z. *et al.* Visualization of electrode-electrolyte interfaces in LiPF₆/EC/DEC electrolyte for lithium ion batteries via in situ TEM. *Nano Letters* **14**, 1745–1750 (2014).
217. Sacci, R. L. *et al.* Direct visualization of initial SEI morphology and growth kinetics during lithium deposition by in situ electrochemical transmission electron microscopy. *Chemical Communications* **50**, 2104–2107 (2014).
218. Unocic, R. R. *et al.* Quantitative electrochemical measurements using in situ ec-S/TEM devices. *Microscopy and Microanalysis* **20**, 452–461 (2014).
219. Chee, S. W., Duquette, D. J., Ross, F. M. & Hull, R. Metastable structures in Al thin films before the onset of corrosion pitting as observed using liquid cell transmission electron microscopy. *Microscopy and Microanalysis* **20**, 462–468 (2014).
220. Chee, S. W. *et al.* Studying localized corrosion using liquid cell transmission electron microscopy. *Chemical Communications* **51**, 168–171 (2015).

221. Smith, D. J., McCartney, M. R. & Bursill, L. A. The electron-beam-induced reduction of transition metal oxide surfaces to metallic lower oxides. *Ultramicroscopy* **23**, 299–303 (1987).
222. Zheng, H. & Zhu, Y. Perspectives on in situ electron microscopy. *Ultramicroscopy* **180**, 188–196 (2017).
223. Dubochet, J. & McDowell, A. Vitrification of Pure Water for Electron Microscopy. *Journal of Microscopy* **124**, 3–4 (1981).
224. Dubochet, J. *et al.* Cryo-electron microscopy of vitrified specimens. *Quarterly Reviews of Biophysics* **21**, 129–228 (1988).
225. Dobro, M. J., Melanson, L. A., Jensen, G. J. & McDowell, A. W. In *Methods in Enzymology* 63–82 (Academic Press Inc., 2010).
226. Thompson, R. F., Walker, M., Siebert, C. A., Muench, S. P. & Ranson, N. A. An introduction to sample preparation and imaging by cryo-electron microscopy for structural biology. *Methods* **100**, 3–15 (2016).
227. Schaffer, M. *et al.* Optimized cryo-focused ion beam sample preparation aimed at in situ structural studies of membrane proteins. *Journal of Structural Biology* **197**, 73–82 (2017).
228. Villa, E., Schaffer, M., Plitzko, J. M. & Baumeister, W. Opening windows into the cell: Focused-ion-beam milling for cryo-electron tomography. *Current Opinion in Structural Biology* **23**, 771–777 (2013).
229. Stott, F. H., Wood, G. C. & Stringer, J. The influence of alloying elements on the development and maintenance of protective scales. *Oxidation of Metals* **44**, 113–145 (1995).
230. Piron, D. L., Koutsoukos, E. P. & Nobe, K. Corrosion Behavior of Nickel and Inconel in Acidic Chloride Solutions. *Corrosion* **25**, 151–156 (1969).
231. Lillard, R. S., Jurinski, M. P. & Scully, J. R. Crevice corrosion of alloy 625 in chlorinated ASTM artificial ocean water. *Corrosion* **50**, 251–265 (1994).

232. Cairns, R. W. & Ott, E. X-Ray Studies of the System Nickel-Oxygen-Water. I. Nickelous Oxide and Hydroxide. *Journal of the American Chemical Society* **55**, 527–533 (1933).
233. Khoi, N. N. Growth and Structure of Nickel Oxide on Nickel Crystal Faces. *Journal of The Electrochemical Society* **122**, 1495 (1975).
234. Hono, K. *et al.* Atom-probe study of the initial stage of selective oxidation of Ni from the Cu-Ni alloy system. *Surface Science* **245**, 132–149 (1991).
235. Kjellqvist, L., Selleby, M. & Sundman, B. Thermodynamic modelling of the Cr-Fe-Ni-O system. *Calphad* **32**, 577–592 (2008).
236. Van der Ven, A., Morgan, D., Meng, Y. S. & Ceder, G. Phase Stability of Nickel Hydroxides and Oxyhydroxides. *Journal of The Electrochemical Society* **153**, A210–A215 (2006).
237. McEwen, R. S. Crystallographic studies on nickel hydroxide and the higher nickel oxides. *The Journal of Physical Chemistry* **75**, 1782–1789 (1971).
238. Hall, D. S., Lockwood, D. J., Bock, C. & MacDougall, B. R. Nickel hydroxides and related materials: a review of their structures, synthesis and properties. *Proceedings of the Royal Society A: Mathematical, Physical and Engineering Sciences* **471**, 20140792–20140792 (2014).
239. Comolli, L. R. *et al.* A portable cryo-plunger for on-site intact cryogenic microscopy sample preparation in natural environments. *Microscopy Research and Technique* **75**, 829–836 (2012).
240. Zachman, M. J., Asenath-Smith, E., Estroff, L. A. & Kourkoutis, L. F. Site-specific preparation of intact solid-liquid interfaces by label-free in situ localization and Cryo-focused ion beam lift-out. *Microscopy and Microanalysis* **22**, 1338–1349 (2016).
241. Marcus, P. & Maurice, V. Atomic level characterization in corrosion studies. *Philosophical Transactions of the Royal Society A: Mathematical, Physical and Engineering Sciences* **375**, 20160414 (2017).

242. Chebeir, M. & Liu, H. Oxidation of Cr(III)-Fe(III) Mixed-Phase Hydroxides by Chlorine: Implications on the Control of Hexavalent Chromium in Drinking Water. *Environmental Science and Technology* **52**, 7663–7670 (2018).
243. Bode, H., Dehmelt, K. & Witte, J. Zur kenntnis der nickelhydroxidelektrode-I. Über das nickel (II)-hydroxidhydrat. *Electrochimica Acta* **11**, 1079–1087 (1966).
244. Oliva, P. *et al.* Review of the structure and the electrochemistry of nickel hydroxides and oxy-hydroxides. *Journal of Power Sources* **8**, 229–255 (1982).
245. Marcus, P. & Herbelin, J.-M. The entry of chloride ions into passive films on nickel studied by spectroscopic (ESCA) and nuclear (^{36}Cl radiotracer) methods. *Corrosion Science* **34**, 1123–1145 (1993).
246. Strehblow, H.-H. In *Advances in Electrochemical Science and Engineering, Volume 8* (eds Alkire, R. C. & Kolb, D. M.) 271–374 (Wiley-VCH Verlag, Weinheim, 2002).
247. Haupt, S. & Strehblow, H. H. Corrosion, Layer Formation, and Oxide Reduction of Passive Iron in Alkaline Solution: A Combined Electrochemical and Surface Analytical Study. *Langmuir* **3**, 873–885 (1987).
248. Maurice, V. & Marcus, P. Passive films at the nanoscale. *Electrochimica Acta* **84**, 129–138 (2012).
249. Macdonald, D. D. Passivity - The key to our metals-based civilization. *Pure and Applied Chemistry* **71**, 951–978 (1999).
250. Gilberg, M. R. & Seeley, N. J. The identity of compounds containing chloride ions in marine iron corrosion products: A critical review. *Studies in Conservation* **26**, 50–56 (1981).
251. Russo, C. J. & Henderson, R. Charge accumulation in electron cryomicroscopy. *Ultramicroscopy* **187**, 43–49 (2018).
252. Zachman, M. J., Tu, Z., Choudhury, S., Archer, L. A. & Kourkoutis, L. F. Cryo-STEM mapping of solid–liquid interfaces and dendrites in lithium-metal batteries. *Nature* **560**, 345–349 (2018).

253. Merkle, A. P., Erdemir, A., Eryilmaz, O. L., Johnson, J. A. & Marks, L. D. In situ TEM studies of tribo-induced bonding modifications in near-frictionless carbon films. *Carbon* **48**, 587–591 (2010).
254. Casillas, G., Liao, Y., Jose-Yacaman, M. & Marks, L. D. Monolayer Transfer Layers During Sliding at the Atomic Scale. *Tribology Letters* **59**, 1–5 (2015).
255. Hoffman, E. E. & Marks, L. D. Graphitic Carbon Films Across Systems. *Tribology Letters* **63**, 32 (2016).
256. Hoffman, E., Lin, A. & Marks, L. D. In Situ Evidence for Stability of Low Friction Nanostructures in MoS₂, in preparation (2018).
257. Nilsson, H. M., de Knoop, L., Cumings, J. & Olsson, E. Localized resistance measurements of wrinkled reduced graphene oxide using in-situ transmission electron microscopy. *Carbon* **113**, 340–345 (2017).
258. Zeng, L. *et al.* Correlation between Electrical Transport and Nanoscale Strain in InAs/In_{0.6}Ga_{0.4}As Core-Shell Nanowires. *Nano Letters* **18**, 4949–4956 (2018).
259. Gammer, C. *et al.* Local and transient nanoscale strain mapping during in situ deformation. *Applied Physics Letters* **109**, 081906 (2016).
260. Minor, A. M. & Dehm, G. Advances in in situ nanomechanical testing. *MRS Bulletin* **44**, 438–442 (2019).
261. Lin, A. Y. W., Yu, X.-X., Dato, A., Krauss, G. & Marks, L. D. In situ observations of graphitic staples in crumpled graphene. *Carbon* **132**, 760–765 (2018).
262. Lee, C., Wei, X., Kysar, J. W. & Hone, J. Measurement of the elastic properties and intrinsic strength of monolayer graphene. *Science* **321**, 385–388 (2008).
263. Ramanathan, T. *et al.* Functionalized graphene sheets for polymer nanocomposites. *Nature Nanotechnology* **3**, 327–331 (2008).
264. Novoselov, K. S. *et al.* Electric field in atomically thin carbon films. *Science* **306**, 666–669 (2004).

265. Neto, A. H. C., Guinea, F., Peres, N. M. R., Novoselov, K. S. & Geim, A. K. The electronic properties of graphene. *Reviews of Modern Physics* **81**, 109–162 (2007).
266. Geim, A. K. & Novoselov, K. S. The rise of graphene. *Nature Materials* **6**, 183–191 (2007).
267. Geim, A. K. Graphene: Status and prospects. *Science* **324**, 1530–1534 (2009).
268. Schwierz, F. Graphene transistors. *Nature Nanotechnology* **5**, 487–496 (2010).
269. Berman, D., Erdemir, A. & Sumant, A. V. Graphene: A new emerging lubricant. *Materials Today* **17**, 31–42 (2014).
270. Ou, J. *et al.* Tribology study of reduced graphene oxide sheets on silicon substrate synthesized via covalent assembly. *Langmuir* **26**, 15830–15836 (2010).
271. Bunch, J. S. *et al.* Impermeable atomic membranes from graphene sheets. *Nano Letters* **8**, 2458–2462 (2008).
272. Kim, K. S. *et al.* Chemical vapor deposition-grown graphene: The thinnest solid lubricant. *ACS Nano* **5**, 5107–5114 (2011).
273. Won, M. S., Penkov, O. V. & Kim, D. E. Durability and degradation mechanism of graphene coatings deposited on Cu substrates under dry contact sliding. *Carbon* **54**, 472–481 (2013).
274. Berman, D., Erdemir, A. & Sumant, A. V. Few layer graphene to reduce wear and friction on sliding steel surfaces. *Carbon* **54**, 454–459 (2013).
275. Dou, X. *et al.* Self-dispersed crumpled graphene balls in oil for friction and wear reduction. *Proceedings of the National Academy of Sciences* **113**, 1528–1533 (2016).
276. Dato, A., Radmilovic, V., Lee, Z., Phillips, J. & Frenklach, M. Substrate-free gas-phase synthesis of graphene sheets. *Nano Letters* **8**, 2012–2016 (2008).
277. Dato, A. *et al.* Clean and highly ordered graphene synthesized in the gas phase. *Chemical Communications* **2009**, 6095–6097 (2009).

278. Dato, A. & Frenklach, M. Substrate-free microwave synthesis of graphene: experimental conditions and hydrocarbon precursors. *New Journal of Physics* **12**, 125013 (2010).
279. Cranford, S. W. & Buehler, M. J. Packing efficiency and accessible surface area of crumpled graphene. *Physical Review B* **84**, 205451 (2011).
280. Luo, J. *et al.* Compression and aggregation-resistant particles of crumpled soft sheets. *ACS Nano* **5**, 8943–8949 (2011).
281. Zhang, K. & Arroyo, M. Adhesion and friction control localised folding in supported graphene. *Journal of Applied Physics* **113**, 193501 (2013).
282. Zang, J. *et al.* Multifunctionality and control of the crumpling and unfolding of large-area graphene. *Nature Materials* **12**, 321–325 (2013).
283. Vliegenthart, G. A. & Gompper, G. Forced crumpling of self-avoiding elastic sheets. *Nature Materials* **5**, 216–221 (2006).
284. Tallinen, T., Ström, J. A. & Timonen, J. The effect of plasticity in crumpling of thin sheets. *Nature Materials* **8**, 25–29 (2009).
285. Ma, X., Zachariah, M. R. & Zangmeister, C. D. Crumpled nanopaper from graphene oxide. *Nano Letters* **12**, 486–489 (2012).
286. Liao, Y., Hoffman, E. & Marks, L. D. Nanoscale abrasive wear of CoCrMo in in situ TEM sliding. *Tribology Letters* **57**, 28 (2015).
287. Zhang, J. *et al.* Free folding of suspended graphene sheets by random mechanical stimulation. *Physical Review Letters* **104**, 166805 (2010).
288. Witten, T. A. Stress focusing in elastic sheets. *Reviews of Modern Physics* **79**, 643–675 (2007).
289. Matan, K., Williams, R. B., Witten, T. A. & Nagel, S. R. Crumpling a thin sheet. *Physical Review Letters* **88**, 761011–761014 (2002).
290. Aharoni, H. & Sharon, E. Direct observation of the temporal and spatial dynamics during crumpling. *Nature Materials* **9**, 993–997 (2010).

291. Balankin, A. S. & Huerta, O. S. Entropic rigidity of a crumpling network in a randomly folded thin sheet. *Physical Review E* **77**, 51124 (2008).
292. Cambou, A. D. & Menon, N. Three-dimensional structure of a sheet crumpled into a ball. *Proceedings of the National Academy of Sciences* **108**, 14741–14745 (2011).
293. Meyer, J. C. *et al.* The structure of suspended graphene sheets. *Nature* **446**, 60–63 (2007).
294. Schniepp, H. C. *et al.* Bending Properties of Single Functionalized Graphene Sheets Probed by Atomic Force Microscopy. *ACS Nano* **2**, 2577–2584 (2008).
295. Wierzbicki, T. & Abramowicz, W. On the Crushing Mechanics of Thin-Walled Structures. *Journal of Applied Mechanics* **50**, 727–734 (1983).
296. Chang, C., Song, Z., Lin, J. & Xu, Z. How graphene crumples are stabilized? *RSC Advances* **3**, 2720–2726 (2013).
297. Mizzi, C. A., Lin, A. Y. W. & Marks, L. D. Does Flexoelectricity Drive Triboelectricity? *Physical Review Letters* **123**, 116103 (2019).
298. Harper, W. R. *Contact and Frictional Electrification* (Oxford University Press, Oxford, 1967).
299. Lacks, D. J. & Sankaran, R. M. Contact electrification of insulating materials. *Journal of Physics D: Applied Physics* **44**, 453001 (2011).
300. Liu, C. Y. & Bard, A. J. Electrostatic electrochemistry at insulators. *Nature Materials* **7**, 505–509 (2008).
301. Lowell, J. & Rose-Innes, A. C. Contact electrification. *Advances in Physics* **29**, 947–1023 (2006).
302. Davies, D. K. Charge Generation on Dielectric Surfaces. *Journal of Physics D: Applied Physics* **2**, 1533–1537 (1969).
303. Diaz, A. F. & Fenzel-Alexander, D. An Ion Transfer Model for Contact Charging. *Langmuir* **9**, 1009–1015 (1993).

304. McCarty, L. S. & Whitesides, G. M. Electrostatic charging due to separation of ions at interfaces: contact electrification of ionic electrets. *Angewandte Chemie. International Edition in English* **47**, 2188–2207 (2008).
305. Baytekin, H. T., Baytekin, B., Incorvati, J. T. & Grzybowski, B. A. Material transfer and polarity reversal in contact charging. *Angewandte Chemie. International Edition in English* **51**, 4843–4847 (2012).
306. Galembeck, F. *et al.* Friction, tribochemistry and triboelectricity: recent progress and perspectives. *RSC Advances* **4**, 64280–64298 (2014).
307. Lin, S. *et al.* Electron Transfer in Nanoscale Contact Electrification: Effect of Temperature in Metal-Dielectric Case. *Advanced Materials*, 1808197 (2019).
308. Kok, J. F. & Lacks, D. J. Electrification of granular systems of identical insulators. *Physical Review E* **79**, 051304 (2009).
309. Lacks, D. J., Duff, N. & Kumar, S. K. Nonequilibrium accumulation of surface species and triboelectric charging in single component particulate systems. *Physical Review Letters* **100**, 188305 (2008).
310. Lowell, J. & Truscott, W. S. Triboelectrification of identical insulators. II. Theory and further experiments. *Journal of Applied Physics D: Applied Physics* **19**, 1281–1298 (1986).
311. Bowden, F. P. & Tabor, D. *The Friction and Lubrication of Solids* (Clarendon Press, 1958).
312. Cross, L. E. Flexoelectric effects: Charge separation in insulating solids subjected to elastic strain gradients. *Journal of Materials Science* **41**, 1573–4803 (2006).
313. Yudin, P. V. & Tagantsev, A. K. Fundamentals of flexoelectricity in solids. *Nanotechnology* **24**, 432001 (2013).
314. Zubko, P., Catalan, G. & Tagantsev, A. K. Flexoelectric Effect in Solids. *Annual Review of Materials Research* **43**, 387–421 (2013).

315. Koirala, P., Mizzi, C. A. & Marks, L. D. Direct Observation of Large Flexoelectric Bending at the Nanoscale in Lanthanide Scandates. *Nano Letters* **18**, 3850–3856 (2018).
316. Lee, D. *et al.* Giant flexoelectric effect in ferroelectric epitaxial thin films. *Physical Review Letters* **107**, 057602 (2011).
317. Gharbi, M., Sun, Z. H., Sharma, P. & White, K. The origins of electromechanical indentation size effect in ferroelectrics. *Applied Physics Letters* **95**, 142901 (2009).
318. Robinson, C. R., White, K. W. & Sharma, P. Elucidating the mechanism for indentation size-effect in dielectrics. *Applied Physics Letters* **101**, 122901 (2012).
319. Abdollahi, A. *et al.* Fracture toughening and toughness asymmetry induced by flexoelectricity. *Physical Review B* **92**, 094101 (2015).
320. Das, S. *et al.* Enhanced flexoelectricity at reduced dimensions revealed by mechanically tunable quantum tunnelling. *Nature Communications* **10**, 537 (2019).
321. Burgo, T. A. L., Silva, C. A., Balestrin, L. B. S. & Galembeck, F. Friction coefficient dependence on electrostatic tribocharging. *Scientific Reports* **3**, 2384 (2013).
322. Sayfidinov, K., Cezan, S. D., Baytekin, B. & Baytekin, H. T. Minimizing friction, wear, and energy losses by eliminating contact charging. *Science Advances* **4**, eaau3808 (2018).
323. Nakayama, K. Tribocharging and friction in insulators in ambient air. *Wear* **194**, 185–189 (1996).
324. Wolloch, M., Levita, G., Restuccia, P. & Righi, M. C. Interfacial Charge Density and Its Connection to Adhesion and Frictional Forces. *Physical Review Letters* **121**, 026804 (2018).
325. Zubko, P., Catalan, G., Buckley, A., Welche, P. R. & Scott, J. F. Strain-gradient-induced polarization in SrTiO₃ single Crystals. *Physical Review Letters* **99**, 167601 (2007).

326. Narvaez, J., Saremi, S., Hong, J., Stengel, M. & Catalan, G. Large Flexoelectric Anisotropy in Paraelectric Barium Titanate. *Physical Review Letters* **115**, 037601 (2015).
327. Kogan, S. M. Piezoelectric Effect during Inhomogeneous Deformation and Acoustic Scattering of Carriers in Crystals. *Soviet Physics-Solid State* **5**, 2069–2070 (1964).
328. Burgo, T. A. & Erdemir, A. Bipolar tribocharging signal during friction force fluctuations at metal-insulator interfaces. *Angewandte Chemie. International Edition in English* **53**, 12101–12105 (2014).
329. Escobar, J. V., Chakravarty, A. & Putterman, S. J. Effect of anodic oxidation of single crystal boron doped diamond on tribocurrent and macroscopic friction force with metals. *Diamond and Related Materials* **36**, 8–15 (2013).
330. Forward, K. M., Lacks, D. J. & Sankaran, R. M. Charge segregation depends on particle size in triboelectrically charged granular materials. *Physical Review Letters* **102**, 028001 (2009).
331. Pham, R., Virnelson, R. C., Sankaran, R. M. & Lacks, D. J. Contact charging between surfaces of identical insulating materials in asymmetric geometries. *Journal of Electrostatics* **69**, 456–460 (2011).
332. Shinbrot, T., Komatsu, T. S. & Zhao, Q. Spontaneous tribocharging of similar materials. *EPL (Europhysics Letters)* **83**, 24004 (2008).
333. Waitukaitis, S. R., Lee, V., Pierson, J. M., Forman, S. L. & Jaeger, H. M. Size-Dependent Same-Material Tribocharging in Insulating Grains. *Physical Review Letters* **112**, 218001 (2014).
334. Baytekin, H. T. *et al.* The Mosaic of Surface Charge in Contact Electrification. *Science* **333**, 308–312 (2011).
335. Burgo, T. A. *et al.* Triboelectricity: macroscopic charge patterns formed by self-arraying ions on polymer surfaces. *Langmuir* **28**, 7407–7416 (2012).

336. Musa, U. G., Cezan, S. D., Baytekin, B. & Baytekin, H. T. The Charging Events in Contact-Separation Electrification. *Scientific Reports* **8**, 2472 (2018).
337. Terris, B. D., Stern, J. E., Rugar, D. & Mamin, H. J. Contact electrification using force microscopy. *Physical Review Letters* **63**, 2669–2672 (1989).
338. Xu, C. *et al.* Contact-Electrification between Two Identical Materials: Curvature Effect. *ACS Nano* **13**, 2034–2041 (2019).
339. Nemeth, E., Albrecht, V., Schubert, G. & Simon, F. Polymer tribo-electric charging: dependence on thermodynamic surface properties and relative humidity. *Journal of Electrostatics* **58**, 3–16 (2003).
340. Fan, F.-R. *et al.* Transparent Triboelectric Nanogenerators and Self-Powered Pressure Sensors Based on Micropatterned Plastic Films. *Nano Letters* **12**, 3109–3114 (2012).
341. Zhu, G. *et al.* Triboelectric-Generator-Driven Pulse Electrodeposition for Micropatterning. *Nano Letters* **12**, 4960–4965 (2012).
342. Dharmasena, R. *et al.* Triboelectric nanogenerators: providing a fundamental framework. *Energy and Environmental Science* **10**, 1801–1811 (2017).
343. Niu, S. *et al.* Theoretical study of contact-mode triboelectric nanogenerators as an effective power source. *Energy and Environmental Science* **6**, 3576–3583 (2013).
344. Wahl, K. J., Dunn, D. N. & Singer, I. L. Wear behavior of Pb-Mo-S solid lubricating coatings. *Wear* **230**, 175–183 (1999).
345. Petrov, A. G. Flexoelectricity of model and living membranes. *Biochimica et Biophysica Acta* **1561**, 1–25 (2002).
346. Vasquez-Sancho, F., Abdollahi, A., Damjanovic, D. & Catalan, G. Flexoelectricity in Bones. *Advanced Materials* **30**, 1705316 (2018).
347. Walton, A. J. Triboluminescence. *Advances in Physics* **26**, 887–948 (1977).
348. Zink, J. I. Triboluminescence. *Accounts of Chemical Research* **11**, 289–295 (1978).

349. Camara, C. G., Escobar, J. V., Hird, J. R. & Putterman, S. J. Correlation between nanosecond X-ray flashes and stick–slip friction in peeling tape. *Nature* **455**, 1089–1092 (2008).
350. Nakayama, K. & Nevshupa, R. A. Plasma generation in a gap around a sliding contact. *Journal of Physics D: Applied Physics* **35**, L53–L56 (2002).

APPENDIX A

DFT CIFs

A.1 Ni₃O₄

```
data_Wien2k_Data
_cell_length_a    5.848660
_cell_length_b    5.848660
_cell_length_c    8.271254
_cell_angle_alpha 90.000000
_cell_angle_beta  90.000000
_cell_angle_gamma 90.000000
_cell_measurement_temperature 0.0
_diffrn_ambient_temperature 0.0
_symmetry_space_group_name_H-M      'Imm2  '
_symmetry_space_group_number    44
_refine_date    '14- 4-2020'
_refine_method  'generated from Wien2k code'
_refine_special_details

loop_
_symmetry_equiv_pos_as_xyz
  +x,+y,+z
  -x,-y,+z
  +x,-y,+z
  -x,+y,+z
  +x+1/2,+y+1/2,+z+1/2
  -x+1/2,-y+1/2,+z+1/2
```

```

+x+1/2,-y+1/2,+z+1/2
-x+1/2,+y+1/2,+z+1/2
loop_
_atom_site_label
_atom_site_type_symbol
_atom_site_fract_x
_atom_site_fract_y
_atom_site_fract_z
_atom_site_U_iso_or_equiv
Ni001 Ni01  0.00000000  0.00000000  0.00220191  0.05000000
Ni002 Ni02  0.00000000  0.50000000  0.25261160  0.05000000
Ni001 Ni01  0.74909529  0.00000000  0.37615072  0.05000000
Ni002 Ni02  0.00000000  0.24915818  0.62605034  0.05000000
O0001 O01   0.00000000  0.73241721  0.87181095  0.05000000
O0002 O02   0.00000000  0.77179691  0.37595169  0.05000000
O0003 O03   0.22864634  0.50000000  0.62560186  0.05000000
O0004 O04   0.23293902  0.00000000  0.62202770  0.05000000
#End data_Wien2k_Data

```

A.2 Ni₅CrO₈

```

data_Wien2k_Data
_cell_length_a  5.886888
_cell_length_b  5.886888
_cell_length_c  8.325316
_cell_angle_alpha  90.000000
_cell_angle_beta  90.000000

```

```
_cell_angle_gamma    90.000000
_cell_measurement_temperature  0.0
_diffn_ambient_temperature  0.0
_symmetry_space_group_name_H-M      'Imm2  '
_symmetry_space_group_number    44
_refine_date    '14- 4-2020'
_refine_method  'generated from Wien2k code'
_refine_special_details

loop_
_symmetry_equiv_pos_as_xyz
  +x,+y,+z
  -x,-y,+z
  +x,-y,+z
  -x,+y,+z
  +x+1/2,+y+1/2,+z+1/2
  -x+1/2,-y+1/2,+z+1/2
  +x+1/2,-y+1/2,+z+1/2
  -x+1/2,+y+1/2,+z+1/2

loop_
_atom_site_label
_atom_site_type_symbol
_atom_site_fract_x
_atom_site_fract_y
_atom_site_fract_z
_atom_site_U_iso_or_equiv
Cr001 Cr01  0.00000000  0.00000000  0.00061651  0.05000000
```

```

Ni001 Ni01  0.00000000  0.50000000  0.24969135  0.05000000
Ni002 Ni02  0.75444514  0.00000000  0.37815345  0.05000000
Ni003 Ni03  0.00000000  0.24663647  0.62295782  0.05000000
00001 001   0.00000000  0.75257692  0.87945296  0.05000000
00002 002   0.00000000  0.76241929  0.37851918  0.05000000
00003 003   0.25410569  0.50000000  0.62160598  0.05000000
00004 004   0.23972324  0.00000000  0.61910667  0.05000000
#End data_Wien2k_Data

```

A.3 Ni₂CrO₄

```

data_Wien2k_Data
_cell_length_a    5.949519
_cell_length_b    5.949519
_cell_length_c    8.413890
_cell_angle_alpha 90.000000
_cell_angle_beta  90.000000
_cell_angle_gamma 90.000000
_cell_measurement_temperature 0.0
_diffrn_ambient_temperature 0.0
_symmetry_space_group_name_H-M      'Imm2  '
_symmetry_space_group_number    44
_refine_date    '14- 4-2020'
_refine_method  'generated from Wien2k code'
_refine_special_details

loop_

```

_symmetry_equiv_pos_as_xyz

+x,+y,+z

-x,-y,+z

+x,-y,+z

-x,+y,+z

+x+1/2,+y+1/2,+z+1/2

-x+1/2,-y+1/2,+z+1/2

+x+1/2,-y+1/2,+z+1/2

-x+1/2,+y+1/2,+z+1/2

loop_

_atom_site_label

_atom_site_type_symbol

_atom_site_fract_x

_atom_site_fract_y

_atom_site_fract_z

_atom_site_U_iso_or_equiv

Ni001	Ni01	0.00000000	0.00000000	0.99445287	0.05000000
Ni002	Ni02	0.00000000	0.50000000	0.25660869	0.05000000
Ni001	Ni01	0.75012555	0.00000000	0.37542467	0.05000000
Cr002	Cr02	0.00000000	0.24988260	0.62503054	0.05000000
O0001	O01	0.00000000	0.73686898	0.85223304	0.05000000
O0002	O02	0.00000000	0.76444288	0.39712198	0.05000000
O0003	O03	0.21573025	0.50000000	0.62316900	0.05000000
O0004	O04	0.21637718	0.00000000	0.62643999	0.05000000

#End data_Wien2k_Data

A.4 $\text{Ni}_3\text{Cr}_3\text{O}_8$

```
data_Wien2k_Data
_cell_length_a    5.949516
_cell_length_b    5.949516
_cell_length_c    8.413886
_cell_angle_alpha 90.000000
_cell_angle_beta  90.000000
_cell_angle_gamma 90.000000
_cell_measurement_temperature 0.0
_diffrn_ambient_temperature 0.0
_symmetry_space_group_name_H-M      'Imm2  '
_symmetry_space_group_number    44
_refine_date    '14- 4-2020'
_refine_method  'generated from Wien2k code'
_refine_special_details

loop_
_symmetry_equiv_pos_as_xyz
  +x,+y,+z
  -x,-y,+z
  +x,-y,+z
  -x,+y,+z
  +x+1/2,+y+1/2,+z+1/2
  -x+1/2,-y+1/2,+z+1/2
  +x+1/2,-y+1/2,+z+1/2
  -x+1/2,+y+1/2,+z+1/2
loop_
```

```

_atom_site_label
_atom_site_type_symbol
_atom_site_fract_x
_atom_site_fract_y
_atom_site_fract_z
_atom_site_U_iso_or_equiv
Ni001 Ni01  0.00000000  0.00000000  0.99575714  0.05000000
Cr002 Cr02  0.00000000  0.50000000  0.24166720  0.05000000
Cr003 Cr03  0.75134874  0.00000000  0.37117804  0.05000000
Ni004 Ni04  0.00000000  0.25159429  0.62668916  0.05000000
O0001 O01   0.00000000  0.71774411  0.87330636  0.05000000
O0002 O02   0.00000000  0.76511075  0.38074334  0.05000000
O0003 O03   0.23800065  0.50000000  0.64743772  0.05000000
O0004 O04   0.24431290  0.00000000  0.60693319  0.05000000
#End data_Wien2k_Data

```

A.5 NiCr₂O₄

```

data_Wien2k_Data
_cell_length_a  5.970106
_cell_length_b  5.970106
_cell_length_c  8.443004
_cell_angle_alpha  90.000000
_cell_angle_beta  90.000000
_cell_angle_gamma  90.000000
_cell_measurement_temperature 0.0
_diffrn_ambient_temperature 0.0

```

```

_symmetry_space_group_name_H-M      'Imm2      '
_symmetry_space_group_number      44
_refine_date      '14- 4-2020'
_refine_method      'generated from Wien2k code'
_refine_special_details

loop_
_symmetry_equiv_pos_as_xyz
  +x,+y,+z
  -x,-y,+z
  +x,-y,+z
  -x,+y,+z
  +x+1/2,+y+1/2,+z+1/2
  -x+1/2,-y+1/2,+z+1/2
  +x+1/2,-y+1/2,+z+1/2
  -x+1/2,+y+1/2,+z+1/2
loop_
_atom_site_label
_atom_site_type_symbol
_atom_site_fract_x
_atom_site_fract_y
_atom_site_fract_z
_atom_site_U_iso_or_equiv
Ni001 Ni01  0.00000000  0.00000000  0.00323994  0.05000000
Ni002 Ni02  0.00000000  0.50000000  0.25338637  0.05000000
Cr001 Cr01  0.74899154  0.00000000  0.37524033  0.05000000
Cr002 Cr02  0.00000000  0.24898833  0.62525483  0.05000000

```

```

00001 001  0.00000000  0.72911213  0.86392530  0.05000000
00002 002  0.00000000  0.77721190  0.38425696  0.05000000
00003 003  0.22278801  0.50000000  0.63418251  0.05000000
00004 004  0.22913977  0.00000000  0.61382692  0.05000000
#End data_Wien2k_Data

```

A.6 Ni₃Cr₉O₁₆

```

data_Wien2k_Data
_cell_length_a  5.970103
_cell_length_b  5.970103
_cell_length_c  8.443001
_cell_angle_alpha  90.000000
_cell_angle_beta  90.000000
_cell_angle_gamma  90.000000
_cell_measurement_temperature 0.0
_diffrn_ambient_temperature 0.0
_symmetry_space_group_name_H-M      'P1      '
_symmetry_space_group_number      1
_refine_date  '14- 4-2020'
_refine_method 'generated from Wien2k code'
_refine_special_details

loop_
_symmetry_equiv_pos_as_xyz
  +x,+y,+z
loop_

```

```
_atom_site_label
_atom_site_type_symbol
_atom_site_fract_x
_atom_site_fract_y
_atom_site_fract_z
_atom_site_U_iso_or_equiv
Cr001 Cr01  0.74393598  0.00031386  0.37545581  0.05000000
Cr002 Cr02  0.24189772  0.99845159  0.37120576  0.05000000
Cr003 Cr03  0.25636281  0.50124689  0.87341909  0.05000000
Cr004 Cr04  0.75685013  0.50237591  0.87978627  0.05000000
Cr005 Cr05  0.99906094  0.24595357  0.62651424  0.05000000
Cr006 Cr06  0.99859477  0.74682126  0.62589112  0.05000000
Cr007 Cr07  0.50107747  0.75307825  0.12178279  0.05000000
Cr008 Cr08  0.50092026  0.25027332  0.12581464  0.05000000
Ni001 Ni01  0.99767507  0.00278824  0.99843935  0.05000000
Cr009 Cr09  0.50363728  0.50525306  0.50024379  0.05000000
Ni002 Ni02  0.00444694  0.49990913  0.24892279  0.05000000
Ni003 Ni03  0.49605208  0.00585668  0.74962755  0.05000000
O0001 O01   0.00501354  0.72750476  0.86581836  0.05000000
O0002 O02   0.00705990  0.27612641  0.86343628  0.05000000
O0003 O03   0.48801772  0.22542185  0.36269414  0.05000000
O0004 O04   0.49842423  0.77627154  0.35727273  0.05000000
O0005 O05   0.99274881  0.76875706  0.38797330  0.05000000
O0006 O06   0.99237460  0.22803534  0.38783230  0.05000000
O0007 O07   0.50908281  0.27559662  0.88959433  0.05000000
O0008 O08   0.50442562  0.72964764  0.88313656  0.05000000
O0009 O09   0.22780707  0.49054800  0.63733069  0.05000000
```

```
00010 010 0.77503466 0.49894806 0.64334312 0.05000000
00011 011 0.72866710 0.99913422 0.13738797 0.05000000
00012 012 0.26959308 0.00073094 0.13397608 0.05000000
00013 013 0.22585582 0.99256142 0.61006312 0.05000000
00014 014 0.76957111 0.99688319 0.61446056 0.05000000
00015 015 0.72790241 0.49980435 0.11813260 0.05000000
00016 016 0.27791003 0.50170682 0.11044465 0.05000000
#End data_Wien2k_Data
```

A.7 NiCr₅O₈

```
data_Wien2k_Data
_cell_length_a 5.996249
_cell_length_b 5.996249
_cell_length_c 8.479976
_cell_angle_alpha 90.000000
_cell_angle_beta 90.000000
_cell_angle_gamma 90.000000
_cell_measurement_temperature 0.0
_diffraction_ambient_temperature 0.0
_symmetry_space_group_name_H-M 'Imm2 '
_symmetry_space_group_number 44
_refine_date '14- 4-2020'
_refine_method 'generated from Wien2k code'
_refine_special_details

loop_
```

_symmetry_equiv_pos_as_xyz

+x,+y,+z

-x,-y,+z

+x,-y,+z

-x,+y,+z

+x+1/2,+y+1/2,+z+1/2

-x+1/2,-y+1/2,+z+1/2

+x+1/2,-y+1/2,+z+1/2

-x+1/2,+y+1/2,+z+1/2

loop_

_atom_site_label

_atom_site_type_symbol

_atom_site_fract_x

_atom_site_fract_y

_atom_site_fract_z

_atom_site_U_iso_or_equiv

Ni001	Ni01	0.00000000	0.00000000	0.99968901	0.05000000
Cr001	Cr01	0.00000000	0.50000000	0.74814806	0.05000000
Cr002	Cr02	0.00000000	0.24966409	0.37590363	0.05000000
Cr003	Cr03	0.25155932	0.00000000	0.62421635	0.05000000
00001	001	0.22867792	0.50000000	0.36162632	0.05000000
00002	002	0.77873076	0.00000000	0.38445582	0.05000000
00003	003	0.00000000	0.27108023	0.13853518	0.05000000
00004	004	0.00000000	0.77996344	0.61634149	0.05000000

#End data_Wien2k_Data

A.8 NiCr₁₁O₁₆

```
data_Wien2k_Data
_cell_length_a    5.990549
_cell_length_b    5.990549
_cell_length_c    8.471915
_cell_angle_alpha 90.000000
_cell_angle_beta  90.000000
_cell_angle_gamma 90.000000
_cell_measurement_temperature 0.0
_diffrn_ambient_temperature 0.0
_symmetry_space_group_name_H-M      'P1      '
_symmetry_space_group_number        1
_refine_date      '14- 4-2020'
_refine_method    'generated from Wien2k code'
_refine_special_details

loop_
_symmetry_equiv_pos_as_xyz
  +x,+y,+z

loop_
_atom_site_label
_atom_site_type_symbol
_atom_site_fract_x
_atom_site_fract_y
_atom_site_fract_z
_atom_site_U_iso_or_equiv
Cr001 Cr01  0.75133344  0.00030896  0.37433892  0.05000000
```

Cr002	Cr02	0.25101913	0.99614073	0.37276236	0.05000000
Cr003	Cr03	0.24894170	0.49901150	0.87672154	0.05000000
Cr004	Cr04	0.75106447	0.50252127	0.87662060	0.05000000
Cr005	Cr05	0.99796797	0.24939558	0.62506665	0.05000000
Cr006	Cr06	0.00401860	0.74746623	0.62369834	0.05000000
Cr007	Cr07	0.50132789	0.74967759	0.12506032	0.05000000
Cr008	Cr08	0.49723263	0.25219944	0.12603468	0.05000000
Cr009	Cr09	0.99660532	0.00468862	0.99713898	0.05000000
Cr010	Cr10	0.50835776	0.50159511	0.49844078	0.05000000
Ni001	Ni01	0.99577069	0.49548150	0.25354154	0.05000000
Cr011	Cr11	0.49288496	0.00525558	0.74926548	0.05000000
00001	001	0.00184452	0.72440771	0.85967735	0.05000000
00002	002	0.99542219	0.27413314	0.86315219	0.05000000
00003	003	0.49512047	0.22360538	0.36128034	0.05000000
00004	004	0.50763118	0.77290996	0.36151649	0.05000000
00005	005	0.00223066	0.77237641	0.38377625	0.05000000
00006	006	0.00224356	0.22161091	0.38801876	0.05000000
00007	007	0.49779009	0.27788714	0.88857076	0.05000000
00008	008	0.49936662	0.72243132	0.88928244	0.05000000
00009	009	0.22521122	0.49223113	0.64051261	0.05000000
00010	010	0.77513153	0.50619046	0.63917906	0.05000000
00011	011	0.72277127	0.00563379	0.13717336	0.05000000
00012	012	0.27781756	0.99942191	0.13794381	0.05000000
00013	013	0.22487874	0.00175524	0.61166579	0.05000000
00014	014	0.77769159	0.99645061	0.61043360	0.05000000
00015	015	0.72860116	0.50174341	0.11308107	0.05000000
00016	016	0.26972310	0.50346937	0.11604593	0.05000000

```
#End data_Wien2k_Data
```

A.9 Cr₃O₄

```
data_Wien2k_Data
_cell_length_a    6.061035
_cell_length_b    6.061035
_cell_length_c    8.571597
_cell_angle_alpha 90.000000
_cell_angle_beta  90.000000
_cell_angle_gamma 90.000000
_cell_measurement_temperature 0.0
_diffrn_ambient_temperature 0.0
_symmetry_space_group_name_H-M      'Imm2  '
_symmetry_space_group_number    44
_refine_date    '14- 4-2020'
_refine_method  'generated from Wien2k code'
_refine_special_details

loop_
_symmetry_equiv_pos_as_xyz
  +x,+y,+z
  -x,-y,+z
  +x,-y,+z
  -x,+y,+z
  +x+1/2,+y+1/2,+z+1/2
  -x+1/2,-y+1/2,+z+1/2
```

+x+1/2,-y+1/2,+z+1/2

-x+1/2,+y+1/2,+z+1/2

loop_

_atom_site_label

_atom_site_type_symbol

_atom_site_fract_x

_atom_site_fract_y

_atom_site_fract_z

_atom_site_U_iso_or_equiv

Cr001	Cr01	0.00000000	0.00000000	0.99417727	0.05000000
-------	------	------------	------------	------------	------------

Cr002	Cr02	0.00000000	0.50000000	0.24417678	0.05000000
-------	------	------------	------------	------------	------------

Cr001	Cr01	0.75160324	0.00000000	0.37601989	0.05000000
-------	------	------------	------------	------------	------------

Cr002	Cr02	0.00000000	0.25159381	0.62602970	0.05000000
-------	------	------------	------------	------------	------------

O0001	O01	0.00000000	0.72487677	0.86132850	0.05000000
-------	-----	------------	------------	------------	------------

O0002	O02	0.00000000	0.77674551	0.39055296	0.05000000
-------	-----	------------	------------	------------	------------

O0003	O03	0.22325985	0.50000000	0.64055951	0.05000000
-------	-----	------------	------------	------------	------------

O0004	O04	0.22486757	0.00000000	0.61133242	0.05000000
-------	-----	------------	------------	------------	------------

#End data_Wien2k_Data

APPENDIX B

Supplementary Video Captions

Video S1. Crumpled graphene ball formed by shear and compressive forces rolling during sliding. Video was recorded at 25 frames per second (fps) and is shown in real time.

Video S2. Folding and unfolding of a single graphene sheet. Video was recorded at 25 fps and is shown in real time.

Video S3. Mechanical behaviors of graphitic nanocrystals and intra-sheet links. Video was recorded at 25 fps and is shown in real time.

Video S4. Rotation of graphitic nanocrystals during sliding. Video was recorded at 25 fps and is shown in real time.

Video S5. Adhesion of crumpled graphene after compression. Video was recorded at 25 fps and is shown in real time.

Video S6. Adhesion of crumpled graphene after shear. Video was recorded at 25 fps and is shown in real time.

Video S7. Unfolding and folding crumpled paper can be done reversibly by applying tensile forces to the edges of the sheet. Video was recorded at 30 fps and is shown in real time.